7-6-2012

Modeling, simulation and experimental study of the UNM low power reltron

Shawn Soh

Recommended Citation

Soh, Shawn. "Modeling, simulation and experimental study of the UNM low power reltron." (2012). https://digitalrepository.unm.edu/ece_etds/240

Shawn SzeLiip Soh
Candidate

Electrical and Computer Engineering
Department

This dissertation is approved, and it is acceptable in quality and form for publication:

Approved by the Dissertation Committee:

Professor Edl Schamiloglu , Chairperson

Professor Mark Gilmore

Dr R. Bruce Miller

Professor James Ellison

MODELING, SIMULATION AND EXPERIMENTAL STUDY OF THE UNM LOW POWER RELTRON

BY

Shawn SzeLiip Soh
B.E., Nanyang Technological University, Singapore, 2003

DISSERTATION

Submitted in Partial Fulfillment of the
Requirements for the Degree of

Doctor of Philosophy
Engineering

The University of New Mexico
Albuquerque, New Mexico

May, 2012

ACKNOWLEDGMENTS

To God be the Glory

who created Heaven and Earth

To my beautiful wife and children

In the Physical Sciences I would like to thank Prof. Edl Schamiloglu, Dr. R.B. Miller, Prof. Mark Gilmore, Prof. James Ellison, Prof. Christos G. Christodoulou, Ralph Lee Terry and a spiritual mom to every graduate student Elmyra Grelle.

In the Spiritual Sciences, I would like to thank Dad and Mom, Pastor Mike Derrick, Mrs. Darlene Derrick, Tim, Tarrah, Esther, Renee Heyer, Pastor Brian Bailey, Suzanne Ying, Michael Derrick and everyone in Zion Chapel, Waverly, New York.

MODELING, SIMULATION AND EXPERIMENTAL STUDY OF THE UNM LOW POWER RELTRON

BY

Shawn SzeLiip Soh
B.E., Nanyang Technological University, Singapore, 2003

ABSTRACT OF DISSERTATION

Submitted in Partial Fulfillment of the
Requirements for the Degree of

Doctor of Philosophy
Engineering

The University of New Mexico
Albuquerque, New Mexico

May, 2012

MODELING, SIMULATION AND EXPERIMENTAL STUDY OF THE UNM LOW POWER RELTRON

by

Shawn SzeLiip Soh

ABSTRACT

Reltrons are high power electron beam microwave oscillators that do not require an external magnetic field. The University of New Mexico (UNM) has a low power educational reltron system developed during an AFOSR-sponsored FY'94 Multi-University Research Initiative (MURI) program. This dissertation focuses on developing mathematical models of, and performing particle-in-cell (PIC) simulations and conducting experiments on the low power reltron.

The modules in the reltron tube can be described using mathematical models. We first analyze the minimum beam potential required to self-excite the modulating cavity. We obtain the resonant modes of the modulating cavity using a circuit model. The electron beam is modeled using a relativistic ballistic current model from which we derive the optimal drift distance where the modulating current will peak. We develop a transmission line model of the single and dual extraction cavity that is used to match the cavity impedance to the beam impedance. We also model the electrostatic field distribution between the anode-cathode (A-K) gap and post acceleration gap.

We compare our 1D / 2D models with 3D simulations performed using HFSS and CST. Full 3D simulations are required because the reltron is not axisymmetric. We also performed PIC simulations of the reltron using MAGIC. MAGIC is able to simulate the beam-wave interaction self-consistently. This accounts for all interactions between all modules as the beam propagates through the reltron. We optimize the reltron parameters in MAGIC and confirm the UNM reltron is able to generate microwave power in the megawatt range.

We conducted experiments using the UNM low power reltron to compare our mathematical models and simulations with the performance of the actual reltron system. Experiments allow us to account for physical phenomena that are not described by models or simulations. Maximum microwave power generated by the UNM low power reltron is 116 kW for a duration of 100 ns. The low output power is accounted for by electrical breakdown in the electron beam diode's A-K gap during operation.

Finally, we conclude with recommendations for future work that would resolve the difficulties encountered in the experiments.

Table of Contents

CHAPTER 1: INTRODUCTION

Reltrons belong to a class of narrowband megawatt (MW) microwave sources that are efficient and compact [1]. Reltrons are able to generate high power microwaves (HPM) with excellent power and frequency stability for the duration of the pulse. Reltrons operate without external magnetic fields, thus giving reltron systems a higher power to mass and volume density ratios. Reltrons typically use velvet cathodes which are cold cathodes that are readily available. Velvet cathodes are very cheap compared to thermionic cathodes and can generate current densities >1 kA/cm^2. The tube performance is independent of the load impedance. Reltrons can generate long pulses, up to microsecond duration, enabling them to radiate microwaves not only with high peak power, but also large energy per pulse.

Reltron tubes were first developed to operate in the L and S bands [1]. The L band reltron can reach peak microwave power of 600 MW at 1 GHz with average microwave energy of 220 J/pulse. The tube is driven by a 24 stage, 0.44 μF, 50 kV bipolar charging Marx generator. Beam voltage is 250 kV, beam current is 1.35 kA and post acceleration voltage is 850 kV. The 1 GHz cavity uses grids made from stainless steel mesh with 90% transparency. Comparing microwave power to the total beam power gives an efficiency of 40.4%. Using symmetric horseshoe tuners, the cavity can be tuned to 15% above and below the nominal frequency. Two WR975 rectangular waveguides, each with two cavities, are used to extract microwaves with each cavity offset transversely to account for the beam transit time. The 1 GHz tube can also be made to generate microwaves at 3 GHz by using WR340 waveguides in the extraction cavity [2]. It gives a peak microwave power of 45 MW with a pulse duration of ~1 μs. Average microwave energy is 25 J/pulse. The beam current oscillates at 1.042 GHz and the radiated microwaves at 3.12 GHz.

The S band tube can reach peak microwave power of 300 MW at 3 GHz with average microwave energy of 40 J/pulse [1]. The tube is driven by a 22 stage, 0.44 μF, 50 kV bipolar charging Marx. The beam voltage is 200 kV, beam current 1.0 kA and post acceleration voltage is 700 kV. The 3 GHz cavity uses stainless steel grids of 50 x 50 mesh, 1 mil thickness with 1.8 cm grid spacing. Mesh is the wire cloth specification given by 1/(wire diameter + distance between wires). The measured cold cavity π/2 frequency is 3.091 GHz with a quality factor (Q) of 225. The cavity Q can be increased to 500-700 using 40 mesh grids. All grids have transparency exceeding 95%. The 3 GHz super-reltron has two WR340 extraction waveguides. Using tunable reflecting barriers to maximize extraction, microwaves are radiated from the two windows. The 3 GHz tube has a full width half maximum (FWHM) pulsed duration of 100 ns and a bandwidth of 2.875 GHz to 3.075 GHz. Maximum microwave power is generated at 3.05 GHz.

The 3 GHz cavity can also be driven at much lower voltages to generate longer microwave pulses [3]. The cathode radius is reduced to 2 cm to lower the beam current. The beam voltage is 60 kV and post acceleration voltage 90 kV. A single window is used to radiate microwaves. This reltron has a pulse repetition rate (PRR) of 25 Hz, limited by the power modulator, with pulse duration 2 μs but at power levels of ~20 MW. Table 1.1 summarizes the performance ranges of the commercial L and S band tubes.

Table 1.1 Performance parameters of commercially available reltrons.

Device	**Pulsed Power**	**Frequency (GHz)**	**Microwave Power (MW)**	**Duration (ns)**
1 GHz Super-Reltron [2]	250 kV, 850 kV, 1.35 kA	1	600	500-1000
3 GHz Super-Reltron [2]	200 kV, 750 kV, 1.0 kA	3	350	300-500
Low Power Reltron [3]	60 kV, 90 kV 0.4 kA	3	20	2000
Gridless Reltron [4]	100 kV, 150 kV 200 A	2.856	20	5000

The gridless reltron [4,5] overcomes the pulse duration and PRR limitations by using gridless modulating and extraction cavities. Grids are woven from thin wires that enhance electric fields that induce breakdown. Velvet cathodes generate plasma resulting in gap closure in the anode cathode (A-K) gap. Breakdown in the reltron limits the microwave duration. The gridless reltron utilizes a thermionic Pierce electron gun that emits electrons without plasma. The gun focuses the beam as it traverses the A-K gap into the modulating cavity. A magnetic field from a permanent magnet placed at the beam collector catches the electrons as they start to leave the modulating cavity and disperses them. The magnetic field also guides the beam into the extraction cavity, allowing the beam to give up its energy to generate microwaves.

Tien et al. [6] proposed using a constant accelerating or decelerating potential to increase the space charge waves' magnitude in an electron beam. They send a current modulated beam into a high voltage drift tube. The beam electrons are accelerated or decelerated in the tube and microwaves are extracted from the beam as it leaves the tube. A 1D analytic model of their amplifier was proposed using the method of partition space and method of electronic equations. Using the method of partition space, they partitioned the drift space into many segments and model each segment as a diode. Using the Llewellyn-Peterson equation [7], they solve for the ac convection current density and ac electron velocity in each diode. Using the method of electronic equations, they solve a second order ordinary differential equation for the ac convection current density of the tube. They constructed three tubes and tested them for their gain. The 1st tube had 6 cavities and a gain of 24 dB; the 2nd tube had 2 cavities and a gain of 10 dB; the 3rd tube had 3 cavities and a gain of 20 dB.

The arletron is a post-accelerated device proposed by Gardelle [8]. The arletron is essentially a variant of the klystron using coaxial extraction. The arletron uses an annular split cavity instead of a reentrant cavity typically used in a klystron. The arletron can be self-excited at relatively low beam voltages <100 kV. As the arletron has a low beam current of 1 kA, a magnetic field of 0.5 T or less is sufficient to confine the beam. Depending on the beam and accelerating voltage, output power can reach 700 MW at 3 GHz in MAGIC PIC [9] simulations.

Post-acceleration can increase bunching in Cherenkov microwave sources such as the Travelling Wave Tube (TWT) or the Backward Wave Oscillator (BWO). Abubakirov and Savelyev [10] verified this by adding an accelerating force to the TWT / BWO electron force equation. They added a spatially varying rectangular accelerating force that is zero everywhere and constant within a region of longitudinal space. Integrating over longitudinal space and wave period, they showed that the efficiency of relativistic TWTs and BWOs can be increased to 50%.

The UNM low power educational reltron was designed jointly by the former Titan Albuquerque (Bruce Miller) and the University of New Mexico (Edl Schamiloglu) during an AFOSR-sponsored FY'94 HPM MURI program. This reltron is a scaled down, low power version of the commercial S band super-reltron tube. Figure 1.1 shows the block diagram of the subsystems and Figure 1.2 shows the circuit schematic of the UNM reltron system.

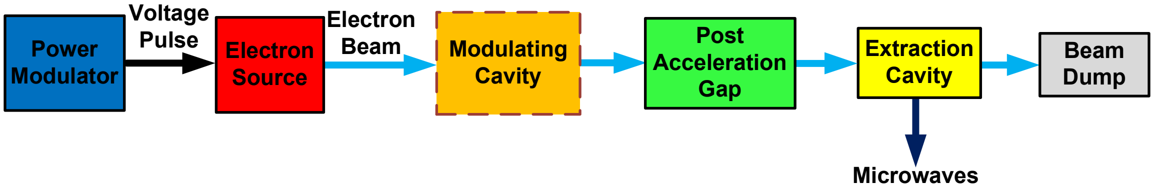

Figure 1.1 Block diagram of the UNM low power reltron system.

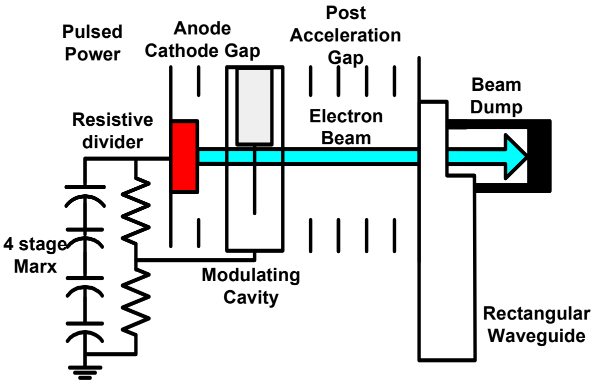

Figure 1.2 Circuit diagram of UNM low power reltron system.

The UNM reltron is driven by a 2 stage bipolar charging 396 J Marx generator capable of generating a maximum voltage of 120 kV. The voltage pulse has a rise time of ~0.2 µs and a pulse width of 1-4 µs, which we can adjust before triggering. The pulse width is controlled by a crowbar switch that shunts current away from the load. An analytic model of the Marx generator's charging and discharging process has been developed [11]. Figure 1.3 and Figure 1.4 show voltage and current waveforms generated by the model compared with experimental measurements taken from the Marx generator.

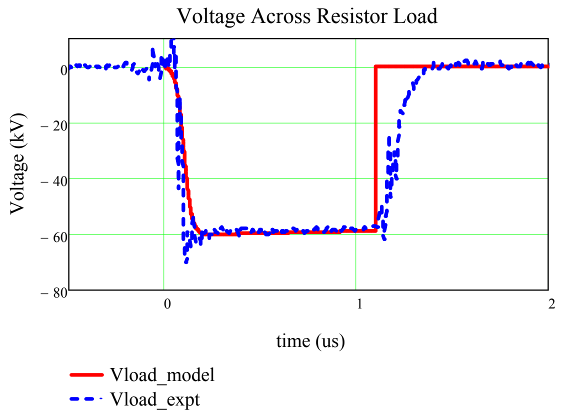

Figure 1.3 Voltage across the resistive load using the model (red) and measured in the experiment (blue).

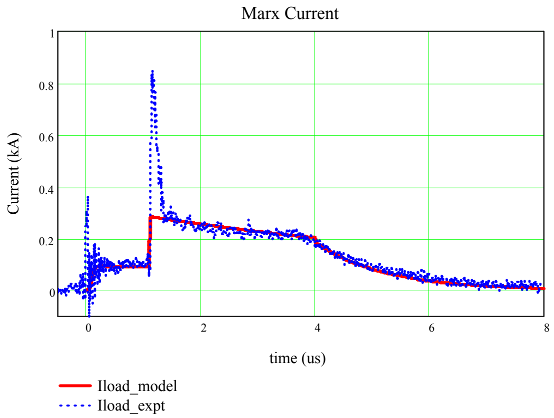

Figure 1.4 Marx generator current as a function of time using the model (red) and measured in the experiment (blue).

Figure 1.5 shows a 1D circuit model of the UNM modulating cavity [12]. The RLC circuit in the middle represents the coupling cavity and the two RLC circuits on the side represent the back and front of the main cavity, respectively.

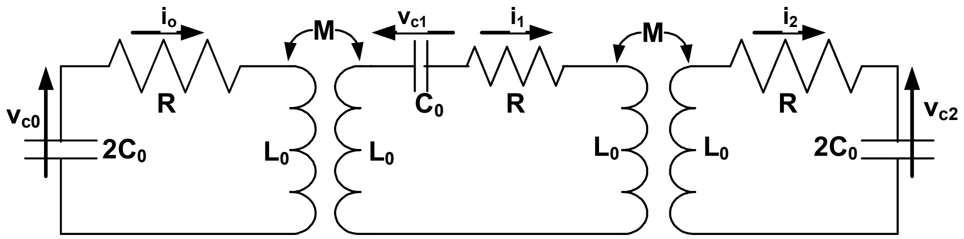

Figure 1.5 Circuit model of the UNM reltron's modulating cavity.

The circuit model shows that the cavity can operate in three resonant modes. We have derived the exact solution for the three resonant modes which includes all the higher order terms. The three resonant frequencies for the lossless case (R=0) are given by

$$\omega_{\pi/2} = \frac{1}{\sqrt{2L_0C_0}}, \tag{1.1}$$

$$\omega_0 = 2\omega_{\pi/2}\sqrt{\frac{1}{3+\sqrt{1+16k^2}}}, \quad \text{and} \tag{1.2}$$

$$\omega_{\pi} = 2\omega_{\pi/2}\sqrt{\frac{1}{3-\sqrt{1+16k^2}}}, \tag{1.3}$$

where the coupling factor $k = M/\sqrt{L_0 L_0} = M/L_0$ represents the coupling between cavities. The three modes in order of increasing frequency are given by $\omega_0 < \omega_{\pi/2} < \omega_{\pi}$ for 0<k<1. Plots of $\omega_0 / \omega_{\pi/2}$ and $\omega_{\pi} / \omega_{\pi/2}$ as a function of the coupling factor k are shown in Figure 1.6 and Figure 1.7, respectively. As we increase k, we are increasing mode separation between ω_0 and $\omega_{\pi/2}$, and $\omega_{\pi/2}$ and ω_{π}.

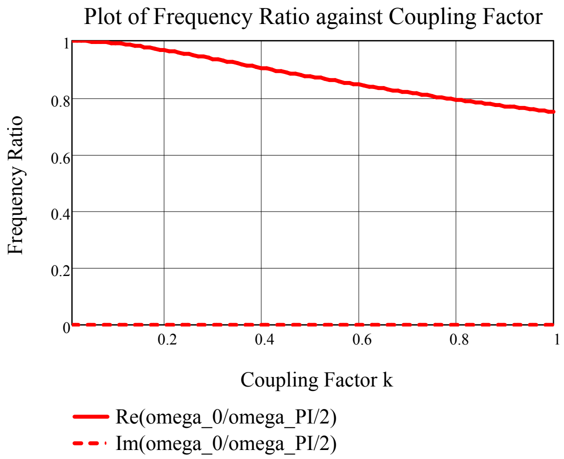

Figure 1.6 Plot of $\omega_0/\omega_{\pi/2}$ as a function of coupling factor k.

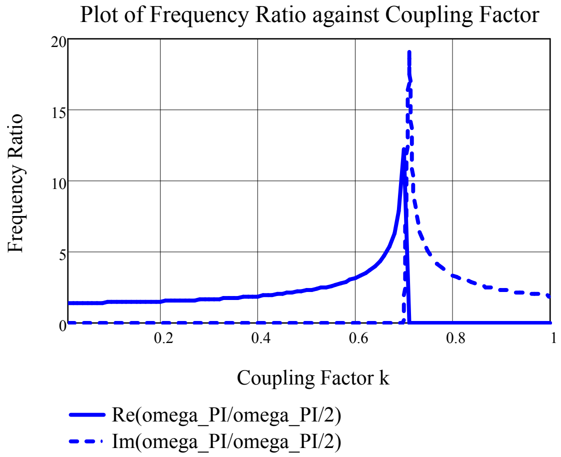

Figure 1.7 Plot of $\omega_{\pi}/\omega_{\pi/2}$ as a function of coupling factor k.

Figure 1.6 shows ω_0 falling below $\omega_{\pi/2}$ as the coupling factor increases. Improving the coupling between cavities will cause ω_0 to decrease. Frequency ω_0 may fall to a level that is below the cutoff frequency of the cavity. As such, ω_0 will not be supported inside the cavity. Figure 1.7 shows ω_π increasing above $\omega_{\pi/2}$ as the coupling factor increases. Beyond k=0.7, ω_π becomes imaginary. Good coupling between the cavities will prevent the growth of ω_π resonating in the cavity. Coupling between cavities improves as more azimuthal magnetic field in the main cavity gets coupled to the coupling cavity.

This dissertation presents results of the analytic model, computer simulations and experimental results conducted on the UNM low power reltron. Chapter 2 presents a single particle analysis as the electron transits through the modulating cavity and the minimum beam potential required to self-excite the modulating cavity. Chapter 3 presents the resonant modes of the modulating cavity and a ballistic model of the electron beam. Chapter 4 presents the analytic model, HFSS frequency-domain simulations of the single and proposed dual extraction cavity. We also performed S parameter measurements of the UNM low power reltron's extraction cavity and compared those with our simulations. Chapter 5 presents an electrostatic analysis of the E_z fields in the A-K gap and post-acceleration gap. Chapter 6 presents MAGIC simulations of the UNM low power reltron and Chapter 7 presents the experimental results measured using the UNM low power reltron system. Chapter 8 presents conclusions and future work. Appendix A presents a derivation of the dispersion relation of space charge waves on an electron beam.

CHAPTER 2: SINGLE PARTICLE ANALYSIS

In this chapter we will investigate the electron's interaction with the modulating cavity. Electrons entering the modulating cavity induce an electromagnetic (EM) shockwave inside the cavity. The electrons in the rear portion of the beam get slowed down by the wave, losing energy to the wave in the cavity. The EM wave grows in amplitude by drawing upon the kinetic energy (K.E.) of incoming electrons. This wave modulates the electrons' velocities and the electrons are accelerated or decelerated depending on the relative phases between the electrons and the wave. As the electrons drift downstream, velocity modulation leads to density modulation, causing bunches to form.

The modulating cavity is tuned to operate in the π/2 mode [12]. There are no fields inside the coupling cavity when the modulating cavity resonates in the π/2 mode except due to power flow. As such the modulating cavity operates like a split cavity oscillator (SCO). A SCO comprises of two transit time oscillators (TTO) aligned on axis sharing the middle grid. The physics of the TTO was studied by Marcum [13]. Marcum first derived the velocity and displacement equation for an electron as it transits through an oscillating electric field. From these two equations, he was able to approximate an analytic solution of the change in K.E. when the electron leaves the cavity. It turns out that the analytic solution describes the motion of a cycloid. Using a mechanical wheel, he drew out a graphical representation of the solution.

Building upon Marcum's idea, we will determine the change in K.E. of an electron when it exits the modulating cavity using both spatial and perturbation analysis. The main cavity has a radius of 1.6 inch and a gap of 0.375 inch between the grids. The electric field inside is assumed to have peak amplitude of 75 kV/cm with frequency 2.75 GHz. The electrons have an initial energy of 50 keV.

2.1 CHANGE IN KINETIC ENERGY FOR A 3 GRID SCO USING METHOD OF PARTITION SPACE

In the spatial analysis we begin by dividing the longitudinal space in the cavity into many spatial cells of length Δx. The time step is determined by the courant stability condition $\Delta t \le \Delta z / c$ [14]. We launch an electron into the 1st gap of the main cavity for a specific phase angle θ. We use the electron's velocity and displacement equations to track the electron as it transits the 1st gap. When the electron enters the 2nd gap, we use the corresponding velocity and displacement equations that represent the electron motion in the 2nd gap. The electron's K.E. is calculated from its velocity as it leaves the 2nd gap. The peak amplitude of the electric field is kept constant throughout the electron's transit. We repeat this calculation with small increments in the phase angle to calculate the K.E. change for all phase angles from 0 to 2π.

Inside the main cavity, the electric field is assumed to have the following polarity: $E_z = E_0 \sin(\omega t + \theta)$ for $0 \le z < g$ and $E_z = -E_0 \sin(\omega t + \theta)$ for $g \le z < 2g$, as indicated in Figure 2.1.

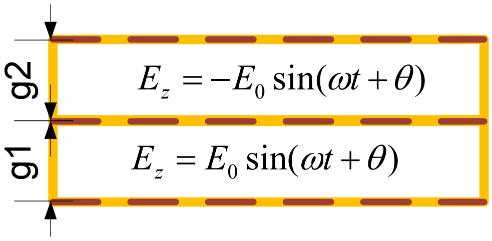

Figure 2.1 Schematic of a 3 grid SCO.

In the 1st gap $0 \le z < g$, the equation of motion is

$$m_e \frac{dv}{dt} = -q_e E_0 \sin(\omega t + \theta) . \tag{2.1}$$

Integrating once we obtain the velocity in the 1st gap

$$\int_0^v dv = \int_0^t \left[-\frac{q_e E_0}{m_e} E_0 \sin(\omega t + \theta) \right] dt ,$$

$$v(t,\theta) = v_0 + \frac{q_e E_0}{m_e \omega} \left(\cos(\omega t + \theta) - \cos\theta \right), \tag{2.2}$$

where v_0 is the initial velocity of the electron as it enters the 1st gap. Integrating again we obtain the displacement in the 1st gap

$$\int_0^z dz = \int_0^t \left[v_0 + \frac{q_e E_0}{m_e \omega} \left(\cos(\omega t + \theta) - \cos\theta \right) \right] dt ,$$

$$z(t,\theta) = v_0 t + \frac{q_e E_0}{m_e \omega^2}\left(\sin(\omega t + \theta) - \sin\theta - \omega t\cos\theta\right). \qquad (2.3)$$

We check our code implementation by assuming that the transit time of the electron through the 1st gap is very short compared to the EM wave period. We neglect the phase delay through the 1st gap and easily obtain the electron's velocity and displacement in the 2nd gap by replacing E_0 with $-E_0$,

$$v(t,\theta) = \tilde{v}_0 - \frac{q_e E_0}{m_e \omega}\left(\cos(\omega t + \theta) - \cos\theta\right), \qquad (2.4)$$

$$z(t,\theta) = \tilde{v}_0 t - \frac{q_e E_0}{m_e \omega^2}\left(\sin(\omega t + \theta) - \sin\theta - \omega t\cos\theta\right), \qquad (2.5)$$

where $\tilde{v}_0$ is the velocity as the electron enters the 2nd gap. Figure 2.2 shows a plot of the phase space for $\theta = 0.25\pi$. The velocity in the graph is normalized to the speed of light. The electron decelerates as it enters the 1st gap $0<z<0.375$ inch and accelerates as it enters the 2nd gap $0.375<z<0.75$ inch. It enters the cavity with an initial velocity of 0.412686c and exits the cavity with velocity 0.412687c.

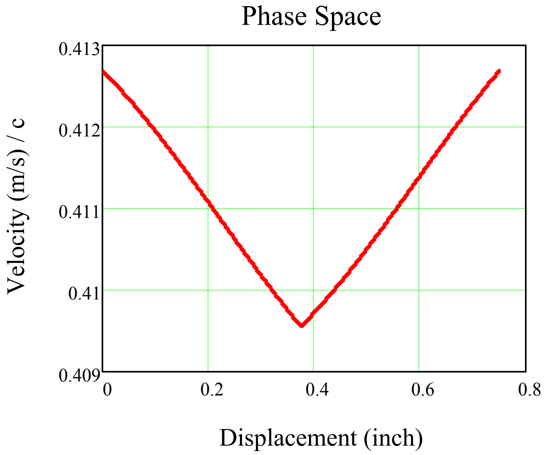

Figure 2.2 Electron velocity for θ=0.25π.

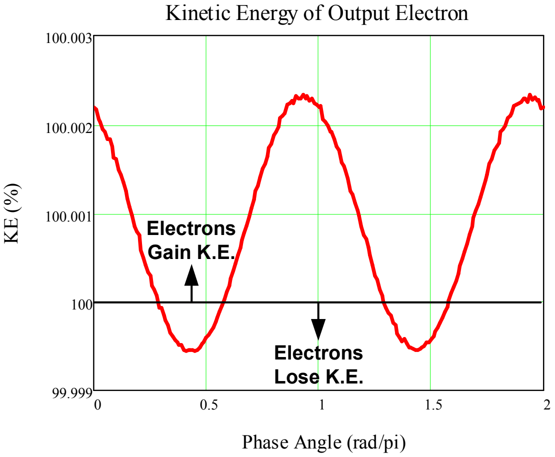

Figure 2.3 Electron K.E. as a function of phase angle.

Figure 2.3 plots the K.E. of an electron for all phases from 0 to 2π as a percentage of its initial K.E.. Electrons lose energy to the SCO for phase angles between 0.28π to 0.58π and 1.29π to 1.58π. The first minimum point is at $\theta_{min}=0.41$. This is where an electron loses the most K.E. to the gap, thus causing the E_z field in the gap to grow at the maximum rate.

We verify θ_{min}=0.41 is the phase angle for maximum growth in the EM wave by deriving the optimum phase that causes electrons to lose the most K.E. to the gap. Electrons lose the most K.E. to the gap when they experience maximum retardation in the middle of the gap. This allows us to express the optimum distance as a function of electron velocity and frequency,

$$k_e z = \frac{\pi}{2},$$

$$\frac{2\pi}{\lambda_e}\frac{g_{opt}}{2} = \frac{\pi}{2},$$

$$\frac{g_{opt}}{\lambda_e} = \frac{g_{opt}}{v_e / f} = \frac{1}{2},$$

$$g_{opt} = \frac{v_e}{2f}, \tag{2.6}$$

where k_e is the electron wavenumber, λ_e is the wavelength due to electron motion, v_e is the electron velocity, and f is the frequency of electron oscillation. In a 1D field, $f = c / \lambda$, where c is the speed of light and λ is the longitudinal wavelength in the cavity. We approximate $v_e \approx v_{initial} = 0.4127c$ and solve for the phase that results in the maximum growth of the E_z field in a single gap

$$\frac{g_{opt}}{\lambda} = \frac{v_e}{2c} \text{ and}$$

$$\theta_{opt} = \frac{g_{opt}}{\lambda} = \frac{v_e}{2c} = \frac{0.4127}{2} = 0.2063\pi . \tag{2.7}$$

Since the electron has to transit through two gaps, the total phase is $\theta_{min} = 2\theta_{opt} = 0.41\pi$, which is the first minimum point in Figure 2.3.

In order to account for transit time, we define variable $\tilde{t}$ as the time the electron enters the 2nd gap. At $t = \tilde{t}$, an electron enters the 2nd gap with velocity $v(\tilde{t}) = \tilde{v}$ and its displacement is $z(\tilde{t}) = g$.

In the 2nd gap $g \le z < 2g$, the equation of motion is

$m_e \frac{dv}{dt} = -q_e E_0 \sin(\omega t + \theta)$. Integrating once we obtain the velocity in the 2nd gap

$$\int_{\tilde{v}}^{v} dv = \int_{\tilde{t}}^{t} \left[\frac{q_e E_0}{m_e \omega} E_0 \sin(\omega t + \theta) \right] dt,$$

$$v(t, \tilde{t}, \tilde{v}, \theta) = \tilde{v} - \frac{q_e E_0}{m_e \omega} \left[\cos(\omega t + \theta) - \cos\left(\omega \tilde{t} + \theta \right) \right]. \tag{2.8}$$

Integrating again we obtain the displacement in the 2nd gap

$$\int_{g}^{z} dz = \int_{\tilde{t}}^{t} \left\{ \tilde{v} - \frac{q_e E_0}{m_e \omega} \left[\cos(\omega t + \theta) - \cos\left(\omega \tilde{t} + \theta \right) \right] \right\} dt,$$

$$z\left(t, \tilde{t}, \tilde{v}, \theta \right) = g + \tilde{v}\left(t - \tilde{t} \right) - \frac{q_e E_0}{m_e \omega^2} \left[\sin(\omega t + \theta) - \sin\left(\omega \tilde{t} + \theta \right) - \omega\left(t - \tilde{t} \right) \cos\left(\omega \tilde{t} + \theta \right) \right]. \tag{2.9}$$

We plot the E_z field inside both gaps for θ = 1.5π in Figure 2.4. The electron transits through the 1st gap and sees an abrupt change in the E_z field as it enters the 2nd gap due to the transit time effect. It experiences a brief period of deceleration, resulting in a decrease in velocity and resumes accelerating as the E_z field becomes negative over the period the electron transits through the 2nd gap.

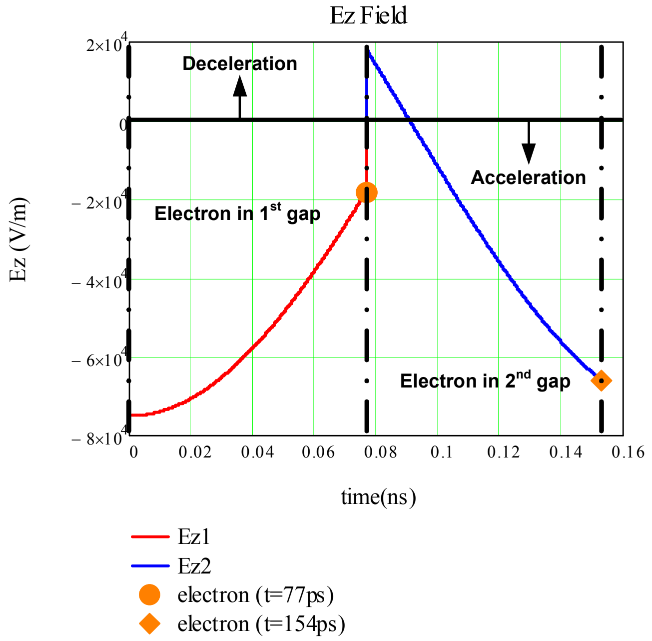

Figure 2.4 Plot of E_z field as a function of time for θ= 1.5π.

Figure 2.5 shows a plot of the phase space for a phase angle of 1.5π. An electron enters the cavity with initial velocity 0.41268c and increases to 0.4164c when it exits the cavity. Figure 2.6 is a plot of electron K.E. as a function of phase angle. The minimum point is now at a later phase with θ_{min}=0.57π.

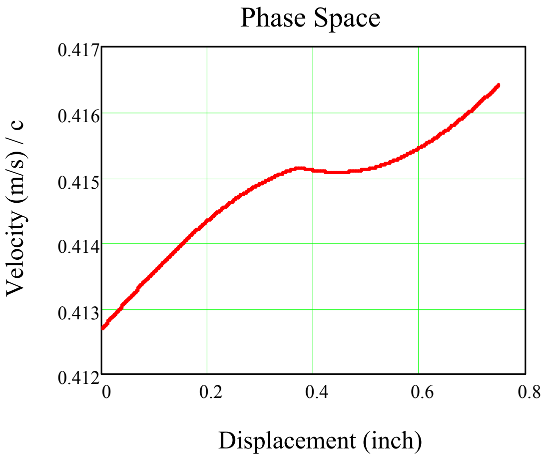

Figure 2.5 Electron velocity for θ=1.5π.

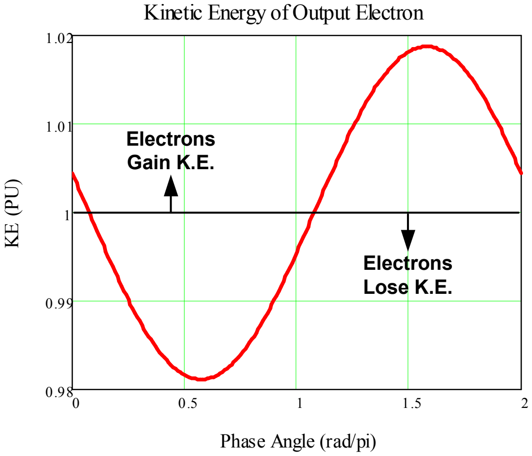

Figure 2.6 Electron K.E. as a function of phase angle.

The optimum gap g_{opt} to excite maximum growth of the EM wave is not equal to the optimum gap to induce maximum RF current. From Miller's particle trajectory code, the optimum gap to induce maximum RF current for ~200 keV electron beam is given by [15]

$$g_{opti\_RF} = v_0 / 3.2 f, \tag{2.10}$$

where he multiplies the denominator of (2.6) by 1.6 to shorten the gap to optimize electron bunching. The E_z field in the gap is time periodic and independent of the longitudinal axis for TM_{mn0} modes. The shortened gap maximizes velocity modulation that maximizes density modulation. For a 2.75 GHz, 200 keV beam the optimum RF current gap g_{opt_RF} is 0.93 inch. The middle of gap g1 will have an electron phase angle of 0.3125π and the end of gap g1 will have a phase angle of 0.625π. The E_z maximum for a sinusoidal E_z field is at 1 inch (0.5π), so all the electrons leave the gap accelerating.

2.2 CHANGE IN KINETIC ENERGY FOR A 3 GRID SCO USING PERTURBATION METHOD

Using perturbation analysis, we determine the minimum beam voltage required for the electrons to give up their energy inside the cavity. For the EM wave to grow inside the cavity, the electrons have to exit the cavity with K.E. less than their initial K.E. for all phase angles. We average the change in K.E over all phase angles and a negative ΔK.E. implies energy loss

$$\Delta K.E. = \frac{1}{2\pi}\int_0^{2\pi}\left[\frac{K.E.(\theta)_f - K.E.(\theta)_i}{K.E.(\theta)_i}\right]d\theta\,. \tag{2.11}$$

Let $\varepsilon = q_e E_0 / m_e \omega v_0$ be the perturbation constant. Assuming that the beam is monoenergetic, the velocity of the electron in the 1st gap can now be expressed as

$$v(t,\theta) = v_0\left[1+\varepsilon\left(\cos(\omega t+\theta)-\cos\theta\right)\right]. \tag{2.12}$$

At $t=\tilde{t}$ the electron enters the 2nd gap with velocity

$$v\left(\tilde{t},\theta\right) = \tilde{v} = v_0\left\{1+\varepsilon\left[\cos\left(\omega\tilde{t}+\theta\right)-\cos\theta\right]\right\}. \tag{2.13}$$

The velocity of the electron through the 2nd gap is given by

$$v(t,\tilde{t},\tilde{v},\theta) = \tilde{v} - \frac{q_e E_0}{m_e \omega}\left[\cos(\omega t+\theta)-\cos\left(\omega\tilde{t}+\theta\right)\right]. \tag{2.14}$$

Substituting $\tilde{v}$ in the above we have

$$v(t,\tilde{t},\theta) = v_0\left\{1+\varepsilon\left[2\cos\left(\omega\tilde{t}+\theta\right)-\cos\theta-\cos(\omega t+\theta)\right]\right\}. \tag{2.15}$$

We obtain the displacement in the 1st gap by integrating gap 1's velocity to obtain

$$z(t,\theta) = v_0\left\{t+\varepsilon\left[\frac{1}{\omega}\left(\sin(\omega t+\theta)-\frac{1}{\omega}\sin\theta - t\cos\theta\right)\right]\right\}. \tag{2.16}$$

We obtain the displacement in the 2nd gap by integrating gap 2's velocity to obtain

$$\begin{aligned} z(t,\tilde{t},\theta) &= g + v_0 \\ &\times\left\{\left(t-\tilde{t}\right)+\varepsilon\left(t-\tilde{t}\right)\left(2\cos\left(\omega\tilde{t}+\theta\right)-\cos\theta\right)-\frac{1}{\omega}\left(\sin(\omega t+\theta)-\frac{1}{\omega}\sin\left(\omega\tilde{t}+\theta\right)\right)\right\}. \end{aligned} \tag{2.17}$$

We define T to be the time it takes for an electron to exit the SCO. At t=T, $z(T,\theta)=2g$ and the electron velocity as it exits the gap is

$$v(T,\tilde{t},\theta)=v_0\left\{1+\varepsilon\left[2\cos\left(\omega\tilde{t}+\theta\right)-\cos\theta-\cos(\omega T+\theta)\right]\right\}. \tag{2.18}$$

Substituting the series $\tilde{t}=\tilde{t}_0+\varepsilon\tilde{t}_1+...$ and $T=T_0+\varepsilon T_1+...$ in the above, we obtain

$$\frac{v(T,\theta)}{v_0}=1+\varepsilon\left[2\cos\left(\omega\tilde{t}_0+\theta\right)-2\varepsilon\tilde{t}_1\,\omega\sin\left(\omega\tilde{t}_0+\theta\right)-\cos\theta-\cos\left(\omega T_0+\theta\right)+\varepsilon T_1\omega\sin\left(\omega T_0+\theta\right)\right].$$

where we have used the approximation $\cos\left(\omega\varepsilon\tilde{t}_1\right)\approx 1$ and $\sin\left(\omega\varepsilon\tilde{t}_1\right)\approx\omega\varepsilon\tilde{t}_1$.

We can calculate the average change in K.E. of the electron for all phases by integrating

$$\frac{\Delta k}{\varepsilon^2}=\frac{1}{2\pi}\int_0^{2\pi}\left[\left(\frac{v(T,\theta)}{v_0}\right)^2-1\right]d\theta. \tag{2.19}$$

For us to perform the above integration, we have to derive expressions for $\tilde{t}_1$ and T$_1$.

At $t=\tilde{t}$ the electron leaves the 1st gap

$$z(\tilde{t},\theta)=g=v_0\left\{\tilde{t}+\varepsilon\left[\frac{1}{\omega}\left(\sin(\omega\tilde{t}+\theta)-\frac{1}{\omega}\sin\theta-\tilde{t}\cos\theta\right)\right]\right\}. \tag{2.20}$$

Rearranging the above we have an expression for $\tilde{t}$

$$\begin{aligned}\tilde{t}&=\frac{g}{v_0}-\varepsilon\left[\frac{1}{\omega}\sin\left(\omega\tilde{t}_0+\theta\right)-\frac{1}{\omega}\sin\theta-\tilde{t}_0\cos\theta\right]+...,\\ &=\tilde{t}_0+\varepsilon\tilde{t}_1+...,\end{aligned} \tag{2.21}$$

At t=T, the electron leaves the 2nd gap

$$\begin{aligned}&z(T,\tilde{t},\theta)=g+v_0\\ &\quad\times\left\{\left(T-\tilde{t}\right)+\varepsilon\left(T-\tilde{t}\right)\left(2\cos\left(\omega\tilde{t}+\theta\right)-\cos\theta\right)-\frac{1}{\omega}\left(\sin(\omega t+\theta)-\frac{1}{\omega}\sin\left(\omega\tilde{t}+\theta\right)\right)\right\}.\end{aligned} \tag{2.22}$$

Rearranging the above we have an expression for T

$$2g = g + v_0 \left\{ \left(t - \tilde{t} \right) + \varepsilon \left(t - \tilde{t} \right) \left(2\cos\left(\omega \tilde{t} + \theta \right) - \cos\theta \right) - \frac{1}{\omega} \left(\sin(\omega t + \theta) - \frac{1}{\omega} \sin\left(\omega \tilde{t} + \theta \right) \right) \right\}$$

$$T = 2\frac{g}{v_0} - \varepsilon \left[\frac{2}{\omega} \sin\left(\omega \tilde{t}_0 + \theta \right) - \frac{1}{\omega} \sin\theta - T_0 \cos\theta + T_0 \cos\left(\omega \tilde{t}_0 + \theta \right) - \frac{1}{\omega} \sin\left(\omega T_0 + \theta \right) \right] + \ldots$$

$$= T_0 + \varepsilon T_1 + \ldots, \tag{2.23}$$

Substitute $\tilde{t}_1$ and T_1 in the K.E. integral and performing some trigonometric simplifications we obtain the change in K.E. to be

$$\frac{\Delta k}{\varepsilon^2} = 14\sin^2\left(\frac{T_0\omega}{4}\right) - 2T_0\omega\sin\left(\frac{T_0\omega}{4}\right) - 4\sin^2\left(\frac{T_0\omega}{4}\right) + T_0\omega\sin(T_0\omega). \tag{2.24}$$

Marder [16] obtains a similar expression by neglecting higher order terms

$$\frac{\Delta k_m}{\varepsilon^2} = 6 - 4T_0\omega\sin\left(\frac{T_0\omega}{2}\right) - 8\cos\left(\frac{T_0\omega}{2}\right) + 2\cos(T_0\omega) + 2T_0\omega\sin(T_0\omega). \tag{2.25}$$

Figure 2.7 shows the change in K.E. of the electron calculated using (2.24) compared with the solution given by Marder's paper (2.25). Both solutions give increasing oscillations as the beam voltage approaches zero. This behavior is seen when we take the limits: beam voltage $V_{beam} \to 0$, giving electron velocity $v_0 \to 0$ resulting in transit time $T_0 \to \infty$. With $T_0 \to \infty$, the sine and cosine terms oscillate with increasing frequency.

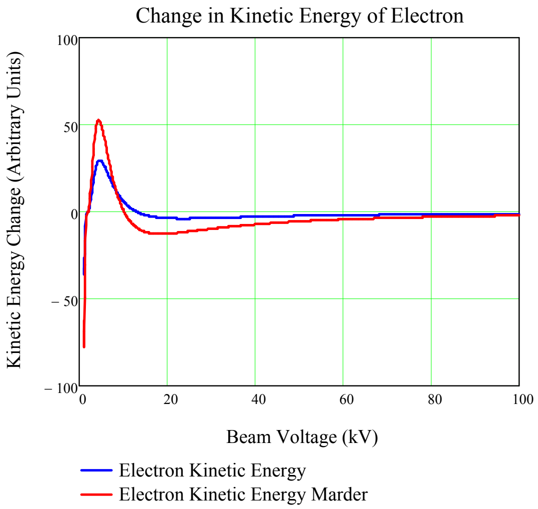

Figure 2.7 Change in electron K.E for a 3 grid SCO.

We neglect the oscillatory regions and focus on solutions where the change in K.E. is negative over a large range of beam voltages. This ensures the cavity will consistently self-excite even if the beam voltage deviates somewhat. Also the energy spread in an electron beam may cause some electrons to be in the positive region if we operate in the oscillatory regime. The minimum beam voltage to ensure self-excitation is 13.1 kV. Marder's analysis gives 10.2 kV. As our formula includes higher order terms, we see higher order terms increase the self-excitation voltage. The K.E. change is most negative at -3.84 when beam voltage is 23.6 kV. This minimum point corresponds to maximum growth of the E_z field in the gap.

2.3 CHANGE IN KINETIC ENERGY FOR A 4 GRID SCO USING PERTURBATION METHOD

We add a drift tube of length d between the two gaps to allow the electrons to form tighter bunches. Typically the drift tube has a radius below the cutoff wavelength of the EM wave inside the gap. In addition the gap and the tube are separated by grids that attenuate any wave passing through it. This allows us to assume that the EM wave is trapped inside the gap and does not propagate into the tube.

When the electrons leave the 1st gap, they maintain their exiting momentum as there are no fields in the tube. They can induce surface charges on the walls of the drift tube. This slows the electrons down because of finite wall conductivity. While the electrons in the front slow down, the electrons in the back, which are still in the gap, are still experiencing acceleration. The electrons in the back catch up with electrons in the front, thereby increasing the density of the electron bunch.

Inside the cavity, the electric field is assumed to have the following polarity: $E_z = E_0 \sin(\omega t + \theta)$ for $0 \le z < g$, $E_z = 0$ for $g \le z < g + d$ and $E_z = -E_0 \sin(\omega t + \theta)$ for $g + d \le z < 2g + d$, as shown in Figure 2.8.

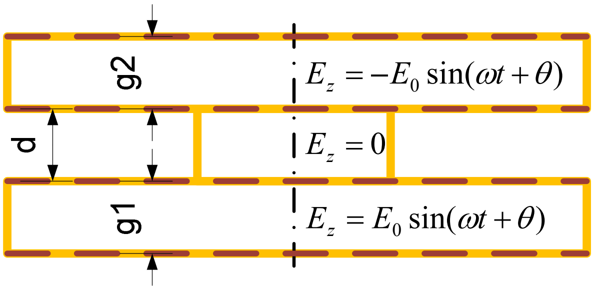

Figure 2.8 Schematic of a 4 grid SCO.

In the 1st gap $0 \le z < g$, the equation of motion is

$$m_e \frac{dv}{dt} = -q_e E_0 \sin(\omega t + \theta). \tag{2.26}$$

In the drift tube $g \le z < g + d$, the equation of motion is

$$m_e \frac{dv}{dt} = 0. \tag{2.27}$$

In the 2nd gap $g + d \le z < 2g + d$, the equation of motion is

$$m_e \frac{dv}{dt} = q_e E_0 \sin(\omega t + \theta). \tag{2.28}$$

We perform a perturbation analysis for the 4 grid SCO to determine the change in K.E.. The methodology is mostly similar to that of the 3 grid SCO. For the 4 grid SCO we have to include the additional transit time of the electron through the drift tube [17]. Performing the analysis, we find the change in K.E. is given by

$$\begin{aligned}\frac{\Delta ke}{\varepsilon^2} = {} & \frac{\omega g}{v_0}\sin\left(\frac{\omega g - T_0\omega v_0}{v_0}\right) - \frac{2\omega g}{v_0}\sin\left(\frac{\omega d - T_0\omega v_0}{v_0}\right) - 4\sin^2\left(\frac{\omega g - T_0\omega v_0}{2v_0}\right) - 4\sin^2\left(\frac{\omega d - T_0\omega v_0}{2v_0}\right) \\ & - 4\sin\left(\frac{\omega d}{2v_0}\right) - 4\sin\left(\frac{\omega g}{2v_0}\right) + 4\sin\left(\frac{T_0\omega}{2}\right) + 4\sin\left(\frac{\omega d - \omega g}{2v_0}\right) - T_0\omega\sin\left(\frac{\omega g - T_0\omega v_0}{v_0}\right) \\ & - T_0\omega\sin(T_0\omega) + \frac{\omega g}{v_0}\sin\left(\frac{\omega d}{v_0}\right) + \frac{\omega d}{v_0}\sin\left(\frac{\omega d}{v_0}\right) + \frac{\omega g}{v_0}\sin\left(\frac{\omega g}{v_0}\right) - \frac{\omega d}{v_0}\sin\left(\frac{\omega d - \omega g}{v_0}\right).\end{aligned} \tag{2.29}$$

We set the drift distance equal to the cavity gap d=g=0.375 inch. Figure 2.9 shows the change in K.E. of the electron for the 3 grid and 4 grid SCO. Just like the case for the 3 grid SCO, we neglect the oscillatory regions and focus on the region where the curve remains negative.

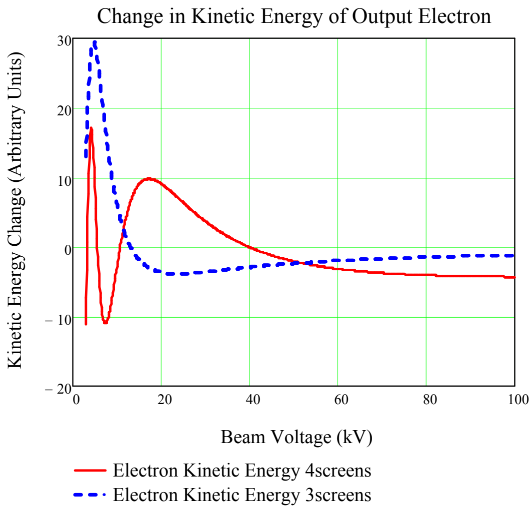

Figure 2.9 Change in electron K.E for a 3 grid and a 4 grid SCO (d=g=0.375 inch).

Minimum voltage for the 4 grid SCO to self-excite is 39.9 kV, which is higher than for the 3 grid SCO at 13.1 kV. The additional drift tube results in a higher excitation voltage even though the electrons do not lose energy in the drift tube. The 4 grid SCO reaches a lower energy change of -4.3 compared to the minimum of the 3 grid at -3.8. We postulate the reason for the improvement in performance. The electron exits the 1st gap and travel down the drift tube. For the 3 grid SCO, the electron immediately sees the electric field of opposite polarity. For the 4 grid SCO, the electron arrives at the 2nd cavity and sees the opposite polarity electric field phase shifted by the time it takes the electron to travel the additional drift distance. A higher beam voltage is required because of the difference in phase between the electric fields in the 1st and 2nd gap. This difference in phase increases the energy lost by the electrons to the cavity as the electron velocity is perturbed even greater in the 4 grid SCO.

We can lower the self-excitation voltage of the 4 grid SCO by decreasing the drift distance to d=g/2=0.1875 inch. The self-excitation threshold decreases to 29.6 kV but the K.E. change increases to -3.49 at 14.3 kV.

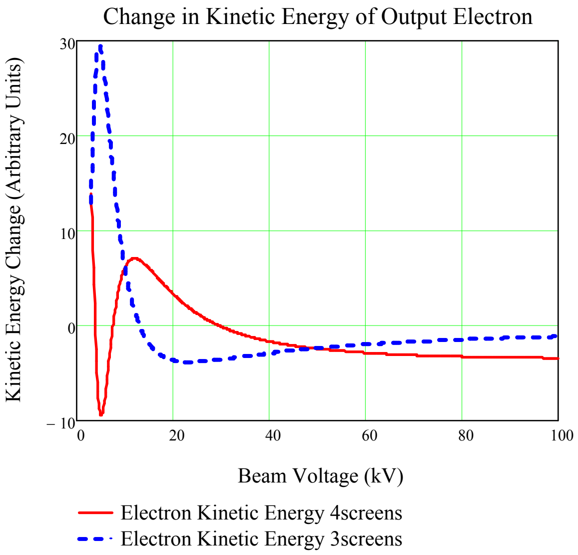

Figure 2.10 Change in electron K.E for a 3 grid and 4 grid SCO (d=g/2=0.1875 inch).

At this drift distance, it may seem advantageous to use the 3 grid SCO which has a lower excitation voltage (23.6 kV) and a lower energy change (-3.84). However, we note that the 4 grid minimum occurs at 14.3 kV. The 4 grid SCO is suited to operate with beam voltages in the 100’s kV as its energy change approaches its minimum point in that range. As we increase the beam voltage, we need to increase the drift distance to ensure the energy change is most negative. The 3 grid SCO is made for lower beam voltages as it reaches its minimum at 23.6 kV.

In this chapter we have analyzed the electron’s interaction with the modulating cavity using a 1D model. Using the electron’s velocity and displacement and equations of motion, we track the electron’s progress through the gaps and generate a plot of electron’s K.E. as a function of phase angle. Using perturbation analysis, we are able to determine the self-excitation potential for a 3 grid and 4 grid SCO.

CHAPTER 3: MODULATING CAVITY RESONANT MODES AND DISPERSION RELATION

The modulating cavity in the reltron converts a continuous electron beam into bunches. The modulating cavity comprises a main cavity and a coupling cavity radially joined to the main cavity, as shown in Figure 3.1. The main cavity has three grids: in the back, middle, and front of the cavity. These grids are weaved into specific patterns using 10's µm-thin wires. The grids trap the EM waves in between them while allowing electrons to pass through. The coupling cavity has two cylindrical idlers aligned with its axis.

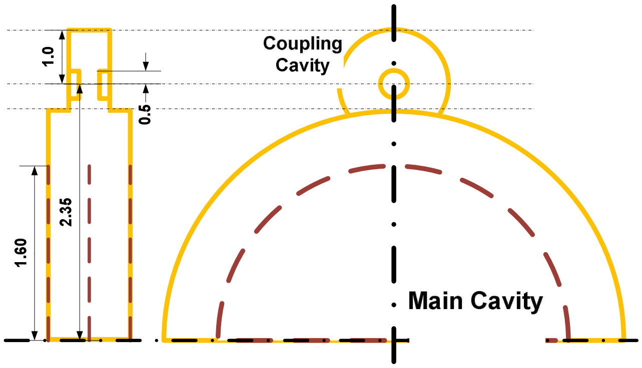

Figure 3.1: Schematic of the reltron modulating cavity.

The modulating cavity is symmetric about its vertical axis and its middle grid. It is assembled by bolting two gridded half-cell side coupled cavities back to back [18]. We model the main and coupling cavity as two cylindrical pillbox cavities of equal height, but having different radii. The coupling cavity is offset 2.35 inch from the main cavity's center axis. We merge the coupling cavity with the main cavity in the section where the two cavities overlap.

We tune the main cavity using a horseshoe tuner and the coupling cavity with an idler, as shown in Figure 3.2. These tuners are moved using vacuum rotary feedthroughs.

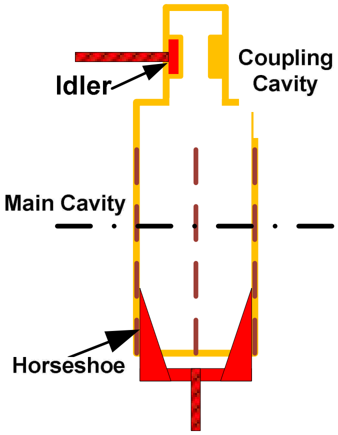

Figure 3.2: Modulating cavity tuning mechanism.

The idler is a capacitive tuner that changes the height of the coupling cavity. This changes the resonant frequency of the coupling cavity and the coupling coefficient between the main and coupling cavity. The horseshoe tuner is an inductive tuner that changes the cavity radius. This reduces the volume of the main cavity, thereby increasing the resonant frequency of the modulating cavity.

The coupling cavity is tuned in conjunction with the main cavity to make the modulating cavity resonate at the desired $\pi/2$ mode. In the $\pi/2$ mode there are no fields in the coupling cavity and the longitudinal electric fields in the main cavity oscillate with opposite polarity. In the $\pi/2$ mode the main cavity operates like an SCO [16].

3.1 MAGIC SIMULATIONS OF RESONANT MODES IN THE MODULATING CAVITY

We simulate the cold modulating cavity using MAGIC [19], a Finite Difference Time Domain (FDTD) Particle-In-Cell (PIC) code which can also perform cold cavity simulations in the absence of particles. The eigenmode solver in MAGIC solves the time domain form of Maxwell's equation through multiple time steps. It applies an operator to an initial field pattern 30 times in order to grow the dominant mode within a frequency window. A solution is obtained when the operator is able to grow the dominant mode three times greater than the modes outside the window. The eigenmode solver typically initializes a random electric field pattern inside the cavity and the operator "grows" the mode. As we are interested only in TM modes, we force B_z=0 to grow pure TM modes.

The modulating cavity has three resonant cavities so it must have three fundamental eigenmodes and an infinite number of harmonics for each mode. The three modes are the 0, π /2, and π modes, in order of increasing frequency [20]. Using MAGIC we calculate the resonant frequency for the TM_{010} π /2 mode to be 2.70 GHz. We plot the direction and intensity of the electric fields in Figure 3.3. The cavity has a Q of 5888.

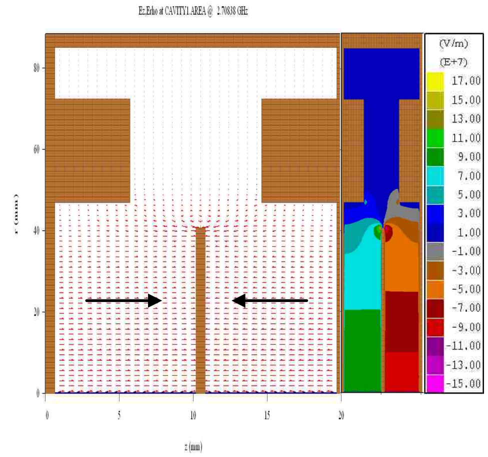

Figure 3.3: MAGIC simulation of the π/2 mode (2.70 GHz). No particles were included in this simulation.

The π mode resonates at 3.29 GHz. The direction and intensity of the electric fields for this mode are plotted in Figure 3.4. The cavity Q is 6016.

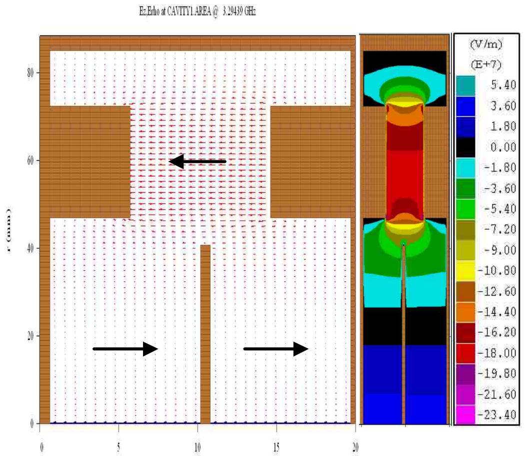

Figure 3.4: MAGIC simulation of the π mode (3.29 GHz). No particles were included in this simulation.

The 0 mode is not shown because MAGIC could not converge to a resonant frequency. This may be due to the smallest simulation cell size of 0.025 inch being much larger than the grid thickness 10 μm. The artificially large size of the grid in the simulations prevents the longer wavelength 0 mode from developing in the cavity.

The electric field distribution for the TM_{020} π /2 mode is plotted in Figure 3.5. The cavity resonates at 6.24 GHz with a Q of 9309.

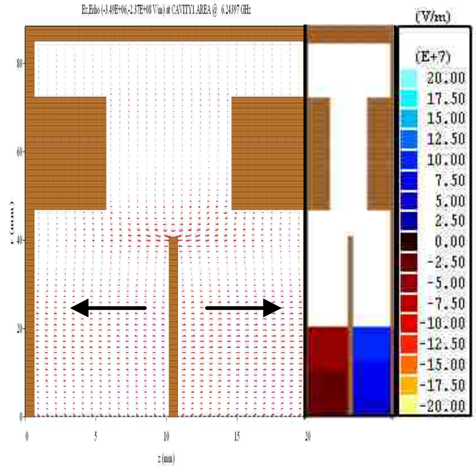

Figure 3.5: MAGIC simulation of the π /2 mode (6.24 GHz). No particles were included in this simulation.

The electric field distribution for the second harmonic TM_{020} 0 mode is plotted in Figure 3.6. The 0 mode resonates at 5.56 GHz with a Q of 9101.

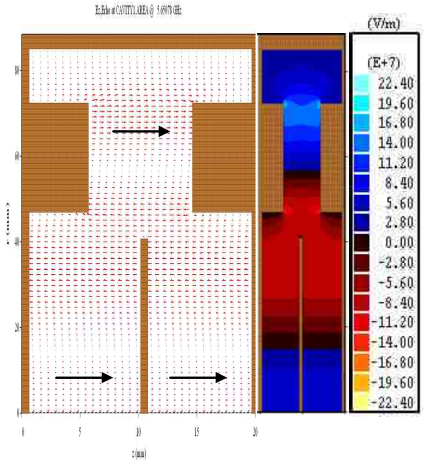

Figure 3.6: MAGIC simulation of the 0 mode (5.65 GHz). No particles were included in this simulation.

The electric field distribution for the second harmonic TM_{020} π mode is plotted in Figure 3.7. The π mode resonates at 6.51 GHz with a Q of 9503.

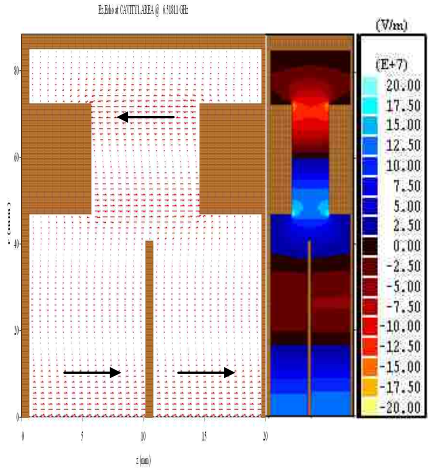

Figure 3.7: MAGIC simulation of the π mode (6.51 GHz). No particles were included in this simulation.

We plot the eigenmode frequencies obtained from MAGIC with the eigenmodes from S parameter measurements (Chapter 3.2) of the actual modulating cavity in Figure 3.8. The plot gives the dispersion relation of the cold modulating cavity for the TM_{010} and TM_{020} mode.

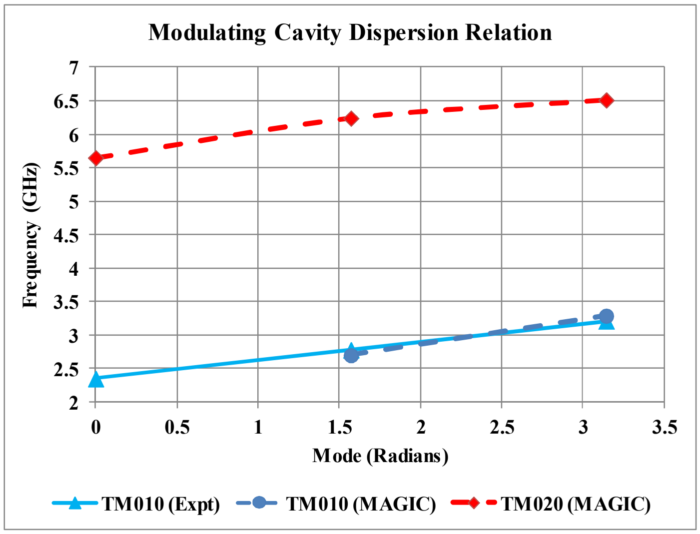

Figure 3.8: Dispersion relation of the modulating cavity obtained using MAGIC. Also indicated are S parameter measurements.

3.2 S PARAMETER MEASUREMENTS OF THE MODULATING CAVITY

In order to perform S parameter measurements, we made elliptical Bdot probes with 5 cm major axis to excite the cold cavity. We measure the S parameters using a vector network analyzer (VNA) model HP 8720D. It has a frequency range of 50 MHz to 20 GHz, 1 Hz frequency resolution, power range of -70 dBm to 5 dBm and a dynamic range of 100 dB.

We perform an S_{21} sweep from 2 GHz to 3.5 GHz and look for 3 distinct dips in the S_{21}. The dips correspond to the resonant frequencies in the cavity. We tune the horseshoe and idler dials until the frequency span between the lowest and middle resonant frequency is equal to the frequency span between the middle and highest resonant frequency. This occurs when we set the horseshoe dial to 2400 and the idler dial to 3409. From the S_{21} measurements (Figure 3.9) we see the 0 mode resonates at 2.35 GHz, the $\pi/2$ mode at 2.78 GHz, and the π mode at 3.21 GHz.

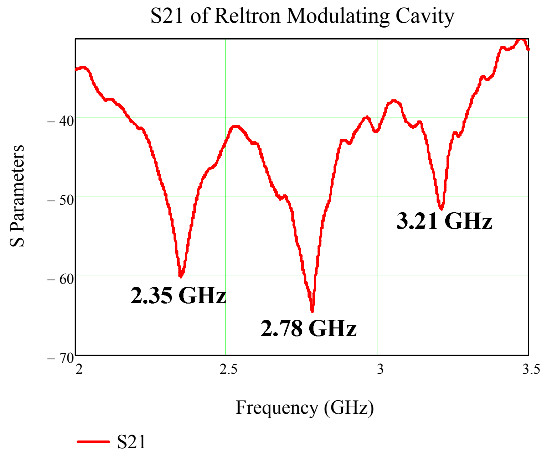

Figure 3.9: S_{21} measurement of cold cavity.

From the resonant modes, we calculate the coupling coefficient between the cavities using the bi-periodic coupled resonator circuit model [21]

$$k^2 \cos^2(m\pi/2N) = \left(1-(\omega_a/\omega_m)^2\right)\left(1-(\omega_c/\omega_m)^2\right), \tag{3.1}$$

where m=0,1,..2N, k is the coupling factor between the main cavity and the coupling cavity, ω_a is the resonant frequency of the main cavity (accelerating cavity), ω_c is the resonant frequency of the coupling cavity, m is the mode number and N is the number of coupling cavities with N+1 accelerating cavities. For the reltron, we have one coupling cavity so N=1 and we have three modes m=0,1, and 2 which correspond to the 0 mode, π/2 mode, and π mode, respectively.

For m=N=1, the modulating cavity resonates in the π/2 mode and equation (3.1) has two solutions $\omega_a = \omega_{\pi/2 \text{ mode}}$ or $\omega_c = \omega_{\pi/2 \text{ mode}}$. The solution $\omega_c = \omega_{\pi/2 \text{ mode}}$ is not valid as this corresponds to the case where the coupling cavities are excited so we have only $\omega_a = \omega_{\pi/2 \text{ mode}}$. Substituting $\omega_a = \omega_{\pi/2}$, we solve for k and ω_c using the two equations for m=0 and m=2

$$k^2 = \left(1-(\omega_{\pi/2}/\omega_0)^2\right)\left(1-(\omega_c/\omega_0)^2\right), \tag{3.2}$$

$$k^2 \cos^2(\pi/N) = \left(1-(\omega_{\pi/2}/\omega_\pi)^2\right)\left(1-(\omega_c/\omega_\pi)^2\right). \tag{3.3}$$

We find ω_c=2.592 GHz for k= ±0.294. Since negative values of k are not used, the coupling coefficient between the main and coupling cavity is k=0.294.

3.3 BALLISTIC BUNCHING

Electrons are velocity modulated by the EM wave in the modulating cavity. The frequency of oscillation is equal to the resonant frequency of the cavity. After electrons leave the modulating cavity, they undergo bunching in the ballistic regime [22]. Current modulation results from the bunching and can be modeled as an infinite sum of harmonic currents. We will derive the modulation current that includes the effect of the post-acceleration voltage.

Let v(t) be the electron velocity after it leaves the modulating cavity. Invoking conservation of energy, the electron K.E. is equal to the potential energy

$$\begin{aligned}\frac{1}{2}m_e v^2 &= q_e(V_{AK}+V_{post}) + q_e M V_{gap}\sin(\omega t)\\ &= q_e V_{beam} + q_e M V_{gap}\sin(\omega t)\\ &= \frac{1}{2}m_e {v^2}_0 + q_e M V_{gap}\sin(\omega t),\end{aligned}$$

$$\begin{aligned}v(t) &= v_0\sqrt{1+\frac{MV_{gap}}{V_{beam}}\sin(\omega t)}\\ &\approx v_0\left[1+\frac{MV_{gap}}{2V_{beam}}\sin(\omega t)\right],\end{aligned} \tag{3.4}$$

where M is the wave-to-beam coupling coefficient, and V_{gap} is the voltage across the cavity gap. Our velocity v(t) is equivalent to the kinematic velocity derived by Webster [22] with the exception that our beam voltage is the sum of the A-K gap voltage and post-acceleration voltage. This allows us to use the modulation current derived by Webster. Replacing the non-relativistic velocity with its relativistic form, we obtain the relativistic bunching parameter that converts the non-relativistic ballistic current to the relativistic regime [23]. The relativistic ballistic current is given by

$$I(t) = I_0 + 2I_0 \sum_{n=1}^{\infty} J_n(nX) \cos\left[n\omega(t - \frac{z}{v_0}) \right], \tag{3.5}$$

where the bunching parameter $X = \frac{q_e M V_{gap}}{m_e c_0^2} \frac{1}{\gamma_0(\gamma_0^2 - 1)} \frac{\omega}{v_0} z.$

Current modulation increases as the electrons drift downstream. For the fundamental mode, Bessel $J_1(X)$ is maximum when X_{max} =1.841. For a 2.75 GHz, 75 keV beam, the fundament modulating current will peak at the optimum drift distance d_{opt} of 3.03 inch. This is verified in our plot of the magnitude of the fundamental modulating current $|I_1|$ as a function of distance (Figure 3.10). We also plot the magnitude of the 2nd harmonic $|I_2|$ and 3rd harmonic $|I_3|$ current magnitudes.

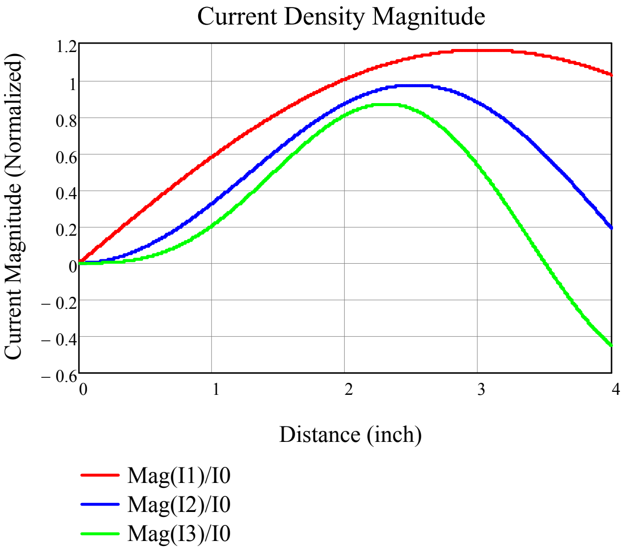

Figure 3.10: Plot of normalized current density magnitude as a function of distance.

Figure 3.11 shows the fundamental modulating current I_1 as it propagates through the longitudinal space. In our plot we use M = 1, $V_{gap} = 0.75V_{beam}$, $V_{beam} = 75$ kV, and $v_0 = (2q_eV_{beam}/m_e)^{1/2}$. The optimum drift distance d_{opt} sees a reversal in polarity every half wave period 181.5 ps ($\omega t = \pi/2$).

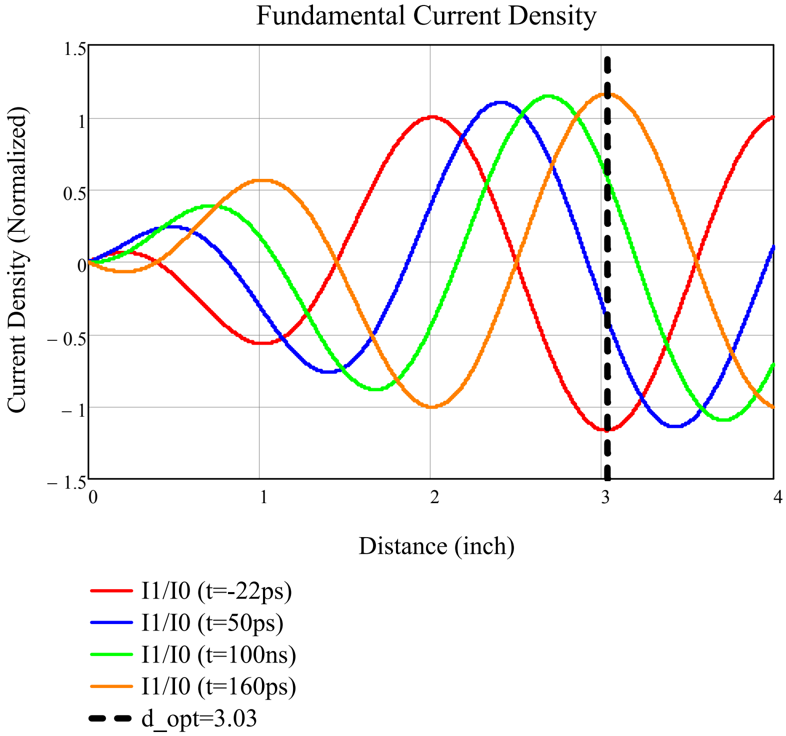

Figure 3.11: Plot of normalized fundamental current density as a function of distance.

We know the "ideal" beam current is shaped like a delta function while the actual beam current is shaped like a very sharp Gaussian pulse. In order to model the beam current more accurately, we need to include the higher harmonic terms. Figure 3.12 plots multi time harmonic current density for n = 1,2, and 3. The effect of the higher harmonics is to shorten the optimum drift distance to $d_{opt\ n} = 2.459$ inch. The current peak arrives at $d_{opt\ n}$ at every full wave period (363 ps) since the I_1 mode dominates in magnitude.

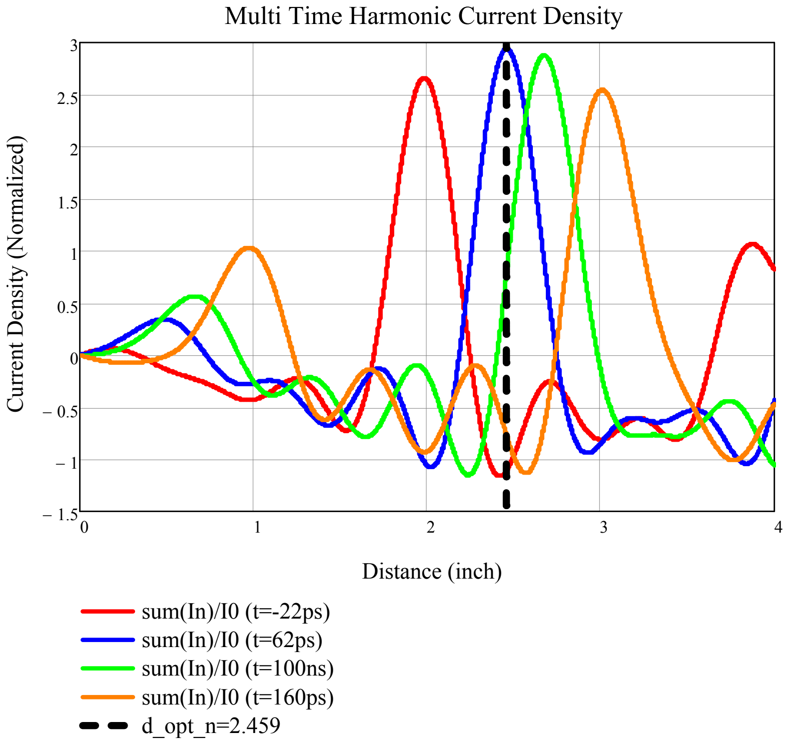

Figure 3.12: Plot of normalized multi time harmonic current density as a function of distance.

In this chapter we found that the resonant modes identified using MAGIC match very well with the measured resonant modes of the modulating cavity. From the resonant modes we can plot the dispersion relation of the modulating cavity. The dispersion relation of the modulating cavity is discrete and depends on the number of main and coupling cavities. The bunched beam leaving the cavity can be modeled using the multi harmonic ballistic current model.

CHAPTER 4: EXTRACTION CAVITY

The post-acceleration gap accelerates the beam bunches a second time before they enter the extraction cavity. This second acceleration minimizes the electrons' velocity spread. Microwaves are extracted from the beam bunches as they enter the extraction cavity. Each bunch becomes the source current J_z that generates the EM waves. Energy is extracted from the bunch, causing the electrons to slow down before entering the beam dump.

The extraction cavity consists of a circular drift tube joined to a rectangular waveguide, as shown in Figure 4.1. The left end of the waveguide has a metal plunger and the other end has an inductive iris. Beyond the iris, the waveguide has a step increase in height, from 0.67 inch to 1.42 inch, to match the height of a WR284 waveguide. All microwaves generated are absorbed using a waveguide load.

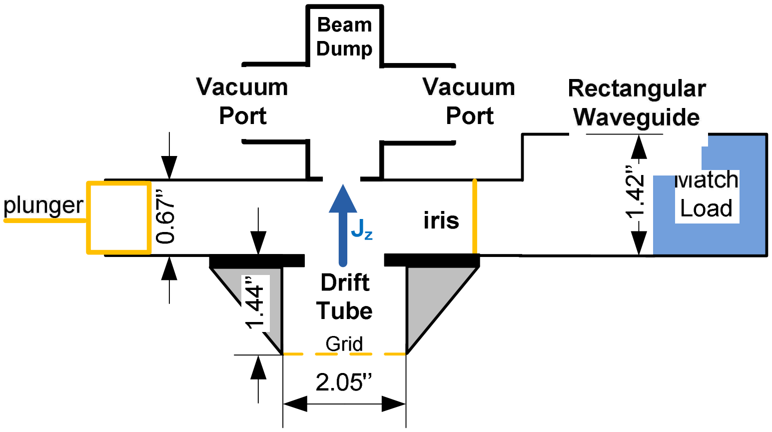

Figure 4.1: Side view of the UNM reltron extraction cavity.

Above the rectangular waveguide are the vacuum ports and beam dump. The vacuum ports use KF-50 O-ring seals that have steel mesh covering their internal diameter. This allows gasses to flow through the ports while reflecting microwaves back from the interfaces.

The extraction cavity is a 3.5 inch x 2.84 inch rectangular cavity that traps a portion of the microwaves and allows the rest to pass through the iris. Extraction is maximized by tuning the resonant frequency of the extraction cavity to match the modulation frequency of the beam. The extraction cavity is tuned using the back plunger and the side iris, as indicated in Figure 4.2. The axis of the drift tube is shifted by 1.1 inch from the center of the cavity so that the axis will coincide with the E_z maximum (Chapter 4.3).

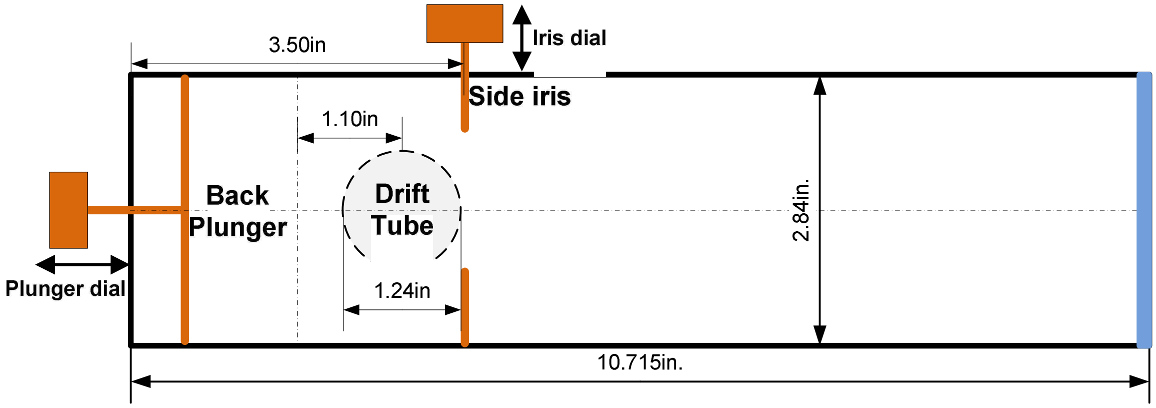

Figure 4.2: Top view of the extraction cavity.

The back plunger serves as a microwave reflector. Moving the plunger backwards increases the cavity volume, thereby decreasing the resonant frequency. Similarly widening the iris window decreases the resonant frequency. The iris can be modeled as a symmetric window consisting of two metal reflectors inserted on both sides of the waveguide. These reflectors act as barriers preventing the electric field from propagating down the waveguide. Figure 4.3 shows the front view of the iris and the E_z field distribution for the TE_{10} mode, and the equivalent circuit model of the waveguide, iris, and load.

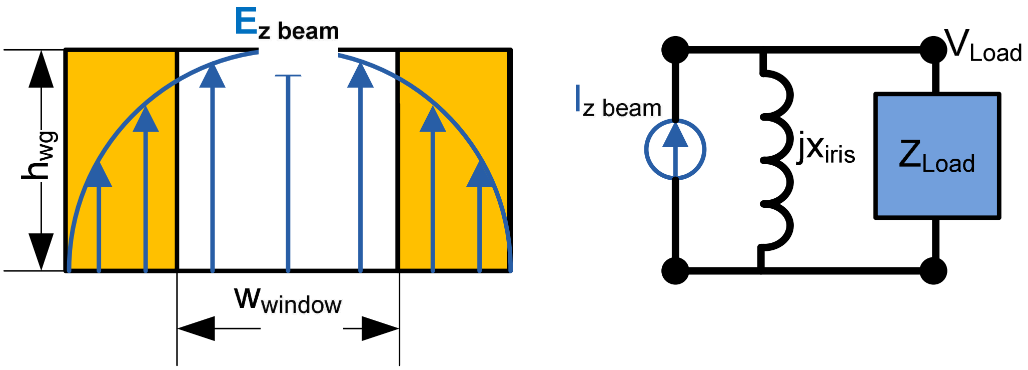

Figure 4.3 Front view of the iris (left) and the equivalent circuit model of the waveguide and iris (right).

The electron bunch is the current source that generates the E_z fields. A portion of the fields are reflected back and the rest are transmitted through the window. The maximum power stored in the cavity is limited by the resistive wall losses of the cavity. If we neglect resistivity, the waveguide and iris can be modeled as an ideal current source in parallel with an inductor and the load. The impedance of the iris is given by [2]

$$x_{iris} = \frac{h_{wg}}{\lambda_g} \tan^2\left(\frac{\pi w_{window}}{2h_{wg}}\right)\left[1 + \left\{\frac{3}{4}\sin^2\left(\frac{\pi w_{window}}{h_{wg}}\right)\right\}\left\{\left[1 - \left(\frac{2h_{wg}}{3\lambda_{wg}}\right)^2\right]^{-1/2} - 1\right\}\right], \tag{4.1}$$

where λ_g is the waveguide wavelength, h_{wg} is the height of the waveguide, and w_{window} is the window width of the iris. The thickness of the iris is negligible when compared to the length of the waveguide and is not included in the impedance formula.

The transfer function for the waveguide iris circuit model is given by

$$\begin{aligned} H(x_{iris}) &= \frac{V_{Load}}{I_{z\,beam}}, \\ &= \frac{jx_{iris} Z_{Load}}{Z_{Load} + jx_{iris}}, \\ &= \frac{j\overline{x}_{iris}}{1 + j\overline{x}_{iris}}, \end{aligned} \tag{4.2}$$

where $\overline{x}_{iris}$ is the impedance of the iris normalized to the load impedance.

When we decrease the width of the iris window we are isolating the current source from the load. This is verified by taking the limits as w_{iris} →0, $\overline{x}_{iris} \to 0$ and $H(x_{iris})$→0. When we increase the microwave frequency λ_g→0, $\overline{x}_{iris} \to \infty$ and $H(x_{iris})$→1. The inductive iris functions as a high-pass filter in the waveguide.

4.1 TRANSMISSION LINE MODEL OF EXTRACTION CAVITY

4.1.1 SINGLE EXTRACTION CAVITY TRANSMISSION LINE MODEL

The reflector plunger reduces the rectangular waveguide to a single port. The port is located after the iris and allows microwaves to leave the cavity. We model the single extraction cavity with the transmission line mode [2] shown in Figure 4.4. In our analysis we assume the height of the cavity to be uniform. The cavity walls are assumed to be PEC.

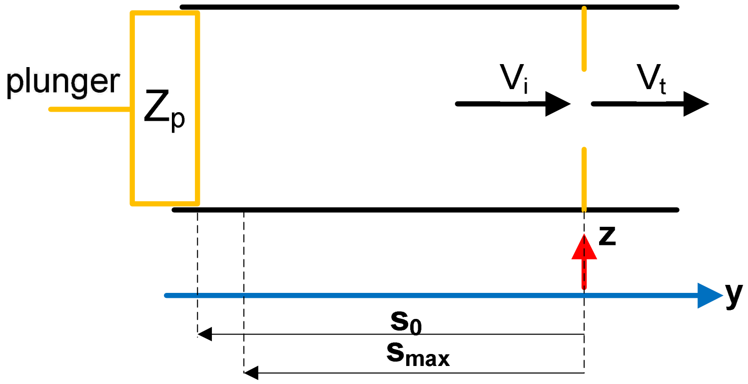

Figure 4.4 Single extraction cavity transmission line model.

Let jx be the shunt impedance of the iris normalized to the intrinsic impedance of the transmission line. The guide wavelength is given by

$$\lambda_g = \frac{2\pi}{\sqrt{k^2 - k_c^{\ 2}}} = \frac{2\pi}{k_z}, \tag{4.3}$$

where

$k = \omega\sqrt{\mu\varepsilon}$ and

$k_c^{\ 2} = k_y^{\ 2} + k_x^{\ 2}$.

Variables k_x, $k_{y,}$ and k_z are yjr wavenumbers in the x, y and z directions, respectively.

The impedance of a transmission line of length z with a short circuit as its load (Z_p=0) is given by Z_{in}=jZ_0 tan(k_zz) [24]. Equating the impedance of a shorted transmission line with the impedance of the iris yields

$$jx = j\tan(k_z s_0) = j\tan(\pi + k_z s_0), \tag{4.4}$$

where $k_z s_0$ is the phase angle. Solving the above, we obtain

$$\begin{aligned} k_z s_0 &= \tan^{-1} x - \pi \\ s_0 &= \frac{\tan^{-1} x - \pi}{k_z} \\ &= \frac{\lambda_g}{2\pi}\left(\tan^{-1} x - \pi\right). \end{aligned} \tag{4.5}$$

The position of the plunger is at s_0 and the voltage maximum will occur at $s_{\max} = s_0 + \lambda_g / 4$. The equivalent load seen by the wave moving in the positive y direction is the impedance of the iris in parallel with the impedance of the transmission line $\overline{Z}_L = \frac{jx}{jx+1}$. The reflection coefficient at the iris is given by

$$\begin{aligned}\Gamma_{ap} &= \frac{\overline{Z}_L - 1}{\overline{Z}_L + 1} \\ &= \frac{\frac{jx}{jx+1} - 1}{\frac{jx}{jx+1} + 1} \\ &= \frac{-1}{j2x+1}. \qquad (4.6)\end{aligned}$$

The voltage maximum occurs at

$$\begin{aligned}V_{\max} &= |V_i|\left(1 + |\Gamma_{ap}|\right) \\ &= |V_i|\left[1 + \left|\frac{1}{j2x+1}\right|\right] \\ &= |V_i|\left[1 + \frac{1}{\sqrt{4x^2+1}}\right] \\ &= |V_i|\left[\frac{\sqrt{4x^2+1}+1}{\sqrt{4x^2+1}}\right] \\ &\approx 2|V_i|\left[\frac{x^2+1}{4x^2+1}\right]^{1/2}. \qquad (4.7)\end{aligned}$$

Knowing

$$\begin{aligned}V_t &= V_i\left(1 + \Gamma_{ap}\right) \\ &= V_i\left(1 - \frac{1}{j2x+1}\right) \\ &= V_i\left(\frac{j2x}{j2x+1}\right),\end{aligned}$$

we obtain

$$|V_t| = |V_i|\sqrt{\left(\frac{4x^2}{4x^2+1}\right)}. \qquad (4.8)$$

Substituting the above into V_{max}, we obtain

$$V_{\max} = |V_i| \left[\frac{\sqrt{4x^2+1}+1}{\sqrt{4x^2+1}} \right]$$

$$= |V_t| \sqrt{\left(\frac{4x^2+1}{4x^2} \right)} \left[\frac{\sqrt{4x^2+1}+1}{\sqrt{4x^2+1}} \right]$$

$$= \frac{|V_t|}{2x} \left[\sqrt{\left(4x^2+1\right)}+1 \right]$$

$$\approx \frac{V_t}{x}\sqrt{x^2+1} \,. \tag{4.9}$$

We know that the power transmitted through the iris is dependent on the reflection coefficient $P_t = \frac{V_i^2}{2}\left(1-\Gamma_{ap}{}^2\right)$. The transmitted power can also be calculated as a function of the transmitted wave and waveguide impedance. The impedance for the TE mode in rectangular waveguide is given by

$Z_{TE} = \eta \left[1 - \left(\frac{\lambda_c}{\lambda} \right)^2 \right]^{-1/2} = \eta \frac{\lambda_g}{\lambda}$. The transmitted power is given by

$$P_t = \frac{V_t^2}{2Z_{TE}}$$

$$= \frac{V_t^2}{754}\frac{\lambda}{\lambda_g} \,. \tag{4.10}$$

The shunt impedance of the cavity is approximated by Atwater [25] as

$$R_{sh} = \frac{V_{\max}{}^2}{P_t(w_{wg}/h_{wg})}$$

$$= 754\frac{V_{\max}{}^2}{V_t^2}\frac{\lambda_g}{\lambda}\left(\frac{h_{wg}}{w_{wg}}\right), \tag{4.11}$$

where w_{wg} is the width of the waveguide.

Optimum extraction occurs when the beam impedance is equal to the shunt impedance $R_{beam} = R_{sh}$, which yields

$$\frac{V_{beam}}{MCI_{beam}} = 754\frac{V_{\max}{}^2}{V_t^2}\frac{\lambda_g}{\lambda}\left(\frac{w_{wg}}{h_{wg}}\right). \tag{4.12}$$

Using the above derivations we can calculate the iris parameters for a cavity height of 0.67 inch with resonant frequency 2.75 GHz, which are summarized in Table 4.1.

Table 4.1: Extraction cavity parameters.

Parameter	**Value**
Frequency f	2.75 GHz
Guide Wavelength λ_g	16.64 cm (6.55 in)
Guide impedance Z_{TE}	575 Ω
Window width w_{iris}	3.614 cm (1.42 in)
shunt impedance x	0.4507 Ω
plunger position s_0	-7.2 cm (-2.835 in)
maximum voltage s_{max}	-3.039 cm (-1.197 in)
Cavity Impedance R_{sh}	1.608 kΩ
Beam Voltage V_{beam}	80 kV
Beam Current I_{beam}	250 A
Modulating Coefficient MC	0.2
Beam Impedance R_{beam}	1.6 kΩ

From the model, we can calculate the width of the iris window as we increase the modulation coefficient of the beam, as shown in Table 4.2.

We plot the percentage of the iris window width normalized to the width of the rectangular waveguide (2.84 inch) in Figure 4.5. We find that the window size is almost linearly proportional to the modulation coefficient. We have to open the iris wider as the modulation coefficient increases. For a modulation coefficient of unity, only 25% of the waveguide is covered by the iris.

Table 4.2: Iris window width.

MC	w_{iris} (inch)
0.2	1.420
0.3	1.541
0.4	1.631
0.5	1.710
0.6	1.784
0.7	1.855
0.8	1.928
0.9	2.005
1	2.103

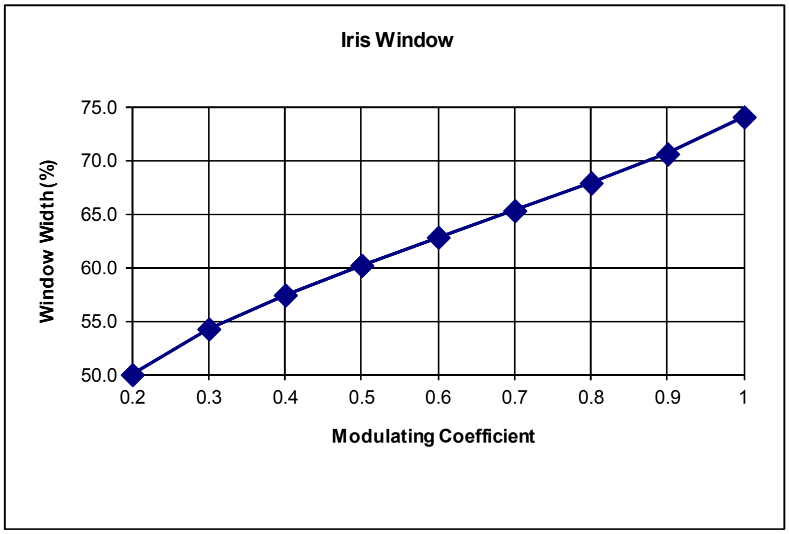

Figure 4.5: Plot of the normalized iris window width as a function of modulation coefficient.

The window width determines the iris impedance. From the iris impedance, we calculate the distance between the plunger and the iris. Figure 4.6 shows the plunger distance for the increasing window widths.

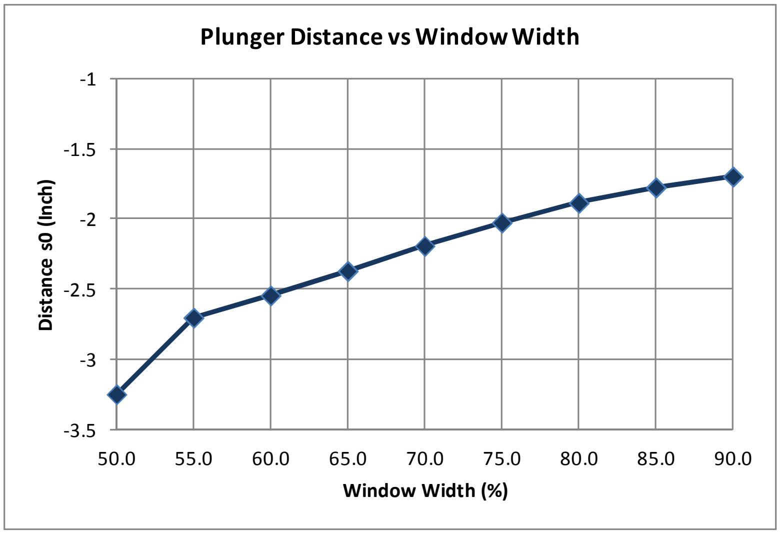

Figure 4.6: Plot of the plunger distance as a function of normalized iris window width

4.1.2 DUAL EXTRACTION CAVITY TRANSMISSION LINE MODEL

The position of the maximum voltage in the single extraction cavity depends on the position of the plunger which depends on the impedance of the iris *jx*. The voltage maximum shifts every time we change the iris window width. In order to fix the position of the voltage maximum, we propose the dual extraction cavity.

The dual extraction cavity is designed to be axisymmetric, which will divide the microwave power equally between two extraction ports. Symmetry also allows us to fix the voltage maximum on the center axis of the cavity. We model the dual extraction cavity as two transmission lines of equal length, joined together at the axis with irises placed equidistant from the center (Figure 4.7).

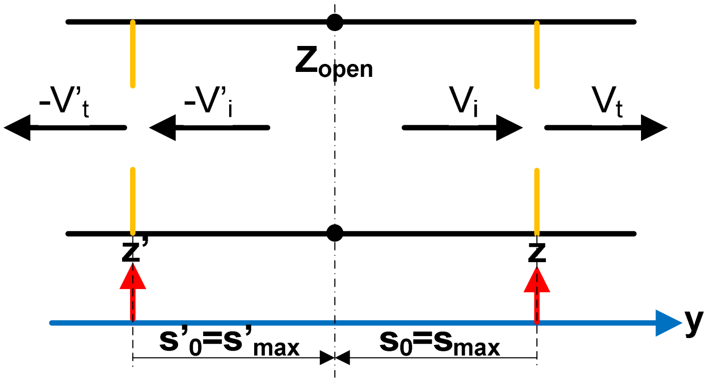

Figure 4.7: Dual extraction cavity transmission line model.

The center axis is modeled as an open circuit, which places the voltage maximum in the middle. As the model is symmetric, dimensions calculated for one line can be applied to the other line. The impedance of a transmission line of length z with an open circuit as its load ($Z_{open}=\infty$) is given by $Z_{in}= -jZ_0 \cot(k_z z)$.

Equating the impedance of an open circuit transmission line with the impedance of the iris

$$jx = -j\cot(k_z s_0) = j\tan(\pi/2 + k_z s_0), \tag{4.13}$$

where $k_z s_0$ is the phase angle. Solving the above, we obtain

$$\pi/2 + k_z s_0 = \tan^{-1} x$$

$$s_{0\_\pi/2} = \frac{\tan^{-1} x - \pi/2}{k_z}$$

$$= \frac{\lambda_g}{2\pi}\left(\tan^{-1} x - \pi/2\right). \tag{4.14}$$

Since the line has an open circuit as its load, the voltage maximum will occur at $s_{\max} = s_0$, which is at the center axis. In the extraction cavity the iris has to be placed at least 1 inch away from the center, otherwise it will lie inside the drift tube radius. We can generate the next set of solutions phase shifted away from the axis by employing $\tan(\theta) = \tan(\theta+\pi)$. The iris distance is now given by

$$s_{0\_3\pi/2} = \frac{\lambda_g}{2\pi}\left(\tan^{-1} x - \frac{3\pi}{2}\right). \tag{4.15}$$

The window width sets the iris impedance which is matched to the beam impedance. As such, the methodology to determine the window width for the dual extraction cavity is identical to the methodology derived for the single extraction cavity. After we have determined the window width, we solve for the position of the iris using $s_{0\_\pi/2}$ or $s_{0\_3\pi/2}$. Figure 4.8 plots the iris distance for the dual extraction cavity phase shifted by π/2 and 3π/2.

4.2 SPACE CHARGE WAVES INSIDE EXTRACTION CAVITY

In Appendix A, we show that the dispersion relation of the space charge waves inside the reltron's electron beam can be approximated by the Breizman and Ryutov space charge waves dispersion relation in polynomial form. We reproduce the Breizman and Ryutov [26] polynomial dispersion relation

$$\left(k_z - \frac{\omega}{v_0}\right)^2 = \left(k_z{}^2 - \frac{\omega^2}{c_0{}^2}\right)\psi \tag{4.16}$$

where $\psi = \frac{2q_e I_b}{m_e v_0{}^3 \gamma_0{}^3} \ln \frac{r_{wg}}{r_b}$ and I$_b$ is the unperturbed beam current.

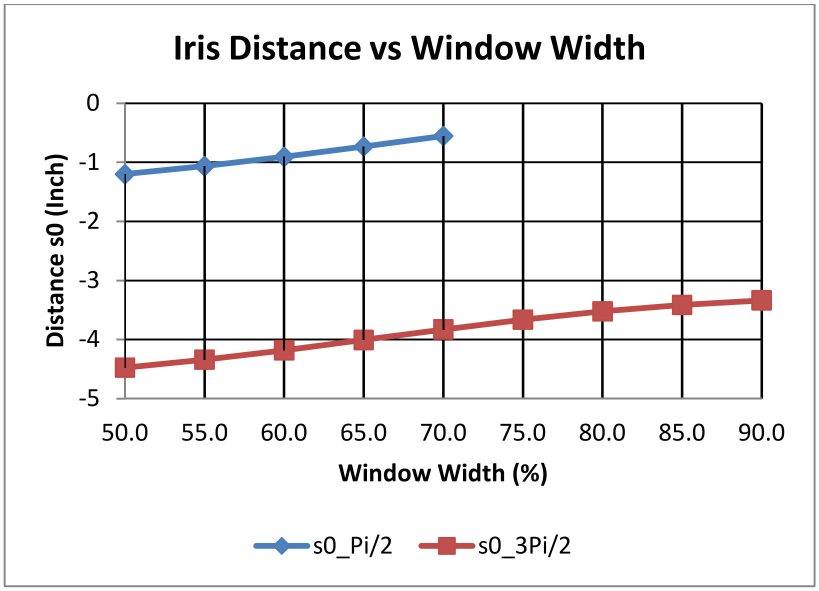

Figure 4.8: Plot of the iris distance as a function of normalized iris window width.

Differentiating equation (4.16) with respect to k$_z$

$$2\left(k_z - \frac{\omega}{v_0}\right)\left(1 - \frac{1}{v_0}\frac{d\omega}{dk_z}\right) = \left(2k_z - \frac{2\omega}{c_0{}^2}\frac{d\omega}{dk_z}\right)\psi$$

$$\left(k_z - \frac{\omega}{v_0}\right)\left(1 - \frac{1}{v_0}\frac{d\omega}{dk_z}\right) + \frac{\omega}{c_0{}^2}\frac{d\omega}{dk_z}\psi = k_z\psi$$

$$\left(\frac{1}{v_0}\left(\frac{\omega}{v_0} - k_z\right) + \frac{\omega}{c_0{}^2}\psi\right)\frac{d\omega}{dk_z} = k_z\psi + \frac{\omega}{v_0} - k_z$$

$$\left(\frac{1}{v_0}\left(\frac{\omega}{v_0} - k_z\right) + \frac{\omega}{c_0{}^2}\psi\right)\frac{d\omega}{dk_z} = k_z\psi + \frac{\omega}{v_0} - k_z.$$

By definition the group velocity is given by $v_{group} = \frac{d\omega}{dk_z}$. Replacing $\frac{d\omega}{dk_z}$ with v$_{group}$ we obtain

$$v_{group} = \left(k_z \psi + \frac{\omega}{v_0} - k_z \right) \left(\frac{1}{v_0} \left(\frac{\omega}{v_0} - k_z \right) + \frac{\omega}{c_0^2} \psi \right)^{-1} . \tag{4.17}$$

For the fast wave $\omega > k_z v_0$, so $\omega / v_0 - k_z > 0$. Similarly, for the slow wave $\omega < k_z v_0$, so $\omega / v_0 - k_z < 0$. This implies the fast wave's group velocity v$_{group\_fast}$ is positive definite while the slow wave group velocity v$_{group\_slow}$ can be positive or negative definite.

When the wave is extracted from the beam, the fast wave with positive group velocity will always travel in the forward direction and leave the extraction port. The slow wave will travel in the reverse direction if its group velocity is negative, propagating backwards towards the modulating cavity. In order to prevent the slow wave from traveling backwards, we design the cutoff frequency of the drift tube to be much lower than the resonant frequency of the space charge wave. A sufficiently long drift tube will prevent backward propagation of any wave as the wave becomes attenuated within a few wavelengths. Energy is trapped inside the extraction cavity and only leaves through the iris.

Using our numerical model (A.20), we plot the space charge waves inside the drift tube for a 75 keV, 500 A beam (Figure 4.9). The beam radius is 0.75 inch and the drift tube radius is 1.025 inch. The beam voltage is higher than the voltage in the modulating cavity because of the post acceleration voltage. The beam pinches when it passes through the grid covering the entrance of the drift tube, so the beam diameter is smaller than the diameter inside that modulating cavity. The space charge waves excited in the modulating cavity oscillates at 2.82 GHz. Using 2.82 GHz as the resonant frequency, we see that the wavenumber inside the drift tube is 128 rad/m.

Having obtained the resonant frequency and wavenumber, we plot the longitudinal electric field inside the beam (A.15) and in the vacuum between the beam and the drift tube (A.16). Figure 4.10 shows the radial distribution of the E$_z$ field inside the beam (red) and inside the vacuum (blue) at the origin of the drift tube z=0.

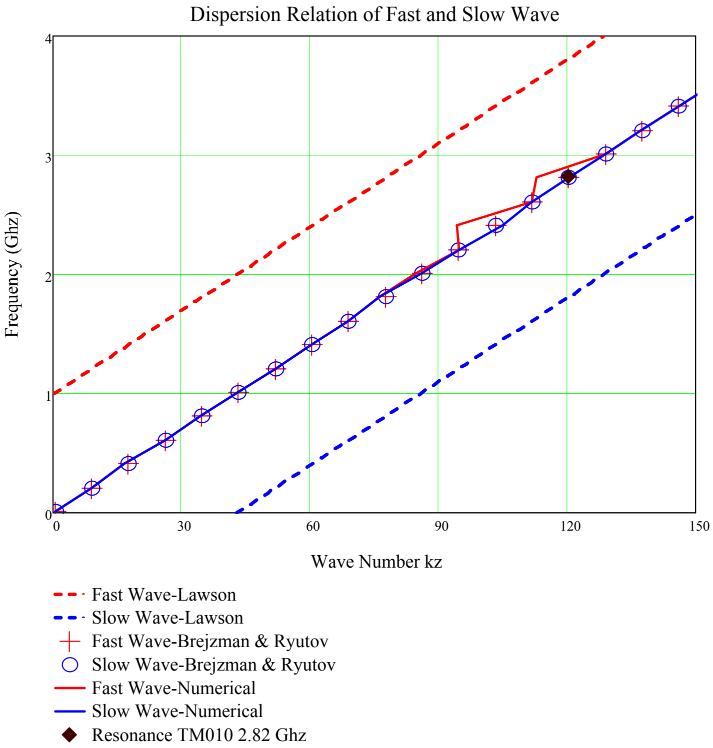

Figure 4.9: Dispersion relation of the space charge wave on the electron beam inside the drift tube.

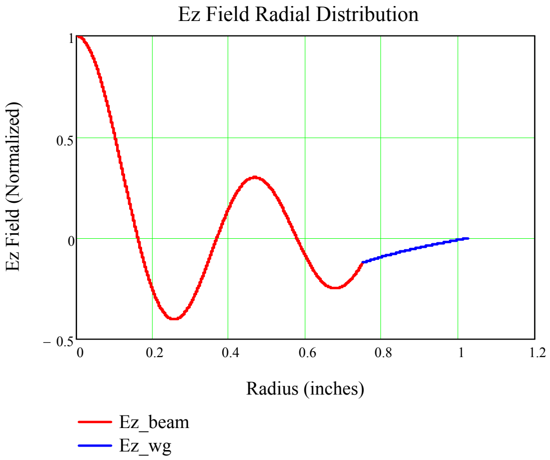

Figure 4.10: E_z field inside drift tube.

From our derivation, we see that space charge waves are spatially periodic in the longitudinal direction. We can maximize microwave extraction by ensuring that the current density peaks at the middle of the extraction cavity. We substitute $E_z = AJ_0(rk_\perp m)e^{-i(k_z z)}$ for the space charge current density (A.8)

$$J_z = \mathrm{Re}\left(\frac{-iq_e^{\;2}\omega n_0 E_z}{\gamma_0^{\;3} m_e(\omega - k_z v_0)^2}\right)$$

$$= \mathrm{Re}\left(\frac{-iq_e^{\;2}\omega n_0}{\gamma_0^{\;3} m_e(\omega - k_z v_0)^2} AJ_0(rk_\perp m)e^{-i(k_z z)}\right)$$

$$= \frac{Aq_e^{\;2}\omega n_0}{\gamma_0^{\;3} m_e(\omega - k_z v_0)^2} J_0(rk_\perp m)\cos(n\pi - k_z z), \tag{4.18}$$

where n=3/2, 5/2, 7/2,… J_z peaks when $\cos(n\pi - k_z z) = 1$ giving $n\pi - k_z z = 0, 2\pi...$ For the case $n\pi - k_z z = 0$, the first peak occurs at

$$z_{n=3/2} = \frac{3\pi}{2k_z} = 1.449'' \tag{4.19}$$

and the next peak occurs at

$$z_{n=5/2} = \frac{5\pi}{2k_z} = 2.415''. \tag{4.20}$$

For the case $n\pi - k_z z = 2\pi$, the first peak occurs at

$$\hat{z}_{n=5/2} = \frac{1}{k_z}\left(\frac{5\pi}{2} - 2\pi\right) = 0.483''. \tag{4.21}$$

The subsequent peaks generated by higher values of n=7/2, 9/2…. equal the peaks in the $n\pi - k_z z = 0$ case. We tabulate the currents peaks in Table 4.3.

Table 4.3: Current density peaks in the modulating cavity.

	Current Peak (inch)
$\hat{z}_{n=5/2}$	0.483
$z_{n=3/2}$	1.449
$z_{n=5/2}$	2.415

The length of the drift tube to the middle of the extraction cavity is

$$\begin{aligned}\text{height} &= \text{length}_{\textit{drift tube}} + \frac{\text{Height}_{wg}}{2} \\ &= 1.44 + \frac{0.67}{2} \\ &= 1.775''.\end{aligned}$$

The space charge wave current peaks at the second spatial harmonic $z_{n=3/2}$, which is 0.339 inch below the midpoint of the extraction cavity. We can adjust the wave current peak to occur exactly at the cavity midpoint by increasing the beam voltage, which increases the beam velocity. This decreases the wavenumber, which increases $z_{n=3/2}$.

The analytical model of the single and dual extraction cavity gives us a good estimate of the physical dimensions of the extraction cavity and the iris. We use these dimensions as the initial parameters for performing HFSS simulations.

4.3 HFSS SIMULATIONS OF A SINGLE EXTRACTION CAVITY

The single extraction cavity transmission line model gives a good estimate of the position of the iris and reflector plunger s_0 and the width of the window w_{iris}. However, the extraction cavity includes the cylindrical drift tube, rectangular waveguide, and beam dump. The volume of these structures influences the resonant frequency of the cavity. We use HFSS v12 to calculate the actual resonant frequencies.

We place the reflector at -1.75 inch and the iris at 1.75 inch relative to the center axis (Figure 4.11). The cavity walls are PEC and the cavity is assumed to be vacuum. The cavity is excited by port 1 and port 2 using the wave port function. A wave is launched from each port and exits the cavity through the initial port or other wave ports. Microwaves can only enter and leave the simulation space through wave ports.

Wave port is a built in function that models modes in semi-infinitely long waveguides with cross section identical to the surface of the cavity port. Wave port calculates the field distribution on the port surface that becomes the excitation source that generates a wave that flows into the cavity. The wave leaves the cavity through the ports and does not return to the cavity. By monitoring the fields at the wave ports, we obtain the S parameters of each port. We perform a frequency sweep from 2.7 GHz to 2.85 GHz using steps of 0.001 GHz.

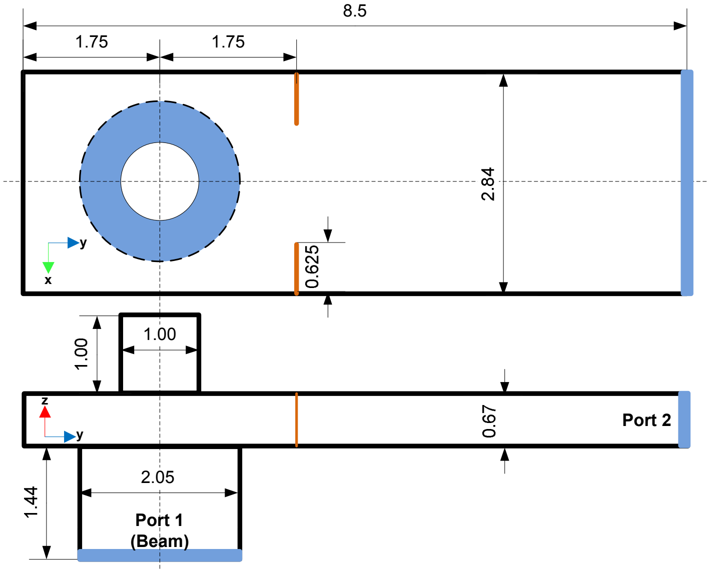

Figure 4.11 Top and side view of a single extraction cavity.

Figure 4.12 shows a 3D view of the single extraction cavity simulated in HFSS.

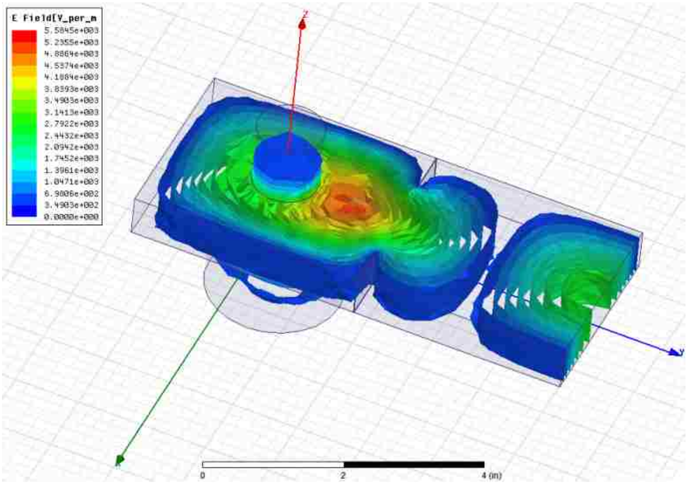

Figure 4.12 HFSS model of single extraction cavity.

Figure 4.13 and Figure 4.14 show the S_{11} and S_{21} of the single extraction cavity, respectively. The highest point of the S_{21} is at 2.757 GHz with magnitude -28.6 dB and S_{11} corresponding to the resonant frequency is -63.2 dB. The cavity's S matrix is symmetric as the magnitude of S_{21} is equal to S_{12} for the frequency range under consideration.

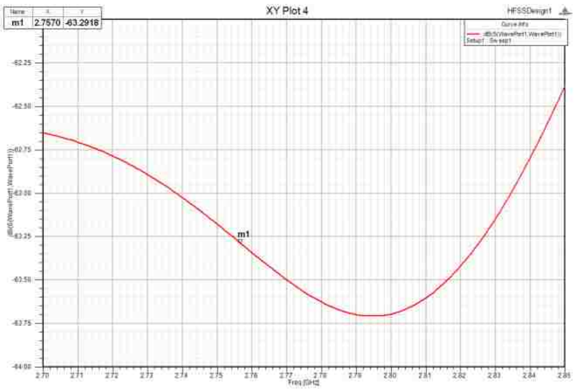

Figure 4.13. Single extraction cavity S_{11}.

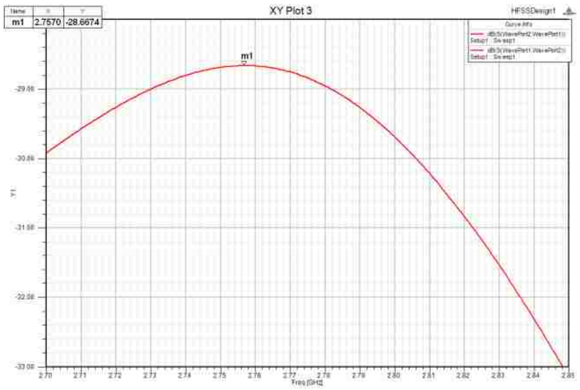

Figure 4.14. Single extraction cavity S_{21}.

A low S_{11} is desirable as it prevents the waves from traveling backward towards the modulating cavity. The highest point on the S_{21} curve represents the frequency where the wave passes through the cavity with minimal attenuation. The attenuation from the drift tube alone is -17.2 dB, so the S_{21} due to the transition from circular waves to rectangular waves is -11.4 dB. As the S_{21} is equal to S_{12}, waves in the rectangular waveguide undergo the same attenuation when flowing back to the drift tube.

The vector and contour plots of the electric fields inside the cavity are show in Figure 4.15 and Figure 4.16, respectively. The plots are generated from a cut plane through the origin with its normal parallel to the x-axis.

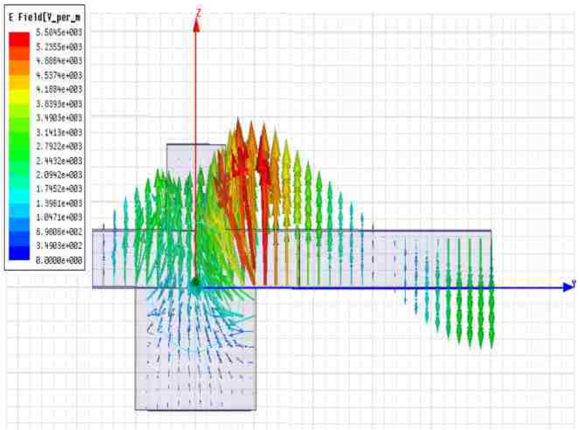

Figure 4.15. Single extraction cavity side view vector plot.

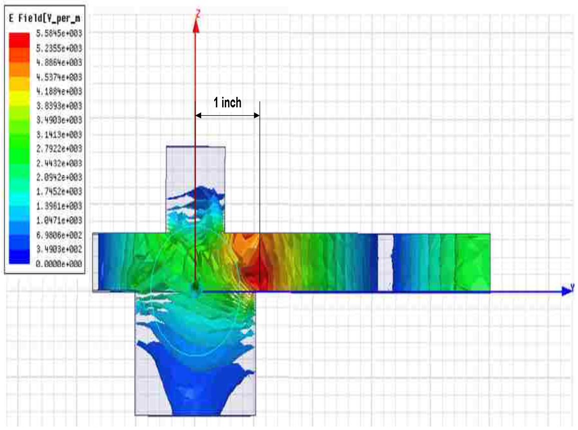

Figure 4.16. Single extraction cavity side view contour plot.

The peak electric field is 1 inch to the right of the center axis of the drift tube, 0.75 inch to the left of the iris. The peak electric field calculated by the 1D model is at

s_{max} = -1.197 inch left of the iris. Widening the iris window moves the peak electric field closer to the iris. Inside the drift tube the electric fields are not symmetric about the axis. The electric forces exerted the beam are not uniform, resulting in beam dispersion.

Figure 4.17 is a top view contour plot of the electric fields inside the rectangular waveguide. We observe the bulk of the electric fields resonating inside the cavity and a portion of the fields flowing past the iris to the output ports. The iris window controls the amount of electric field leaking out of the cavity. The fields peak along the y-axis and decay as they approach the cavity and iris walls.

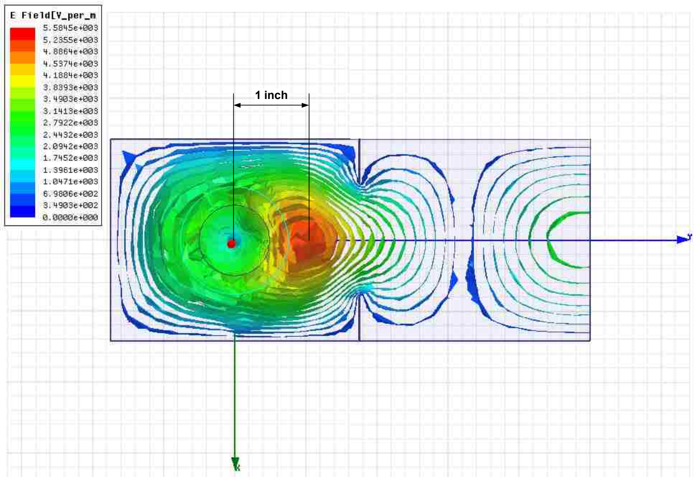

Figure 4.17. Single extraction cavity top view contour plot.

As the peak electric field is close to the iris, the actual extraction cavity has its drift tube shifted by 1.1 inch along the length of the waveguide. The beam propagating through the drift tube will see the E_z maxima as the beam axis coincides with the peak electric field. The E_z field distribution will also be more symmetric, thereby reducing beam dispersion.

4.3.1 SINGLE EXTRACTION CAVITY WITH WR284 WAVEGUIDE

The extraction cavity of the UNM low power reltron includes a WR284 rectangular waveguide, cross section 2.84 inch x 1.34 inch, connected to the cavity after the iris (Figure 4.18). We use the eigenmode solver in HFSS v12 to determine the resonant frequencies that can exist in the single extraction cavity with WR284 waveguide.

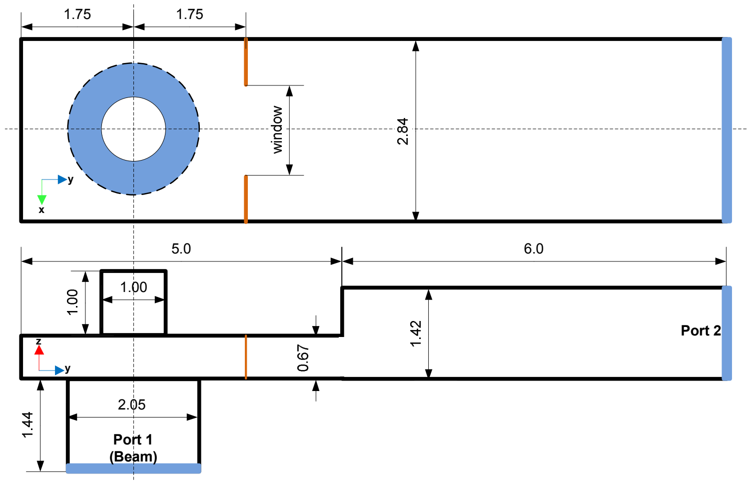

Figure 4.18 Top and side view of a single extraction cavity with WR284 waveguide.

Microwaves leaving the extraction cavity see a change in waveguide height from 0.67 inch in the extraction cavity to 1.34 inch in the WR284 waveguide. However, the modes we are interested in, TE_{m0} modes, where m=1,2,3…, are unaffected by the waveguide height.

The eigenmode solver calculates the resonant frequencies from the spatial mesh generated inside the simulation space. An infinite number of eigenmodes can exist inside the cavity. Furthermore, the length of the WR284 waveguide will affect the resonant frequencies as the EM waves have to spatially distribute themselves inside the cavity and still satisfy boundary conditions. As such, we need to determine which resonant modes are generated in the extraction cavity flowing into the WR284 waveguide and which modes exist because of the WR284 waveguide. We first calculate the TE_{10n} resonant modes [27], where n=1,2,3…, for WR284 rectangular cavities of length 11 inch and 3.5 inch, respectively (Table 4.4). Next we simulate the cavity with WR284 waveguide in HFSS v12. We begin our search at 2 GHz and search upwards in frequency for a total of 10 eigenmodes. We set the solver to converge for real frequencies only. Table 4.5 lists the eigenmodes and Figure 4.19 plots the eigenmodes for window widths varying from 2.04 inch to 1.04 inch, respectively.

Table 4.4: WR284 rectangular cavity eigenmodes.

TE_{10n}	Cavity Length 11 inch Frequency (GHz)	Cavity Length 3.5 inch Frequency (GHz)
1	2.146	2.676
2	2.339	3.961
3	2.628	-
4	2.987	-
5	3.393	-

Table 4.5: Eigenmodes in single extraction cavity with WR284 waveguide.

mode	Window 2.04 inch Frequency (GHz)	Window 1.84 inch Frequency (GHz)	Window 1.64 inch Frequency (GHz)	Window 1.42 inch Frequency (GHz)
1	2.147	2.151	2.153	2.155
2	2.288	2.310	2.331	2.347
3	2.481	2.504	2.536	2.570
4	2.756	2.767	2.787	2.816
5	2.966	2.966	2.966	2.967
6	3.289	3.298	3.310	3.325
7	3.469	3.478	3.491	3.511
8	3.826	3.827	3.829	3.831
9	3.984	3.988	3.993	3.996
10	4.188	4.196	4.197	4.197

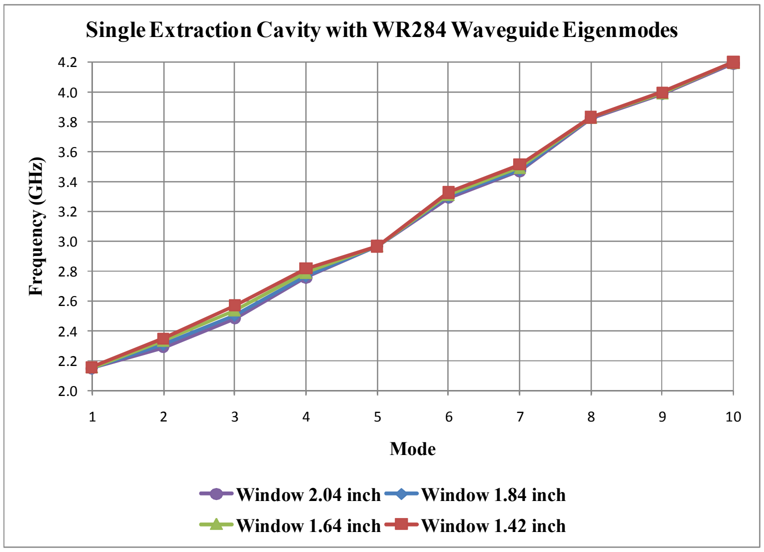

Figure 4.19 Eigenmodes in Single Extraction Cavity with WR284 waveguide.

Comparing with the resonant frequencies of a 3.5 inch WR284 cavity, we deduce that mode 4 (TE_{101}) and mode 8 (TE_{102}) are resonant modes that are excited within the reflector and iris of the extraction cavity. We generate a contour plot of the electric field magnitude for mode 4 and mode 8 in Figure 4.20 and Figure 4.21, respectively. The window width is set to 1.42 inch in both plots. The electric fields start in the reflector-iris region and flow into the WR284 waveguide.

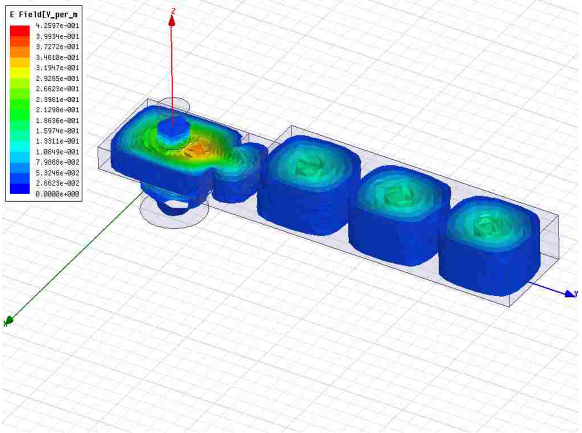

Figure 4.20. Mode 4 (TE_{101}) in extraction cavity with WR284 waveguide.

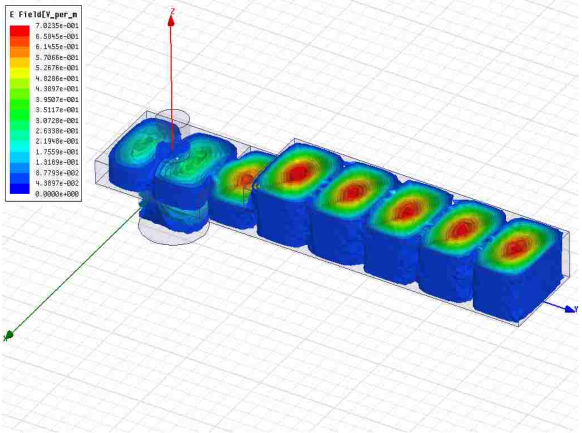

Figure 4.21. Mode 8 (TE_{102}) in extraction cavity with WR284 waveguide.

We observe that mode 8 has 8 electric field crests while mode 4 has four crests. This validates our theory that mode 4 is the TE_{101} mode which has twice the guide wavelength of mode 8 which is the TE_{102} mode.

4.4 HFSS SIMULATIONS OF A DUAL EXTRACTION CAVITY

We simulate the dual extraction cavity in HFSS v12 using the dimensions calculated from the dual extraction cavity transmission line model. We tune the iris position until we achieve resonance at 2.75 GHz. Both irises are placed 1.7362 inch from the center axis, as shown in Figure 4.22. The use of two iris windows increases the amount of EM fields flowing out of the cavity volume. As such, the two irises are placed close to the center axis compared to the iris placement in the single extraction cavity.

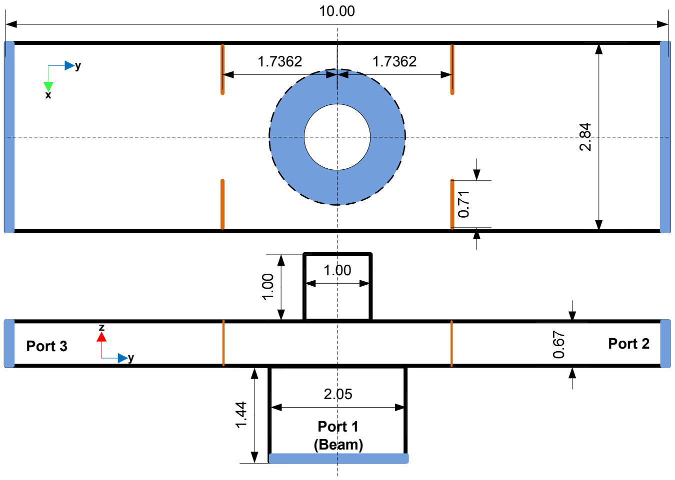

Figure 4.22 Top and side view of a dual extraction cavity.

The cavity walls are PEC and the cavity is assumed to be a vacuum. The cavity is excited by wave ports 1, 2, and 3. Figure 4.23 shows a 3D view of the dual extraction cavity simulated in HFSS.

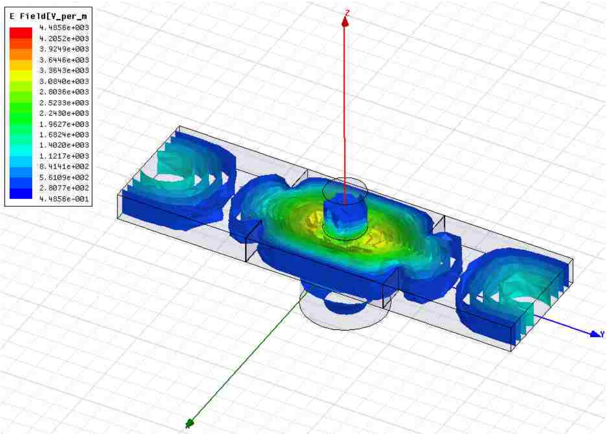

Figure 4.23 Electric field contour of dual extraction cavity.

Figure 4.24 and Figure 4.25 show the S_{21}/S_{31} and S_{22}/S_{33} of the dual extraction cavity, respectively. The S_{22}/S_{33} resonates at 2.753 GHz with magnitude -39.4 dB. The S_{21}/S_{31} corresponding to the resonant frequency is -46 dB.

The dispersion relation of port 2 and port 3 shows both ports are in phase with each other, as indicated in Figure 4.26.

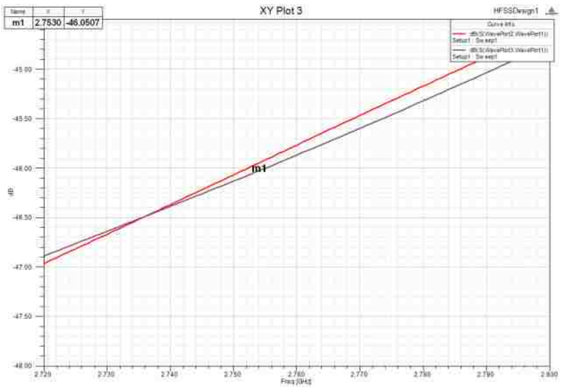

Figure 4.24: Dual extraction cavity S_{21} and S_{31}.

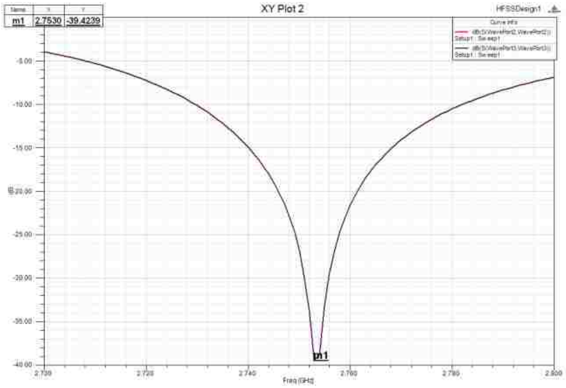

Figure 4.25: Dual extraction cavity S_{22} and S_{33}.

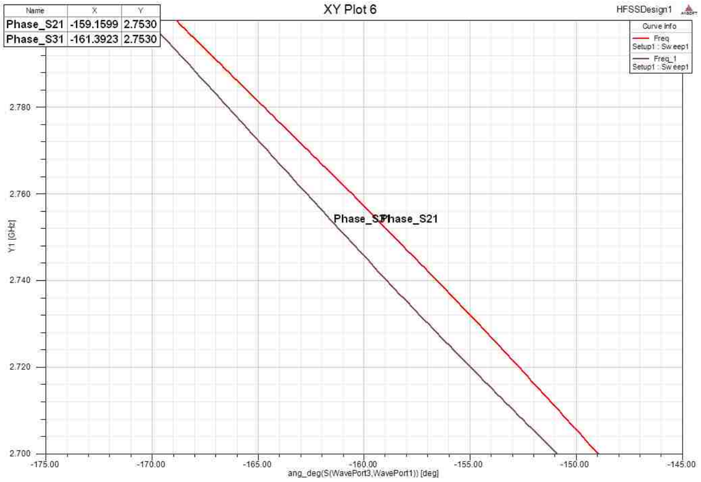

Figure 4.26 Dispersion relation of port 2 and port 3.

The vector and contour plots of the electric field distribution inside the cavity are show in Figure 4.27 and Figure 4.28, respectively. With the use of symmetry, we have restored the peak electric field to the center axis of the drift tube.

Figure 4.29 is a top view contour plot of the electric fields inside the rectangular waveguide. The electric fields flow out of both irises symmetrically, thus dividing the microwave power between ports 2 and 3.

We repeat the simulations using brass walls with conductivity 1.5x10^7 S/m to examine the effect of resistance on the resonant frequency. The S_{22}/S_{33} dips to 2.749 GHz (Figure 4.31), which is 4 MHz lower than the cavity with PEC walls. The S_{22}/S_{33} magnitude is -45.3 dB at resonant which is 5.9 dB lower than the cavity with PEC walls.

The S_{11} corresponding to the resonant frequency is -40.1 dB Figure 4.30, which is 5.9 dB higher for the PEC cavity. More microwaves are reflected back through port 1 because of the wall resistivity.

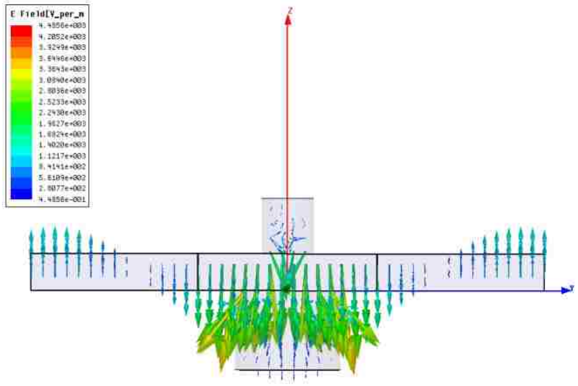

Figure 4.27. Dual extraction cavity side view vector plot.

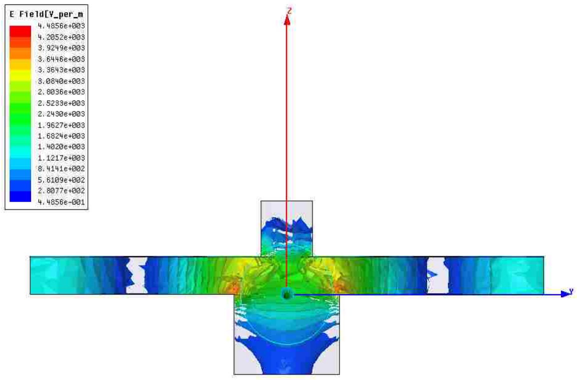

Figure 4.28. Dual extraction cavity side view contour plot.

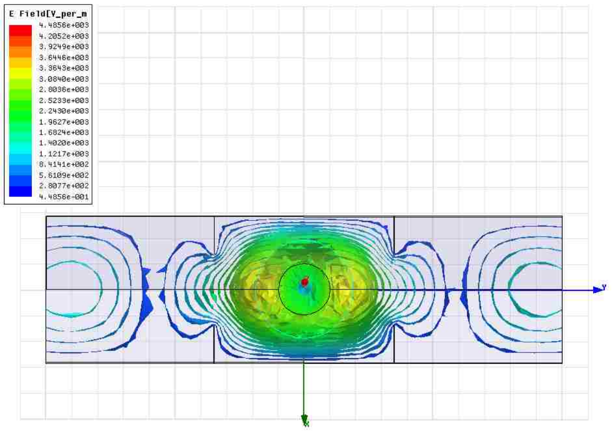

Figure 4.29. Dual extraction cavity top view contour plot.

4.5 S PARAMETERS OF UNM LOW POWER RELTRON

We performed measurements of the extraction cavity's S parameters using the VNA. We mounted a WR284 coaxial to waveguide adapter at the flange of the rectangular waveguide and measured the S_{11} of the cavity through the adapter. Figure 4.32 plots the S_{11} parameter for window width 1.705 inch and Figure 4.33 for window width 1.922 inch.

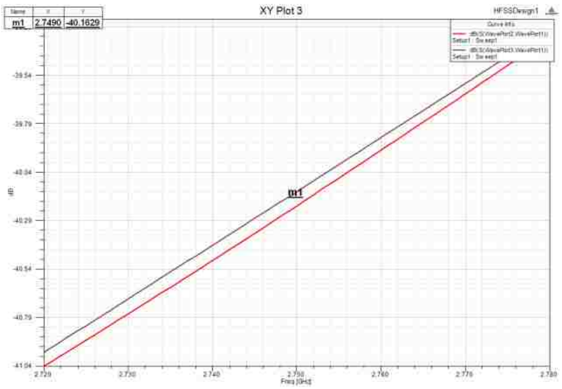

Figure 4.30 Brass walled dual extraction cavity S_{21} and S_{31}.

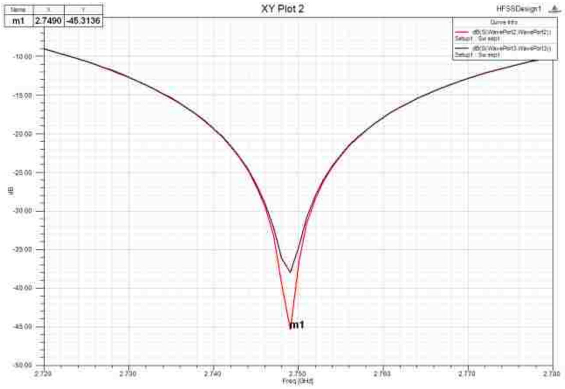

Figure 4.31 Brass walled dual extraction cavity S_{22} and S_{33}.

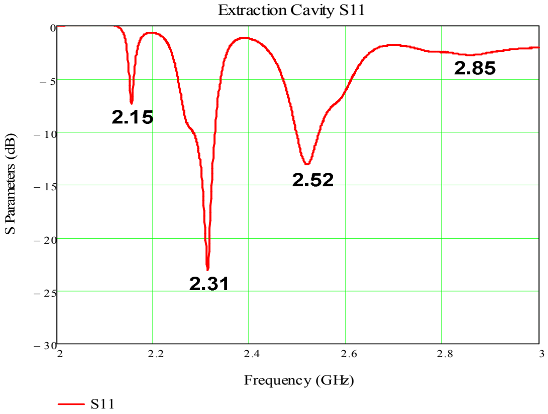

Figure 4.32 Extraction cavity S_{11} for window width 1.705 inch.

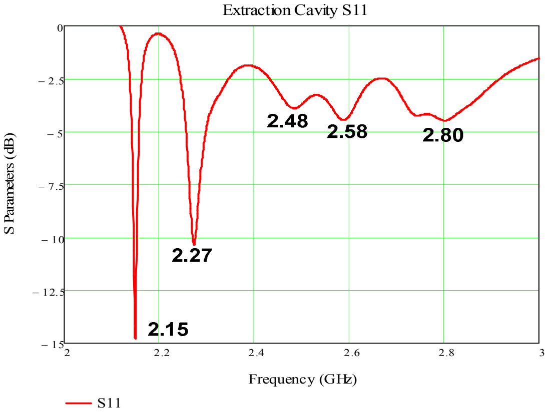

Figure 4.33 Extraction cavity S_{11} for window width 1.922 inch.

For both measurements we retract the back plunger fully to give a cavity length of 3.5 inch. The resonant frequency closest to the π/2 mode (2.78 GHz) is 2.8 GHz. For window width 1.705 inch, the dominant S_{11} is 2.31 GHz with magnitude -23 dB. At 2.85 GHz, the S_{11} magnitude is -2.76 dB (Figure 4.34). For window width to 1.922 inch, the dominant S_{11} parameter is 2.15 GHz with magnitude -14.7 dB. At 2.8 GHz, the S_{11} magnitude is -4.48 dB (Figure 4.35).

For any window width, decreasing the cavity length does not improve the 2.8 GHz resonant mode as we do not see a significant drop in the magnitude of the S_{11} parameter at 2.8 GHz. The S_{11} of the 2.5 GHz resonant mode decreases as we extend the back plunger deeper into the cavity. When we extend both the iris and back plunger to their maximum distance into the cavity, we improve the resonant strength of the 2.5 GHz resonant mode (S_{11} decreases), while increasing the S_{11} of 2.8 GHz resonant mode.

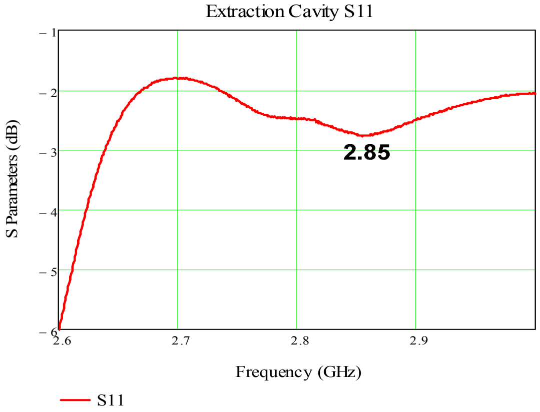

Figure 4.34 Window width 1.705 inch, S_{11} from 2.6 GHz – 3 GHz.

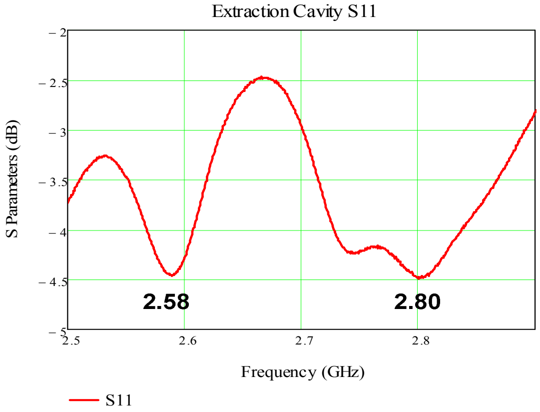

Figure 4.35 Window width 1.922 inch, S_{11} from 2.6 GHz – 3 GHz.

From our eigenmode simulations (Table 4.5) we know that the resonant frequencies at 2.15 GHz, 2.27-2.31 GHz, and 2.48 - 2.52 GHz are due to the presence of the WR284 waveguide. The frequency 2.80 – 2.85 GHz is the resonant frequency of a wave oscillating between the back plunger and the irises.

The resonant frequency of the extraction cavity is close to the resonant frequency of the modulating cavity. Even with the presence of an electron beam, both cavities will resonate with each other.

CHAPTER 5: ELECTROSTATIC ANALYSIS

5.1 STATIC ELECTRIC FIELDS IN RELTRON

High electric fields inside the A-K gap and post-acceleration gap (Figure 5.1) may induce vacuum breakdown. These gaps are machined from Type 303 stainless steel and polished to near mirror-like finish using very fine sandpaper and emery cloth.

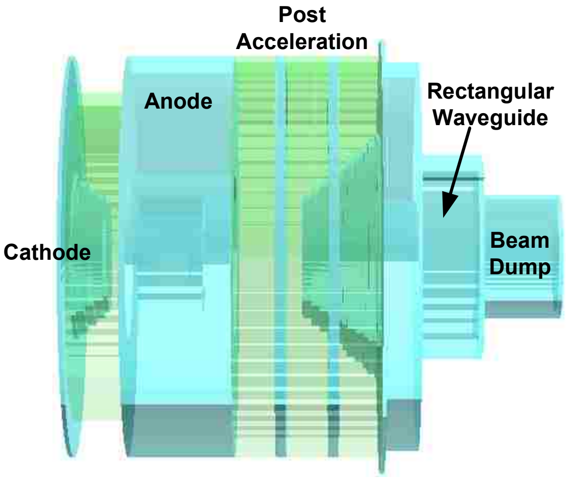

Figure 5.1: Schematic drawing of the UNM low power reltron.

We have to keep peak electric fields on the steel surface below 1.5x10^7 V/m (150 kV/cm) to minimize electron field emission which induces breakdown [15]. At the same time we have to maintain the electric field on the cathode surface above 3.0x10^6 V/m (30 kV/cm) so that explosive electron emission constantly generates electrons from the velvet cathode [28].

Obtaining the electric field distribution involves solving Laplace’s equation. On the surface of the cathode, we can calculate the field enhancement factor by modeling the anode and cathode as semi-infinite long coaxial rectangles. The peak electric field will occur on the rounded corner of the cathode and the field enhancement factor has been derived by Cockcroft [29]. Furthermore, we can account for the field enhancement due to the slope of the cathode/post acceleration cone by modeling the cathode/cone as a step with a rounded edge. Boag showed that the enhancement factor is a function of the edge curvature and base radius of the step [30]. It has a local maximum on the top of the rounded edge.

In their derivations, Cockcroft [29] and Boag [30] made geometric approximations to obtain closed form solutions. For complex geometries, we can use numerical methods to solve Laplace's equation. The Finite Difference method is a commonly used one. Another technique is the method of moments which has been proposed as a computationally more efficient method [31]. Numerical codes can now use the graphics processing units (GPUs) in parallel with the central processing units (CPUs) when performing matrix operations to reduce computation time.

In this Chapter, we propose an analytical model to calculate the electric field distribution for both the A-K and post-acceleration gaps. This model is able to account for the field distribution on the slope and on the surface of the gaps. This model has closed form solutions without having to perform integral transforms as done in the previous models. We shall compare our model with electrostatic simulations performed using CST Studio Suite.

5.2 ELECTRIC FIELDS DISTRIBUTION IN A-K GAP

The velvet cathode of the reltron is held in place by a stainless steel annulus. It lies under the modulating cavity with the cavity grids forming the anode, as indicated in Figure 5.2. The A-K gap distance is given by the distance between the top of the velvet cathode and the base of the modulating cavity.

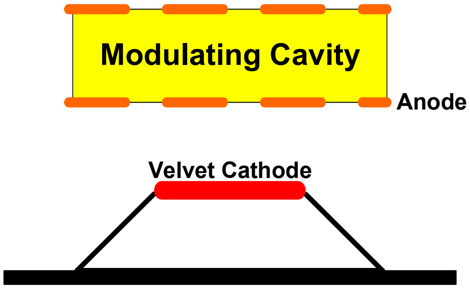

Figure 5.2: Schematic of the A-K gap in the reltron diode.

The base of the annulus is driven by a high voltage pulse generated by a Marx generator. This generates strong electric fields in the vertical direction that can result in breakdown occurring in the A-K gap.

We model the cathode as a flat conical conductor and the modulating cavity as an anode disc. A cylinder surrounds the A-K modules to make the analysis bounded. A mechanical drawing of the A-K gap is shown in Figure 5.3.

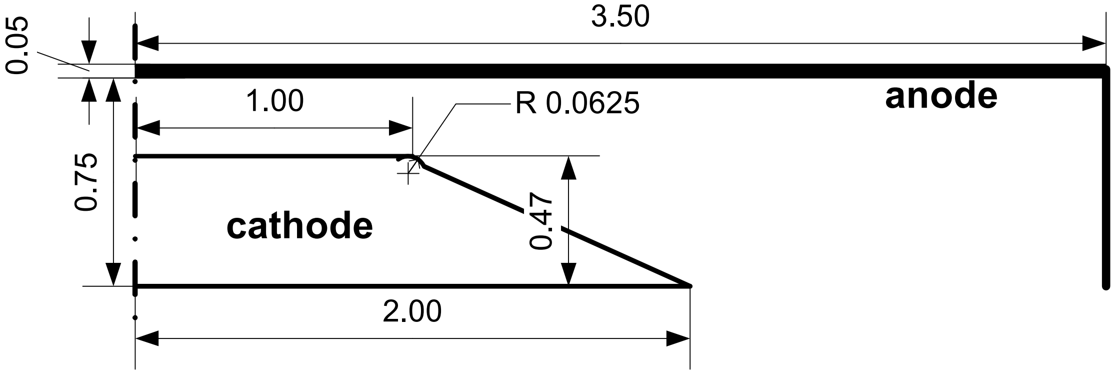

Figure 5.3: Dimensions of the A-K gap (in inch).

Both the cathode and anode are aligned along the center axis and are PEC. The space between the anode and cathode is vacuum.

5.2.1 Analytical Model of the Electric Field inside the A-K Gap

We shall divide the A-K gap space into region A and region B, as shown in Figure 5.4. All static fields are confined within the A-K gap space because the boundaries are perfect conductors.

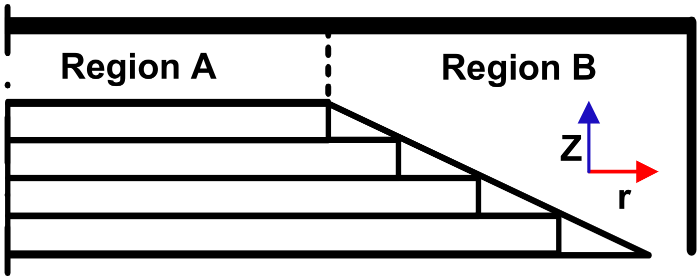

Figure 5.4: Model of the A-K gap as being divided into regions A and B.

Inside region B, we shall model the cathode as many thin discs whose radii correspond to the slope of the cathode, as indicated in Figure 5.5. This creates a multitude of steps that we use to calculate the E_z field above each step. By making the steps small, we obtain a good approximation for the E_z field above the slope in region B.

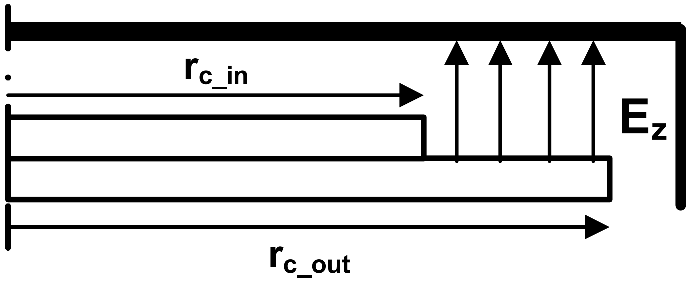

Figure 5.5: Drawing of the E_z fields in region B.

Inside region A, we model the cathode as a thin disc encased by the anode, as indicated in Figure 5.6. We calculate the E_z field above the cathode within the radius of the top disc.

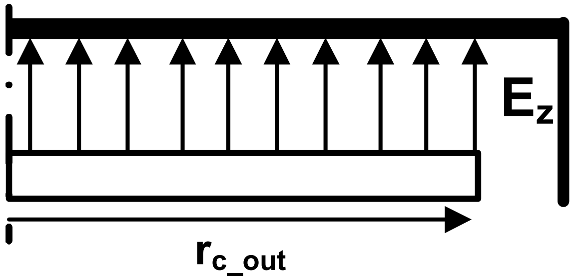

Figure 5.6: Drawing of the E_z fields in region A.

5.2.2 E_z Field inside the A-K Gap with Source Potential on the Cathode

We solve for the potential distribution inside the A-K gap with the cathode potential fixed at -80 kV, as illustrated in Figure 5.7.

The boundary conditions are

$\phi(r_c,\theta,h_c)=V_c$, $\phi(r_c,\theta,h_a)=0$ and $\phi(r_a,\theta,z)=0$ where $r_{c\_in}\le r_c\le r_{c\_out}$.

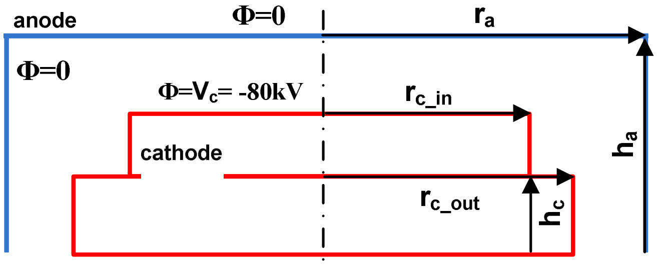

Figure 5.7: The A-K gap with the source potential on the cathode surface.

Starting with Laplace's equation in cylindrical coordinates

$$\nabla^2\varphi = 0,$$

$$\frac{1}{r}\frac{\partial}{\partial r}\left(r\frac{\partial\varphi}{\partial r}\right)+\frac{1}{r^2}\frac{\partial^2\varphi}{\partial\theta^2}+\frac{\partial^2\varphi}{\partial z^2}=0.$$

Using separation of variables $\phi(r,\theta,z)=R(r)\Theta(\theta)Z(z)$ we can simplify the above to yield

$$\Theta Z\frac{\partial^2 R}{\partial r^2}+\frac{\Theta Z}{r}\frac{\partial R}{\partial r}+\frac{1}{r^2}RZ\frac{\partial^2\Theta}{\partial\theta^2}+R\Theta\frac{\partial^2 Z}{\partial z^2}=0,$$

$$\frac{1}{R}\frac{\partial^2 R}{\partial r^2}+\frac{1}{R}\frac{1}{r}\frac{\partial R}{\partial r}+\frac{1}{\Theta}\frac{1}{r^2}\frac{\partial^2\Theta}{\partial\theta^2}+\frac{1}{Z}\frac{\partial^2 Z}{\partial z^2}=0.$$

If we assume the potential ϕ to be axisymmetric, this reduces to $\phi(r,z)=R(r)Z(z)$.

Since $\partial^2\phi/\partial\theta^2=0$, the $\partial^2\Theta/\partial\theta^2=0$ term goes away.

Laplace's equation becomes $\frac{1}{R}\frac{\partial^2 R}{\partial r^2}+\frac{1}{R}\frac{1}{r}\frac{\partial R}{\partial r}=-\frac{1}{Z}\frac{\partial^2 Z}{\partial z^2}$. Let $\frac{1}{Z}\frac{\partial^2 Z}{\partial z^2}=\lambda^2$. We proceed to solve for Z(z) through

$$\frac{\partial^2 Z}{\partial z^2}-Z\lambda^2=0,$$

$$Z(z)=A_3\sinh(\lambda(h_a-z))+B_3\cosh(\lambda(h_a-z)). \qquad (5.1)$$

For Z(h_a)=0, B_3=0 leaving $Z(z)=A_3\sinh(\lambda(h_a-z))$.

Solving for R(r), we obtain

$$\frac{1}{R}\frac{\partial^2 R}{\partial r^2}+\frac{1}{R}\frac{1}{r}\frac{\partial R}{\partial r}+\lambda^2=0,$$

$$\frac{\partial^2 R}{\partial r^2}+\frac{1}{r}\frac{\partial R}{\partial r}+\lambda^2 R=0, \text{ and}$$

$$R(r) = A_1 J_0(\lambda r) + B_1 Y_0(\lambda r)\,. \tag{5.2}$$

For $R(r_a)=0$, the values of λ are restricted to $\lambda_n = \chi_n / r_a$ where χ_n are the n$^{\text{th}}$ zeros of the Bessel function J_0. Since $Y_0(\lambda_n r_a) \neq 0$, we set $B_1=0$.

The potential is given by

$$\varphi(r,z) = \sum_{n=1}^{\infty} A_n J_0(\lambda_n r) \sinh\left(\lambda_n (h_a - z)\right). \tag{5.3}$$

To obtain the coefficients A_n, we substitute $\phi(r_c, \theta, h_C) = V_c$, where

$$V_c = \sum_{n=1}^{\infty} A_n J_0(\lambda_n r_c) \sinh\left(\lambda_n (h_a - h_c)\right) \text{ and } r_{c\_in} \le r_c \le r_{c\_out}\,.$$

Multiplying both sides of this equation with $r_c J_0(\lambda_{n'} r_c)$ and integrating over the radius,

$$\int_{r_{c\_in}}^{r_{c\_out}} V_c r_c J_0(\lambda_{n'} r_c)\, dr_c = \int_{r_{c\_in}}^{r_{c\_out}} \sum_{n=1}^{\infty} A_n J_0(\lambda_n r_c) \sinh\left(\lambda_n (h_a - h_c)\right) r_c J_0(\lambda_{n'} r_c)\, dr_c,$$

$$\frac{V_c}{\lambda_n^2} \int_{\lambda_n r_{c\_in}}^{\lambda_n r_{c\_out}} r_c' J_0(r_c')\, dr_c' = \frac{A_n \sinh\left(\lambda_n (h_a - h_c)\right)}{2}$$

$$\times \left\{ r_{c\_out}^2 \left[J_1(\lambda_n r_{c\_out})^2 + J_0(\lambda_n r_{c\_out})^2 \right] - r_{c\_in}^2 \left[J_1(\lambda_n r_{c\_in})^2 + J_0(\lambda_n r_{c\_in})^2 \right] \right\},$$

$$\frac{V_c}{\lambda_n^{\ 2}} \left[\lambda_n r_{c\_out} J_1(\lambda_m r_{c\_out}) - \lambda_n r_{c\_in} J_1(\lambda_m r_{c\_in}) \right] = \frac{A_n \sinh\left(\lambda_n (h_a - h_c)\right)}{2} f(r_{c\_out}, r_{c\_in})\text{, with}$$

$$A_n = \frac{2V_c}{\lambda_n \sinh\left(\lambda_n (h_a - h_c)\right)} \frac{g(r_{c\_out}, r_{c\_in})}{f(r_{c\_out}, r_{c\_in})},$$

where

$$f(r_{c\_out}, r_{c\_in}, \lambda_n) = r_{c\_out}^2 \left[J_1(\lambda_n r_{c\_out})^2 + J_0(\lambda_n r_{c\_out})^2 \right] - r_{c\_in}^2 \left[J_1(\lambda_n r_{c\_in})^2 + J_0(\lambda_n r_{c\_in})^2 \right]$$

$$g(r_{c\_out}, r_{c\_in}, \lambda_n) = r_{c\_out} J_1(\lambda_n r_{c\_out}) - r_{c\_in} J_1(\lambda_n r_{c\_in})\,.$$

Finally,

$$\phi(r,z) = \sum_{n=1}^{\infty} A_n J_0(\lambda_n r) \sinh\left(\lambda_n (h_a - z)\right). \tag{5.4}$$

The E_z field in region B above the slope of the annulus is given by

$$E_{z\_regB}(r,z) = -d\phi(r,z)/dz$$

$$= 2V_c \sum_{n=1}^{\infty} \frac{g(r_{c\_out}, r_{c\_in}, \lambda_n)}{f(r_{c\_out}, r_{c\_in}, \lambda_n)} \frac{J_0(\lambda_n r)\cosh(\lambda_n (h_a - z))}{\sinh(\lambda_n (h_a - h_c))}. \tag{5.5}$$

By taking the limits $r_{c\_in} \to 0$, we can change the E_{z_regB} field solution from that for an annulus to that of a disc

$$\lim_{r_{c\_in}\to 0} f(r_{c\_out}, r_{c\_in}, \lambda_n) = r_{c\_out}^2 \left[J_1(\lambda_n r_{c\_out})^2 + J_0(\lambda_n r_{c\_out})^2\right] \text{ and}$$

$$\lim_{r_{c\_in}\to 0} g(r_{c\_out}, r_{c\_in}, \lambda_n) = r_{c\_out} J_1(\lambda_n r_{c\_out}) .$$

The E_z field in region A above the cathode surface is

$$E_{z\_regA}(r,z) = \lim_{r_{c\_in}\to 0} 2V_c \sum_{n=1}^{\infty} \frac{g(r_{c\_out}, r_{c\_in}, \lambda_n)}{f(r_{c\_out}, r_{c\_in}, \lambda_n)} \frac{J_0(\lambda_n r)\cosh(\lambda_n (h_a - z))}{\sinh(\lambda_n (h_a - h_c))}$$

$$= 2V_c \sum_{n=1}^{\infty} \frac{J_1(\lambda_n r_{c\_out})}{r_{c\_out}\left[J_1(\lambda_n r_{c\_out})^2 + J_0(\lambda_n r_{c\_out})^2\right]} \frac{J_0(\lambda_n r)\cosh(\lambda_n (h_a - z))}{\sinh(\lambda_n (h_a - h_c))}. \tag{5.6}$$

To check our solution, we take the limits $r_a \to r_{c\_out} = r_c$ and $h_a \to 0$. The result is the standard formula for the E_z field inside a cylinder,

$$E_z(r,z) = \lim_{r_{c\_in}\to r_c} 2V_c \sum_{n=1}^{\infty} \frac{J_1(\lambda_n r_{c\_out})}{r_{c\_out}\left[J_1(\lambda_n r_{c\_out})^2 + J_0(\lambda_n r_{c\_out})^2\right]} \frac{J_0(\lambda_n r)\cosh(\lambda_n (h_a - z))}{\sinh(\lambda_n h_a)}$$

$$= \frac{2V_c}{r_c} \sum_{n=1}^{\infty} \frac{J_0(\lambda_n r)\cosh(\lambda_n (h_a - z))}{\sinh(\lambda_n h_a) J_1(\lambda_n r_c)}. \tag{5.7}$$

We calculate the field solution E_{z_regA} and E_{z_regB} using Mathcad v14. For region A, we use a cell size of dr=dz=0.001inch and for region B, we use a cell size of dr=0.0001 inch and dz=0.001 inch. Figure 5.8 shows a contour plot for the E_z field distribution in region A.

Figure 5.9 shows a contour plot for the E_z field distribution in region B. The spikes in the E_z fields are due to the stair stepping effects on the slope of the cathode discussed earlier.

5.2.3 Electrostatic Simulation of the A-K Gap

We simulate the electric field distribution in the A-K gap using the electrostatic solver in CST EM Studios v2010 (CST) Figure 5.10.

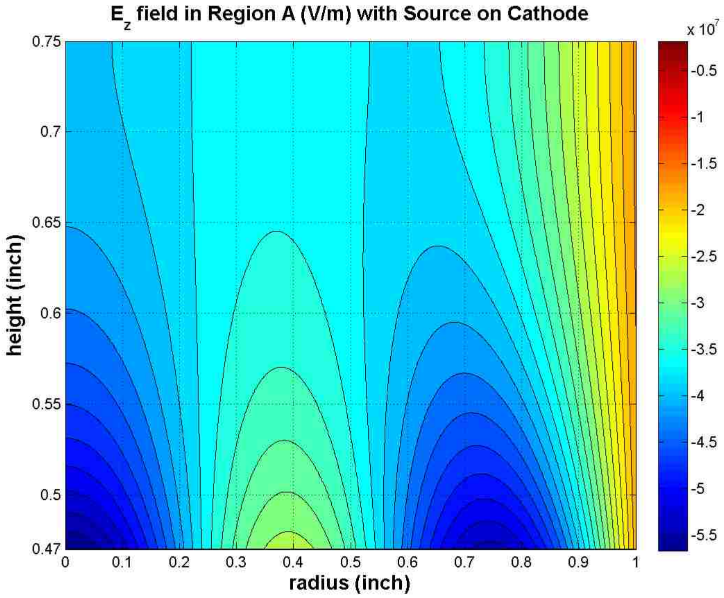

Figure 5.8: Contour plot of the E_z field distribution in region A with the source potential on the cathode.

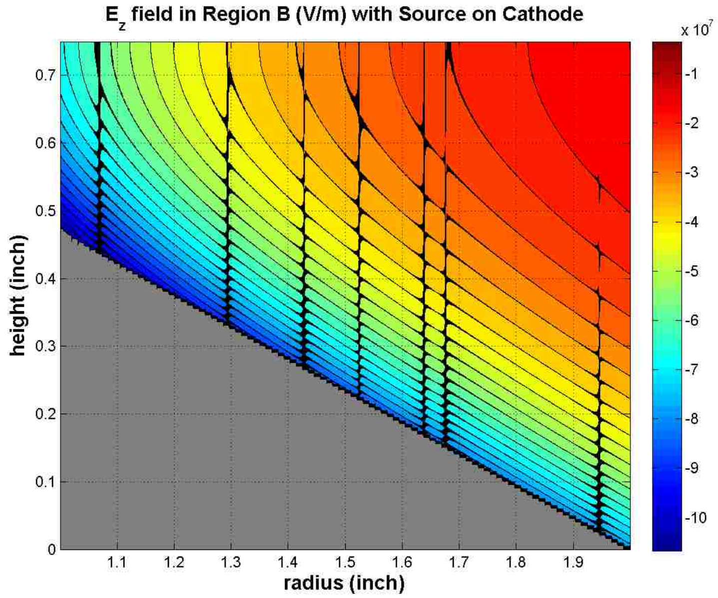

Figure 5.9: Contour plot of the E_z field distribution in region B with the source potential on the cathode.

CST uses a minimum mesh size of 0.00551471 inch and a maximum of 0.0927402 inch. This is larger than the maximum grid size of 0.001 used for numerical calculation of the analytical solutions. However, CST is able to obtain better field resolution by using automatic hexahedral meshing with adaptive mesh refinement. The meshing algorithm uses the Perfect Boundary Approximation (PBA) so the hexahedral grid does not have to conform to the rounded corners. This process does increase preprocessing complexity but the increase in computational time during numerical iteration is nominal. As meshing becomes easier, we reduce the overall computational time when we utilize iterative mesh refinement. This allows us to see the effect of field enhancement on the rounded corners of the cathode that is not accounted for in the analytical model.

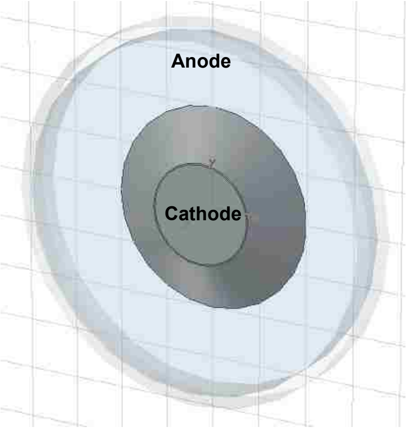

Figure 5.10: Model of the A-K gap in the CST simulation environment.

We use a fixed source potential of 80 kV on the anode so that we can see the field distribution on the cathode surface. We use open boundary conditions so the anode and cathode exist in free space. We assume the anode and cathode material to be perfect electrical conductors (PEC) so no fields can exist inside the anode or cathode.

Figure 5.11 presents a plot of the E_z field distribution on the cathode. The E_z field inside the vacuum region has a maximum field of -9.18×10^7 V/m at the rounded edge on the top of the cathode, as indicated in Figure 5.12.

As we wish to keep the peak electric field below -1.5×10^7 V/m, we increase the height of the anode to $h_a = 1.0$ inch. The entire cathode surface is now below -1.0×10^7 V/m, as indicated in Figure 5.13.

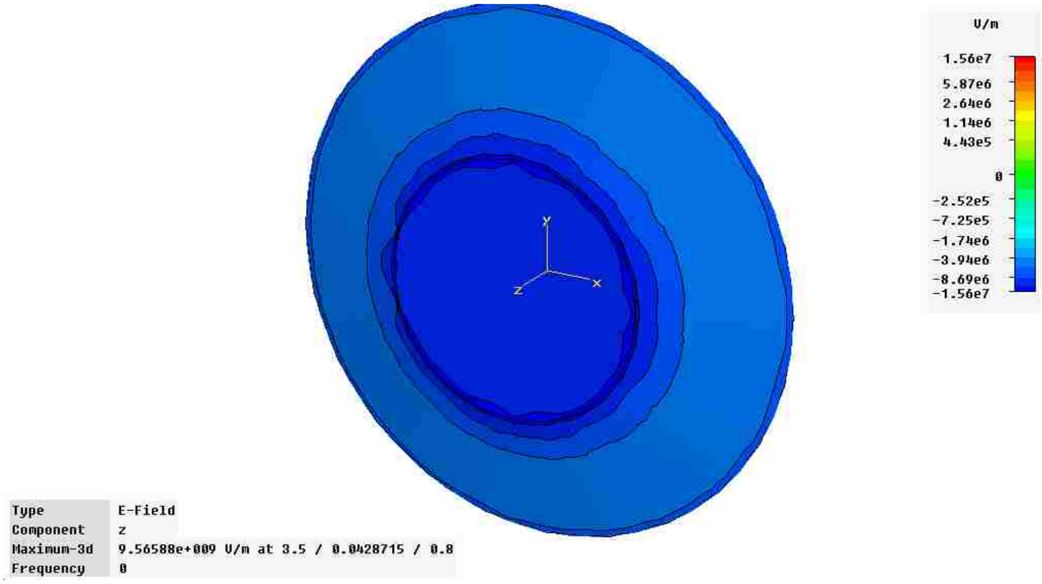

Figure 5.11: Plot of the E_z field distribution on the cathode for h_a = 0.75 inch.

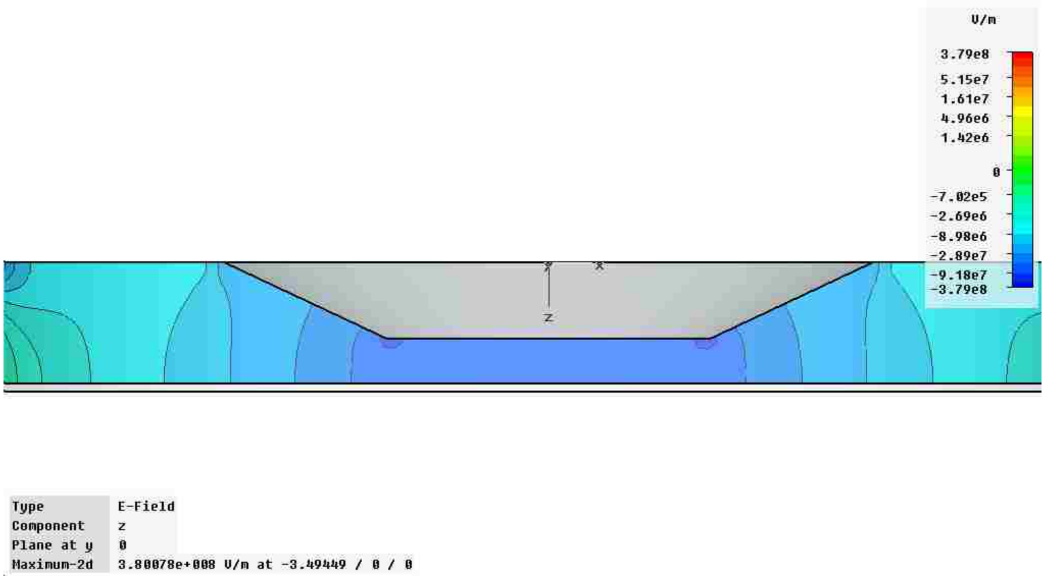

Figure 5.12: Plot of the E_z field distribution inside the A-K gap for h_a = 0.75 inch.

Inside the vacuum there are still regions above -1.5 x 10^7 V/m. The regions closest to the anode have a peak field of -5.76 x 10^7 V/m, as indicated in Figure 5.14. We can lower the peak E_z field by increasing the anode to h_a = 1.25 inch. The peak E_z field on the cathode surface is then reduced to -6.54 x 10^6 V/m, as indicated in Figure 5.15.

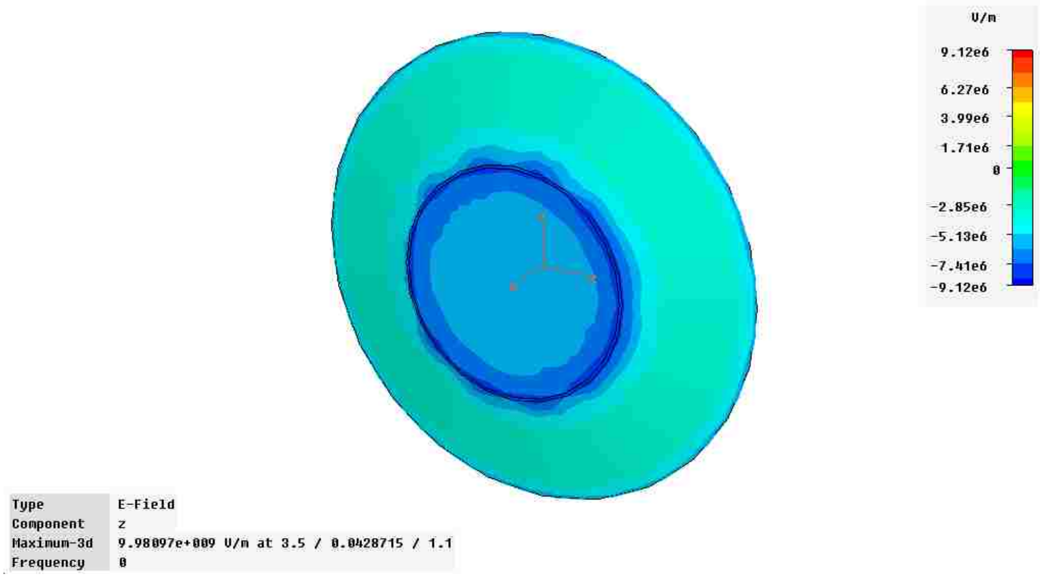

Type E-Field
Component z
Maximum-3d 9.98097e+009 V/m at 3.5 / 0.0428715 / 1.1
Frequency 0

Figure 5.13: Plot of the E_z field distribution on the cathode for h_a = 1.0 inch.

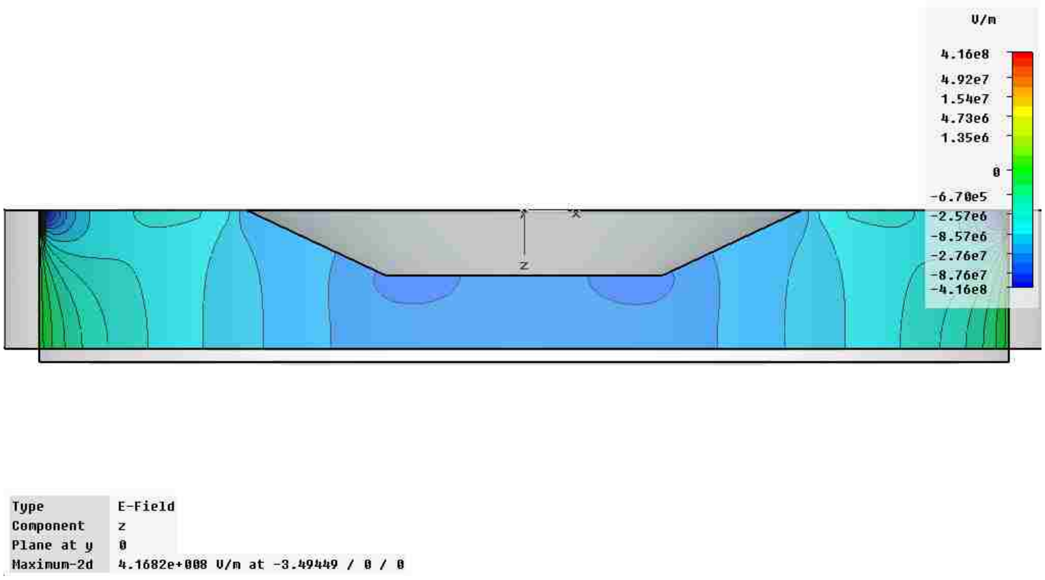

Type E-Field
Component z
Plane at y 0
Maximum-2d 4.1682e+008 V/m at -3.49449 / 0 / 0

Figure 5.14: Plot of the E_z field distribution inside the A-K gap for h_a = 1.0 inch.

In the vacuum region above the flat cathode surface the Ez field is now -1.51 x 10^7 V/m, as indicated in Figure 5.16. We further reduce E_z by increasing the base radius from 2.0 to 2.5 inch. The maximum E_z field on the cathode surface subsequently decreases from -6.54 x 10^6 V/m to -5.66 x 10^6 V/m.

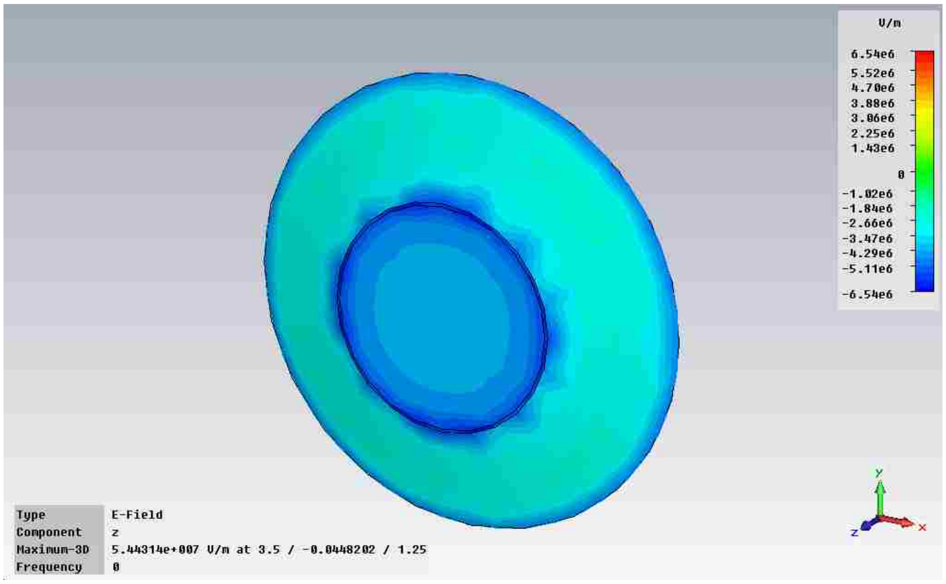

Type E-Field
Component z
Maximum-3D 5.44314e+007 V/m at 3.5 / -0.0448202 / 1.25
Frequency 0

Figure 5.15: Plot of the E_z field distribution on the cathode for h_a = 1.25 inch.

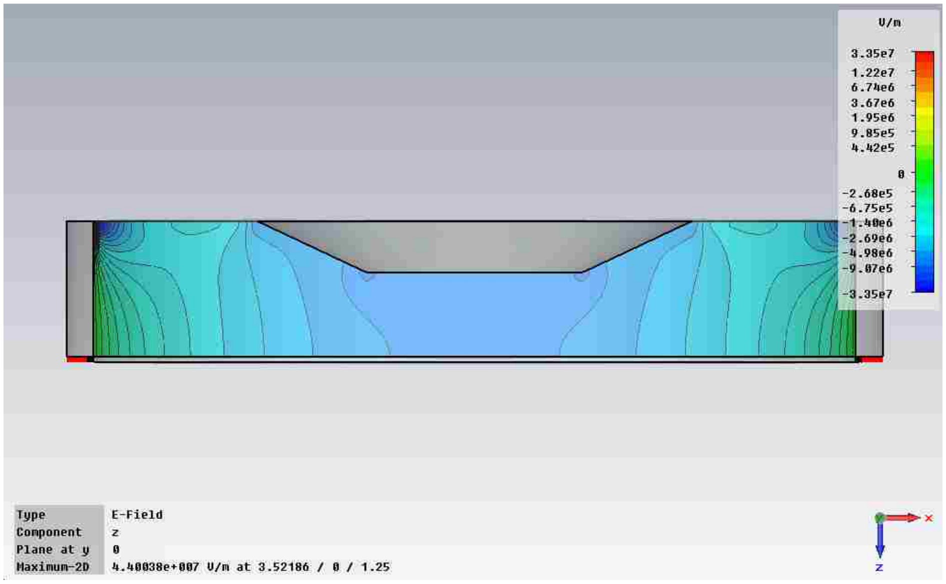

Type E-Field
Component z
Plane at y 0
Maximum-2D 4.40038e+007 V/m at 3.52186 / 0 / 1.25

Figure 5.16: Plot of the E_z field distribution inside the A-K gap for h_a = 1.25 inch.

5.3 ELECTRIC FIELD DISTRIBUTION IN THE POST-ACCELERATION GAP

We now investigate the E_z field distribution in the post-acceleration gap. The gap lies between the modulating cavity and the extraction waveguide, as shown in Figure 5.17. A hollow cone is used to shape the electric field in the gap, thereby reducing electric field enhancement. The cone is covered by a micron-thin grid with transparency

80% - 90%. The cone is joined to a rectangular waveguide that has a hole in its base aligned with the axis of the cone.

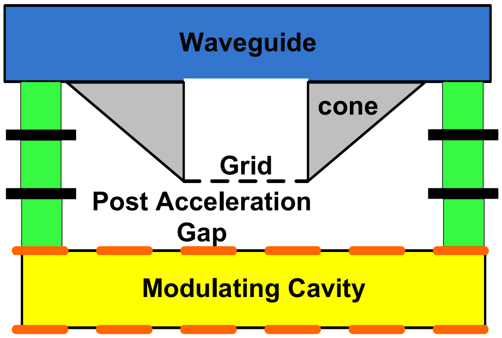

Figure 5.17: Schematic of the post-acceleration gap.

The post-acceleration gap is insulated by three dielectric insulator rings with two metal rings in between. The modulating cavity is driven by a post-accelerating voltage. We model the gap region with a cathode cone and an anode disc representing the modulating cavity. A cylinder surrounds the A-K modules to make the analysis space bounded. The mechanical drawing of the A-K gap is shown in Figure 5.18. This analysis will exclude the waveguide so that the cone sits on a grounded disc with a radius smaller than the anode radius. The normal electrostatic fields pass through the grids because of the high transparency so we can neglect the presence of the grid in our analysis. All the metal modules are assumed to be perfect conductors and the dielectric rings are assumed to be lossless.

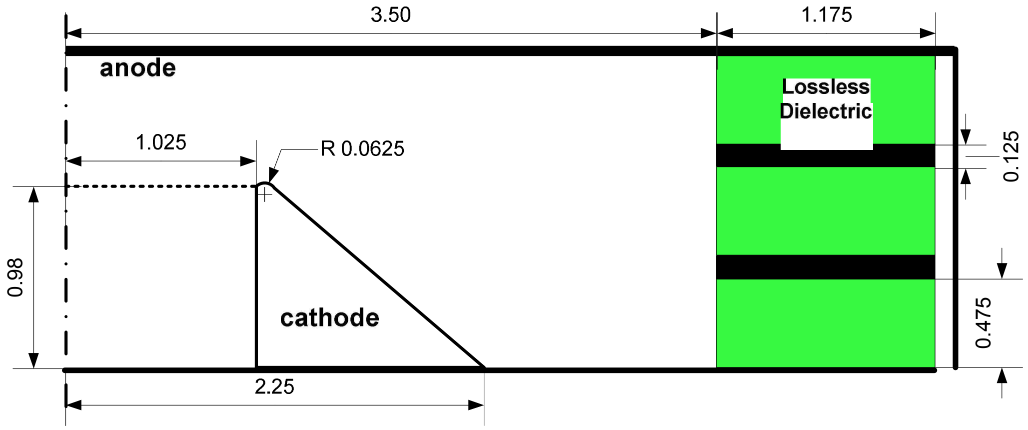

Figure 5.18: Dimensions of the post-acceleration gap (dimensions are in inch).

5.3.1 Analytical Model of the Electric field in the Post Acceleration Gap

Our analytical model will only include the cathode cone and the anode, as illustrated in Figure 5.19. We separate the gap into two regions, region A and region B. Region A will encompass the space above (region A1) and inside (region A2) the cone. Region B will encompass the space above the slope of the cone. Just as before, we divide the cone into many annular discs with outer radius conforming to the slope of the cone.

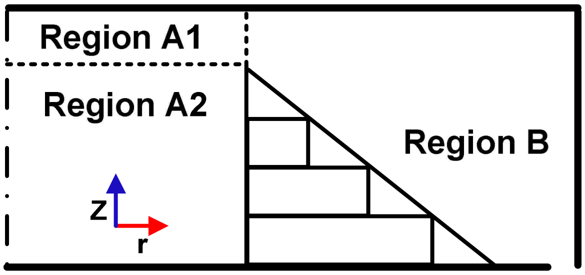

Figure 5.19: Model of the post-acceleration gap.

5.3.2 E_z field inside Region B with Source Potential at the Top of the Anode

We solve for the potential distribution inside the post-acceleration gap with the top of the anode fixed at -40 kV, as indicated in Figure 5.20.

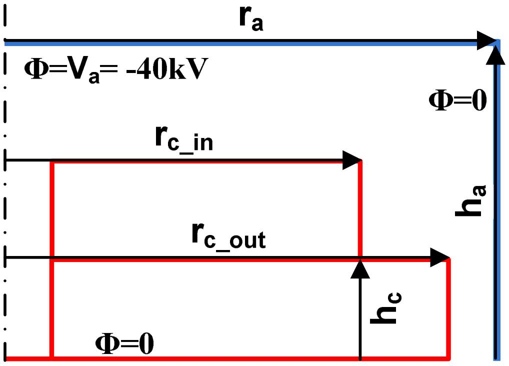

Figure 5.20: Model of the post-acceleration gap with the source potential on top of the anode.

The boundary conditions are

$\phi(r_c,\theta,h_c)=0$, $\phi(r_c,\theta,h_a)=V_a$ and $\phi(r_a,\theta,z)=0$. Where $r_{c\_in} \le r_c \le r_{c\_out}$

From the boundary conditions, we see that moving the source from the bottom to the top only affects the Z(z) component in Laplace's equation. We can recast the A-K gap solution to match the above boundary conditions by changing $Z(z) = A_3 \sinh\left(\lambda(h_a - z)\right)$ to $Z(z) = A_3 \sinh\left(\lambda(z - h_c)\right)$.

The E_z field in region B above the slope of the annulus is given by

$$E_{z\_regB}(r,z) = -2V_a \sum_{n=1}^{\infty} \frac{g(r_{c\_out}, r_{c\_in}, \lambda_n)}{f(r_{c\_out}, r_{c\_in}, \lambda_n)} \frac{J_0(\lambda_n r)\cosh\left(\lambda_n (z - h_c)\right)}{\sinh\left(\lambda_n (h_a - h_c)\right)}. \tag{5.8}$$

The E_z field in region A1, above the cone, is given by

$$E_{z\_regA1}(r,z) = -2V_a \sum_{n=1}^{\infty} \frac{J_1(\lambda_n r_{c\_out})}{r_{c\_out}\left[J_1(\lambda_n r_{c\_out})^2 + J_0(\lambda_n r_{c\_out})^2\right]} \frac{J_0(\lambda_n r)\cosh\left(\lambda_n (z - h_c)\right)}{\sinh\left(\lambda_n (h_a - h_c)\right)}. \tag{5.9}$$

We obtain the E_z field in region A2, inside the cone, by taking the limits $h_c \to 0$,

$$E_{z\_regA2}(r,z) = -2V_a \sum_{n=1}^{\infty} \frac{J_1(\lambda_n r_{c\_out})}{r_{c\_out}\left[J_1(\lambda_n r_{c\_out})^2 + J_0(\lambda_n r_{c\_out})^2\right]} \frac{J_0(\lambda_n r)\cosh\left(\lambda_n z\right)}{\sinh\left(\lambda_n h_a\right)}, \tag{5.10}$$

where $\lambda_n = \chi_n / r_a$ when z > height of hollow cone and $\lambda_n = \chi_n / r_c$ when z ≤ height of hollow cone.

Using $E_{z\text{ regA1}}$ and $E_{z\text{ regA2}}$ we generate a contour plot of the E_z field distribution in region A, shown in Figure 5.21. The E_z field is slightly discontinuous on the grid because we use a discretized λ_n to model the boundary condition.

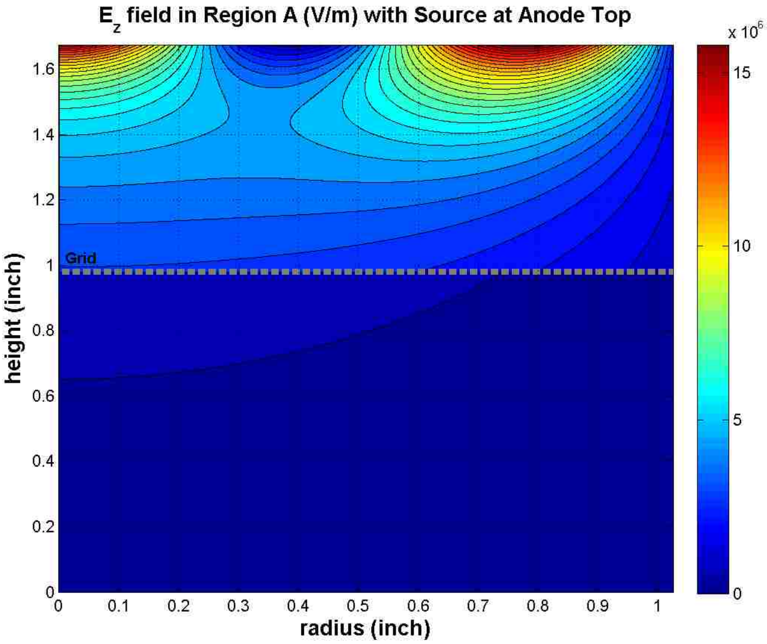

Figure 5.21: Contour plot of the E_z field distribution in region A with the source potential on top of the anode.

Using $E_{z\ regB}$ we generate a contour plot of the E_z field distribution in region B, shown in Figure 5.22.

The spikes in the E_z field distribution are due to the stair stepping approximation of the slope of the cathode. The spikes get smoother as we move away from the cathode to the anode, as shown in Figure 5.23.

5.3.3 E_z field inside Region B with Source Potential at the Side of the Anode

We solve for the potential distribution inside the post-acceleration gap with the side of the anode fixed at -40 kV (Figure 5.24).

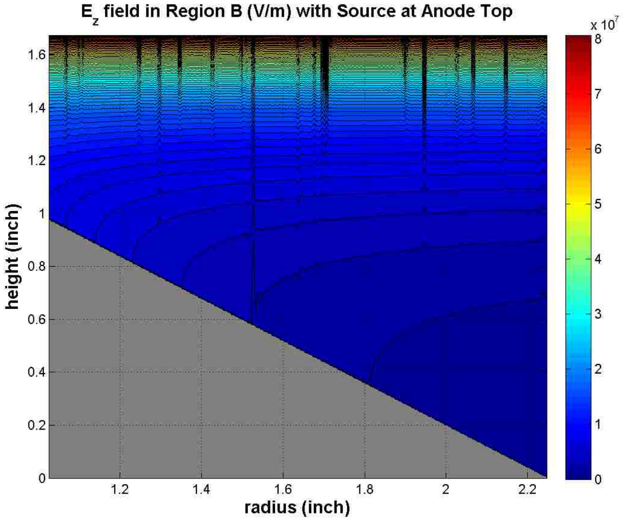

Figure 5.22: Contour plot of the E_z field distribution in region B with the source potential on top of the anode.

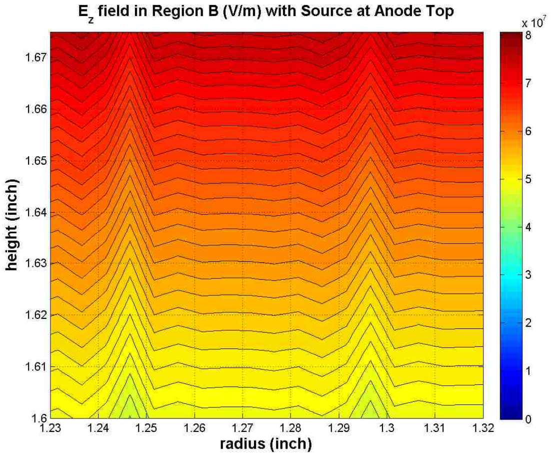

Figure 5.23: Contour plot of the E_z field distribution in region B near the top of the anode.

The boundary conditions are

$\phi(r_c,\theta,h_c)=0$, $\phi(r_c,\theta,h_a)=0$ and $\phi(r_a,\theta,z)=V_a$ where $r_{c\_in} \le r_c \le r_{c\_out}$.

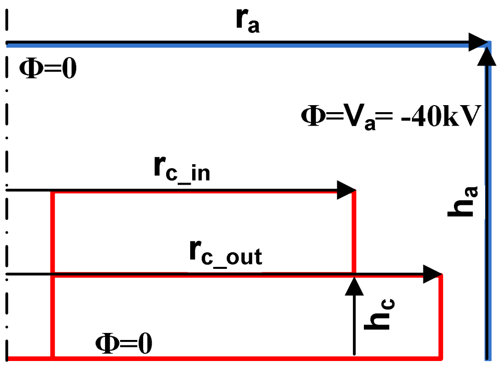

Figure 5.24: Model of the post-acceleration gap with the source potential at the side of the anode.

We first derive the Ez field for a full cone (without the center hole). By separation of variables, Laplace's equation becomes $\frac{1}{R}\frac{\partial^2 R}{\partial r^2}+\frac{1}{R}\frac{1}{r}\frac{\partial R}{\partial r}=-\frac{1}{Z}\frac{\partial^2 Z}{\partial z^2}$. We proceed to solve for Z(z)

$$\frac{1}{Z}\frac{\partial^2 Z}{\partial z^2}=-p^2,$$

$$\frac{\partial^2 Z}{\partial z^2}+Zp^2=0,$$

$$Z(z)=A_3\sin\left(p(z-h_c)\right)+B_3\cos\left(p(z-h_c)\right). \tag{5.11}$$

For $\phi(r_c,\theta,h_c)=0$ and $\phi(r_c,\theta,h_a)=0$ we get $Z(z)=A_3\sin\left(p_m(z-h_c)\right)$, where $p_m=m\pi/(h_a-h_c)$ for m=0,1,2… Solving for R(r), we obtain

$$\frac{1}{R}\frac{\partial^2 R}{\partial r^2}+\frac{1}{R}\frac{1}{r}\frac{\partial R}{\partial r}-p_m^2=0,$$

$$\frac{\partial^2 R}{\partial r^2}+\frac{1}{r}\frac{\partial R}{\partial r}-p_m^2 R=0,$$

$$R(r)=A_1 I_0(p_m r)+B_1 K_0(p_m r). \tag{5.12}$$

For R(r_{c_in}) =0,

$0=A_1 I_0(p_m r_c)+B_1 K_0(p_m r_{c\_in})$, where

$$B_1=\frac{-A_1 I_0(p_m r_{c\_in})}{K_0(p_m r_{c\_in})}.$$

The potential is now given by

$$\phi(r,z)=\sum_{m=0}^{\infty}A_m\left[I_0(p_m r)-\frac{I_0(p_m r_c)}{K_0(p_m r_c)}K_0(p_m r)\right]\sin\left(p_m(z-h_c)\right). \tag{5.13}$$

We substitute $\phi(r_a,\theta,z)=V_a$

$V_a=\sum_{m=0}^{\infty}A_m\left[I_0(p_m r_a)-\frac{I_0(p_m r_c)}{K_0(p_m r_c)}K_0(p_m r_a)\right]\sin\left(p_m(z-h_c)\right)$. Multiply both sides by $\sin\left(p_{m'}(z-h_c)\right)$ and integrate over radius to obtain

$$\int_{h_c}^{h} V_a\sin\left(p_{m'}(z-h_c)\right)dz=\int_{h_c}^{h}\sum_{m=0}^{\infty}A_m\left[I_0(p_m r_a)-\frac{I_0(p_m r_c)}{K_0(p_m r_c)}K_0(p_m r_a)\right]\sin\left(p_m(z-h_c)\right)\sin\left(p_{m'}(z-h_c)\right)dz,$$

$$\frac{-V_a}{p_m}\left[\cos p_m(z-h_c)\right]_{h_c}^{h_a}=\sum_{m=0}^{\infty}\int_{h_a}^{h}A_m\left[I_0(p_m r_a)-\frac{I_0(p_m r_c)}{K_0(p_m r_c)}K_0(p_m r_a)\right]\sin\left(p_m(z-h_c)\right)\sin\left(p_{m'}(z-h_c)\right)dz, \text{ and}$$

$$\frac{-V_a}{p_m}\left[\cos(m\pi)-1\right]=A_m\left[I_0(p_m r_a)-\frac{I_0(p_m r_c)}{K_0(p_m r_c)}K_0(p_m r_a)\right]\frac{h_a-h_c}{2}, \text{ where}$$

$$A_m=\frac{-2V_a}{m\pi\left[I_0(p_m r_a)-\frac{I_0(p_m r_c)}{K_0(p_m r_c)}K_0(p_m r_a)\right]}\left[\cos(m\pi)-1\right]$$

$$=\frac{2V_a\left((-1)^{m+1}+1\right)}{m\pi\left[I_0(p_m r_a)-\frac{I_0(p_m r_c)}{K_0(p_m r_c)}K_0(p_m r_a)\right]}.$$

Now $m\neq 0$, so m=1,2…, so that

$$\phi(r,z)=2V_a\sum_{m=1}^{\infty}\frac{\left((-1)^{m+1}+1\right)\left[I_0(p_m r)-\frac{I_0(p_m r_c)}{K_0(p_m r_c)}K_0(p_m r)\right]}{m\pi\left[I_0(p_m r_a)-\frac{I_0(p_m r_c)}{K_0(p_m r_c)}K_0(p_m r_a)\right]}\sin\left(p_m(z-h_c)\right)$$

$$=2V_a\sum_{m=1}^{\infty}\frac{\left((-1)^{m+1}+1\right)\left[I_0(p_m r)K_0(p_m r_c)-I_0(p_m r_{c\_in})K_0(p_m r)\right]}{m\pi\left[I_0(p_m r_a)K_0(p_m r_c)-I_0(p_m r_{c\_in})K_0(p_m r_a)\right]}\sin\left(p_m(z-h_c)\right). \tag{5.14}$$

The E_z field in region B above the slope of the annulus is given by

$$E_{z\_regB}(r,z)=-d\phi(r,z)/dz$$

$$=\frac{-2V_a}{h_a-h_c}\sum_{m=1}^{\infty}\left((-1)^{m+1}+1\right)\frac{a(r,r_c,p_m)}{b(r_a,r_c,p_m)}\cos\left(p_m(z-h_c)\right), \tag{5.15}$$

where

$a(r, r_{c\_in}, p_m) = I_0(p_m r)K_0(p_m r_c) - I_0(p_m r_c)K_0(p_m r)$ and

$b(r_a, r_{c\_in}, p_m) = I_0(p_m r_a)K_0(p_m r_c) - I_0(p_m r_c)K_0(p_m r_a)$.

Taking the limit $r_c \to 0$, $\lim\limits_{r_{c\_in} \to 0} \dfrac{a(r_a, r_{c\_in}, p_m)}{b(r_a, r_{c\_in}, p_m)} \to \dfrac{I_0(p_m r)}{I_0(p_m r_a)}$.

The E$_z$ field in region A1, above the cone, is given by

$$E_{z\_regA1}(r,z) = \frac{-2V_a}{h_a - h_c} \sum_{m=1}^{\infty} \left((-1)^{m+1} + 1 \right) \frac{I_0(p_m r)}{I_0(p_m r_a)} \cos\left(p_m (z - h_c) \right). \tag{5.16}$$

We obtain the E$_z$ field in region A2, inside the cone, by taking the limits $h_c \to 0$,

$$E_{z\_regA2}(r,z) = \frac{-2V_a}{h_a} \sum_{m=1}^{\infty} \left((-1)^{m+1} + 1 \right) \frac{I_0(p_m r)}{I_0(p_m r_a)} \cos\left(p_m z \right), \tag{5.17}$$

where $p_m = m\pi / h_a$.

Using E$_{z\ \mathrm{regA1}}$ and E$_{z\ \mathrm{regA2}}$ we generate a contour plot of the E$_z$ field distribution in region A, which is shown in Figure 5.25. The surface of the cathode is perpendicular to the anode side so the charge induced on the cathode surface will be small. As a result the E$_z$ field induced will have a small magnitude.

Using E$_{z\ \mathrm{regB}}$ we generate a contour plot of the E$_z$ field distribution in region B, which is shown in Figure 5.26. The E$_z$ field on the slope of the cathode will be much larger since the slope is at an angle to the anode side. However, the E$_z$ field is still many orders of magnitude smaller compared to the case where the source potential is on the cathode or on the anode top.

5.3.4 Electrostatic Simulation of the Post-Acceleration Gap

In order to account for the effects of the insulator and metal ring in the electric field distribution, we turn to electrostatic simulations. We simulate the post-acceleration gap using CST, as shown in Figure 5.27.

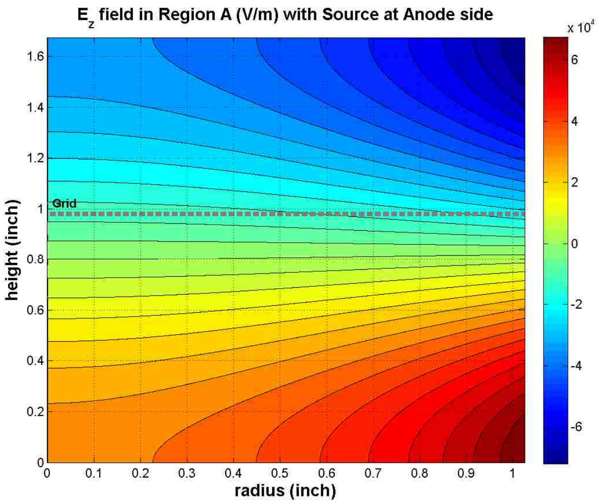

Figure 5.25: Contour plot of the E_z field distribution in region A with the source potential on the side of the anode.

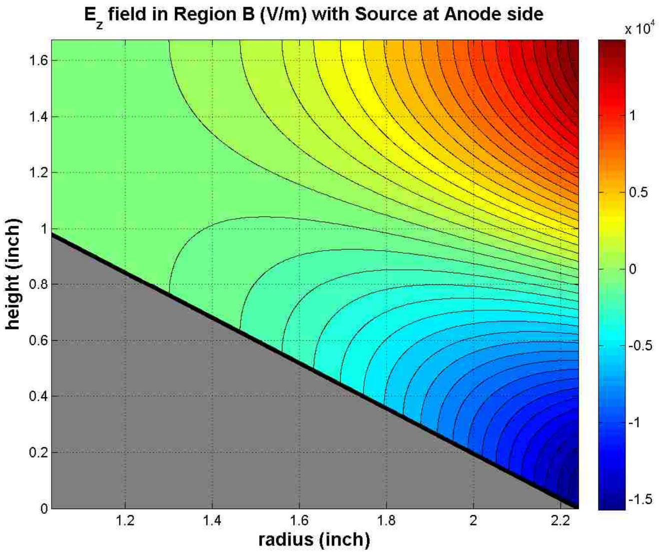

Figure 5.26: Contour plot of the E_z field distribution in region B with the source potential on the side of the anode.

We again use the iterative electrostatic field solver with adaptive meshing. We set the relative permittivity of the lossless dielectric to be 3.2. The z axis is opposite in direction compared to the analytical solution resulting in the E_z fields having negative polarity in the simulations. CST uses a minimum mesh size of 0.0119 inch and a maximum of 0.111 inch. This is larger than the grid size of dz=0.001, dr=0.0002 used in evaluating the analytical solutions. We observe that field enhancement is largest on the rounded edge at the top of the cone with the minimum E_z field -3.41×10^6 V/m, as shown in Figure 5.28.

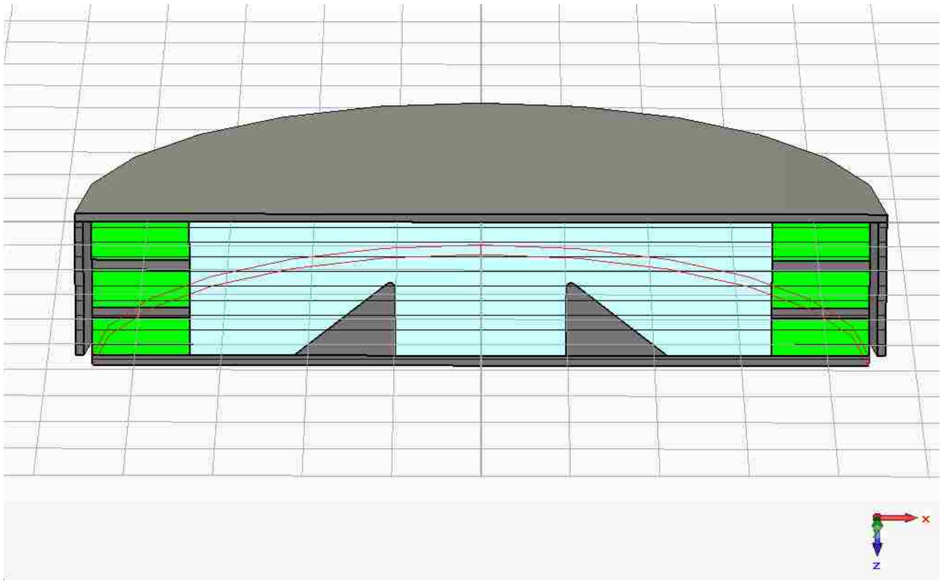

Figure 5.27: Model of the post acceleration gap in CST.

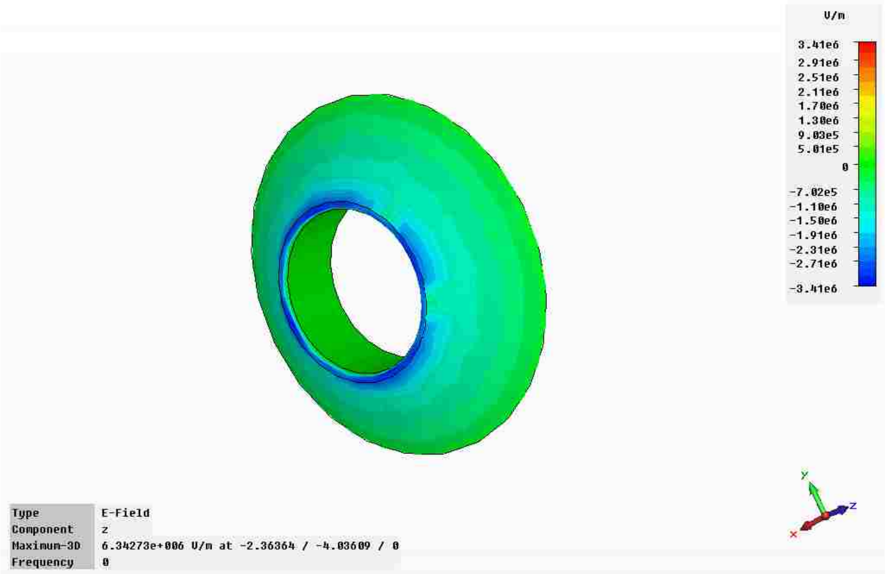

Type	E-Field
Component	z
Maximum-3D	6.34273e+006 V/m at -2.36364 / -4.03609 / 0
Frequency	0

Figure 5.28: E_z field distribution on the cathode cone.

The joining of the insulator, metal ring, and vacuum is termed the triple point. The triple point is the point where electron emission is most likely to occur. This is because of the increased field enhancement at the triple point due to the relative permittivity of the insulator. Field enhancement can be seen from the continuity of the electric field, between the vacuum and dielectric region, normal to the surface of the insulator

$$E_{x\_vacc} = \varepsilon_{x\_dielectric} E_{x\_dielectric} \,. \tag{5.18}$$

We see that the electric field in the vacuum is enhanced by the relativity permittivity of the dielectric ε_r. The distribution of the normal electric field in the vicinity of the triple point is obtained from the CST simulations and shown in Figure 5.29. The electric fields at the vacuum and dielectric interface are stronger than the electric fields inside the dielectric.

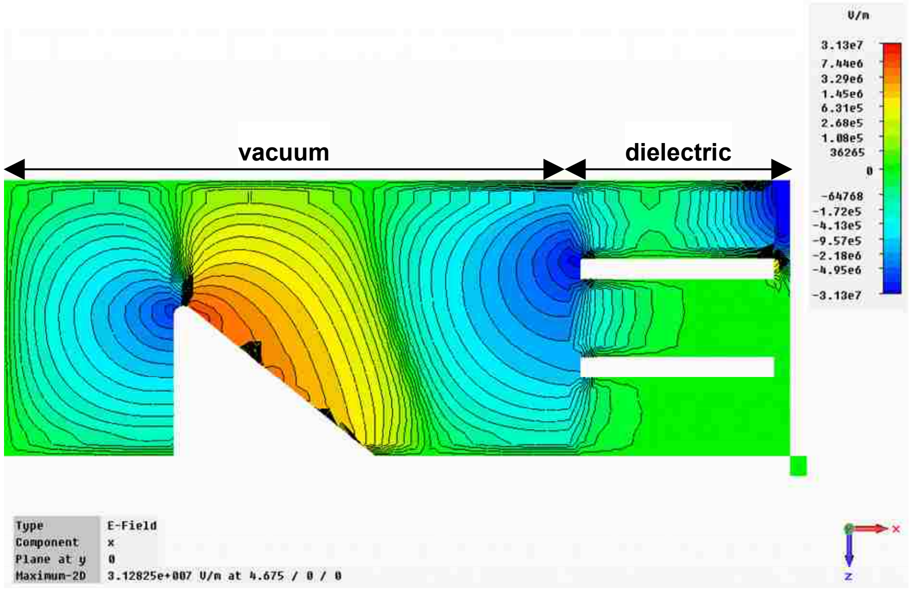

Figure 5.29: E_x field distribution inside the post-acceleration gap showing the enhancement at the triple point.

The field enhancement at the triple point increases the probability of electron emission from the metal rings. These seed electrons propagate towards the next metal ring that has a higher potential. Along the way, these electrons collide with the surface of the insulator generating secondary electrons. Secondary electrons collide with the insulator surface, resulting in the creation of additional electrons. This cascading effect develops into secondary electron emission avalanche (SEEA) [32].

Electrons colliding onto the insulator surface displace neutral gas and ions trapped on the insulator surface. Collisions between electrons, ions, and neutrals result in the formation of a plasma channel between the rings. The rings delay the formation of a continuous plasma channel between the anode and cathode, thereby increasing the breakdown hold-off time of the gap.

The overall field distribution in the post-acceleration gap is simulated and shown in Figure 5.30. The electric field is largest in the region above the metal rings closest to the anode. The minimum E_z field is ~ -5x10^6 V/m at the rounded top of the cone.

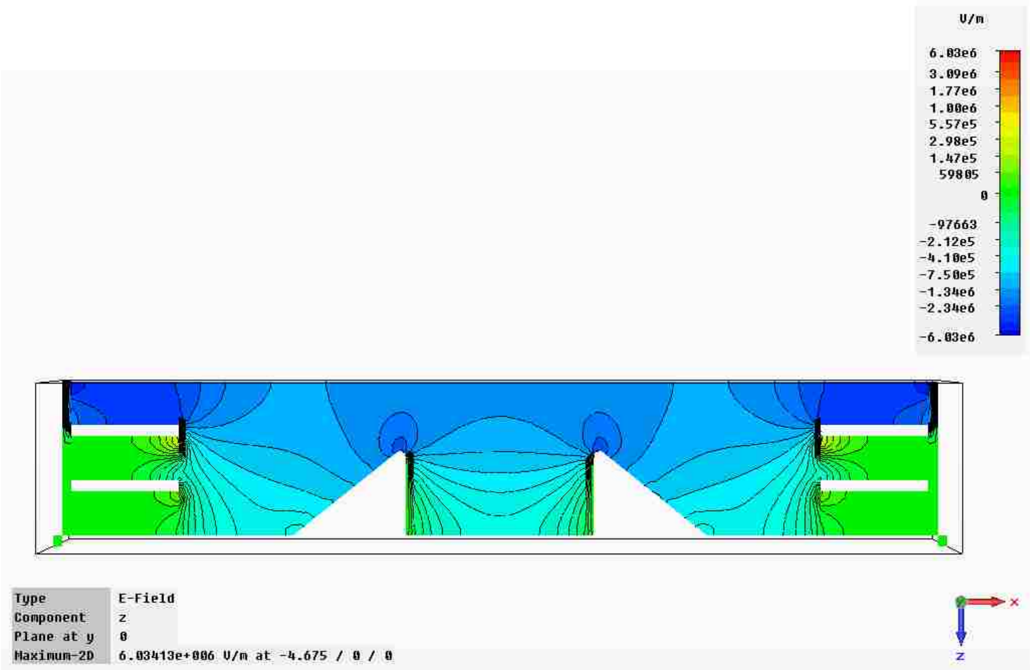

Type	E-Field
Component	z
Plane at y	0
Maximum-2D	6.03413e+006 V/m at -4.675 / 0 / 0

Figure 5.30: E_z field distribution inside the post acceleration gap.

The E_z field calculated using the analytical model of the A-K gap is of the same order of the E_z field simulated using CST. For an insulator thickness of 0.75 inch, the E_z field on the surface of the cathode electrode does exceed 150 kV/cm. We either have to insulate the surface of the cathode electrode or increase the thickness of the insulator. However, increasing the thickness of the insulator reduces the average E_z field in the A-K gap. The velvet cathode may not emit uniformly in such reduced fields.

The analytical model of the post-acceleration gap does not accurately predict the E_z field in the region inside the cone. In the model, the E_z field decays very rapidly as we calculate deeper into the cone. CST simulations show that the E_z field decays at a more gradual rate.

CHAPTER 6: MAGIC SIMULATIONS OF UNM LOW POWER RELTRON

The UNM reltron is simulated using MAGIC v2011 [9] developed by Mission Research Corporation (ATK/MRC). MAGIC is a PIC code that utilizes the Finite Difference Time Domain (FDTD) to calculate the interaction between macro particles and EM fields in space and time. MAGIC divides the simulation space into grids to form a system of Yee cells [33]. The EM fields are located at the edge of the cells (Figure 6.1) and the particles are contained within the cells.

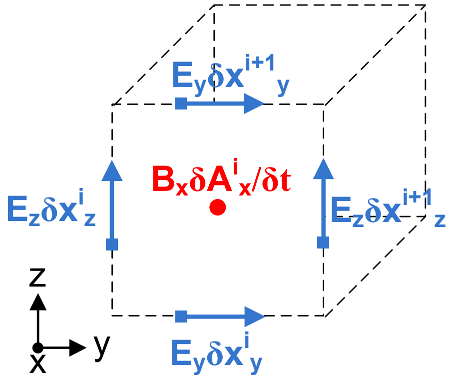

Figure 6.1: YZ plane field components of the Yee cell.

MAGIC first solves Ampere's law with displacement current followed by Faraday's law a half cell away. Electric fields are solved at integer time steps while magnetic fields are solved at every integer plus half time step. For each particle, MAGIC uses pre-defined initial conditions or solutions from the previous time step to solve the relativistic Lorentz force. The Lorentz force is resolved using the kinematics integration algorithm published by Boris [34]. It is a three-step process where we add half the electric impulse to the momentum vector, rotate the momentum vector through the magnetic field and apply the remaining half of the electric impulse. The particles' positions are updated by multiplying the particles' velocities with the time step and adding it to the initial position. The moving particles in the cells become the source current that generates the electric fields. In this manner the particles' equations are solved self consistently, as shown in Figure 6.2.

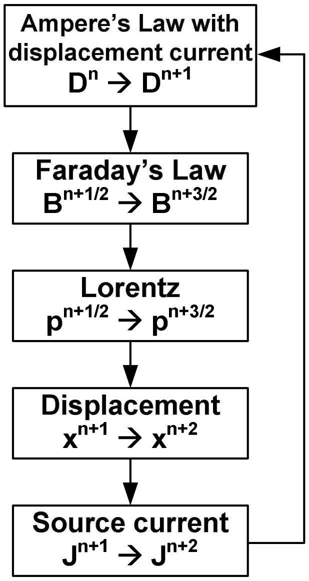

Figure 6.2: Flow chart depicting the MAGIC pseudocode.

MAGIC comes with built-in functions that allow the user to construct simulation objects from basic shapes such as cylinders, cones, etc. It also comes with many physical models such as the foil model that simulates beam scattering through a thin conductor [35]. MAGIC comes with a set of diagnostics and post-processing tools to analyze and display simulation results. Figure 6.3 shows a side view of the reltron modeled in MAGIC. The parts in blue represent PEC and the parts in green represent lossless dielectric. All parts are axisymmetric or off-axis symmetric, except for the extraction cavity.

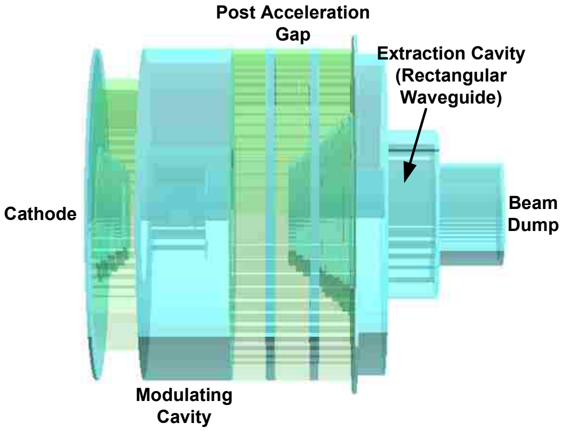

Figure 6.3: MAGIC model of the UNM reltron.

Figure 6.4 shows the dimensions of the UNM reltron modeled in MAGIC. The reltron is driven by two input ports (Portin1 and Portin2) that form the input boundaries allowing incoming waves to enter and reflected waves to leave the simulation space. In all simulations the Marx voltage is divided across the A-K gap (Portin1) and the post-acceleration gap (Portin2) in the ratio 2:1.

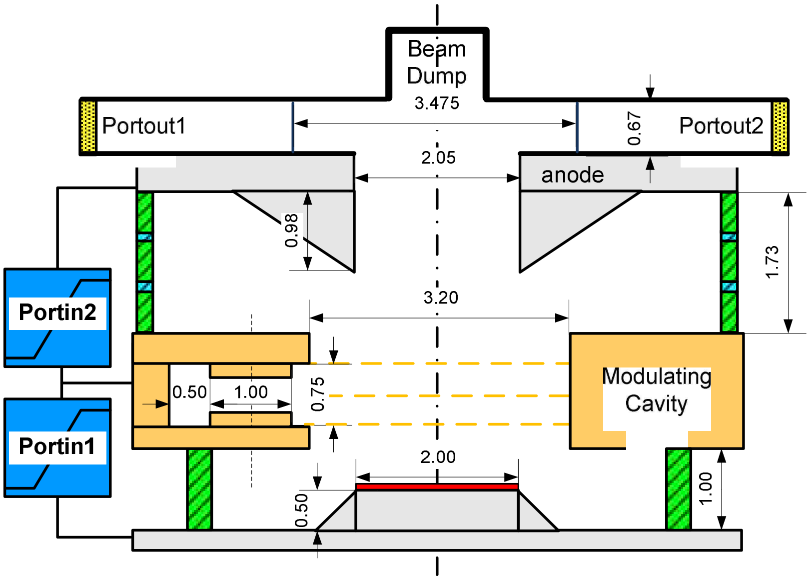

Figure 6.4: Dimensions of the UNM reltron modeled in MAGIC (inches).

The cathode is modeled using the explosive emission function with threshold field set to 30 kV/cm. Electrons are emitted uniformly over the cathode surface at a uniform rate. The modulating cavity is covered by three grids that are modeled using the foil model in MAGIC. The foil model allows electrons to pass through and calculates electron scattering and absorption based on the foil material and thickness. Electron transport is calculated using the Integrated TIGER Series (ITS 3.0) computer code. It is a time independent 2D/3D coupled electron/photon Monte Carlo transport code [36]. EM fields see the foil as a perfect conductor. Tungsten grids are used in the modulating cavity with thickness 76.2 μm, 89.5% transparency. The extraction cavity uses aluminum grids, 5 μm thick, 95% transparency. All metal walls are PEC and the dielectric rings are lossless with a relative permittivity of 3.0.

The circuit command is used in conjunction with the port function to send a time-varying voltage waveform through the ports. The circuit function introduces a feedback loop to keep the voltage at the desired magnitude for each time step. This gives us a very stiff voltage pulse that has a relatively flat top. The input ports supply power to the reltron by launching a TEM wave between the anode and cathode of the ports (Figure 6.5).

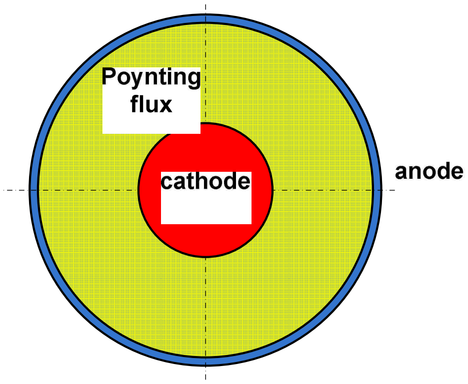

Figure 6.5: Bottom view of the input port in MAGIC simulations.

We obtain the input power by integrating the Poynting flux $\vec{S}$ over the area between the anode and cathode

$$\vec{P} = \int \vec{S}(r,\vartheta,z,t)dA$$

$$= \int_{0}^{2\pi}\int_{r_c}^{r_a} \vec{E}(r,\vartheta,z,t) x \vec{H}(r,\vartheta,z,t)\, dr\, r\, d\vartheta, \qquad (6.1)$$

where r_c is the radius of the cathode and r_a is the inner radius of the anode.

The irises in the extraction cavity are located inside the rectangular waveguide equidistant from the center axis. We maximize microwave power generation by optimizing the iris window width to 2 inch. This is the window width that allows the greatest amount of microwaves to leave the cavity while keeping the right amount of microwaves in the extraction cavity to extract energy efficiently from the electrons. Microwaves are extracted from the reltron using two output ports placed at the end of the waveguide (Portout1 and Portout2). These ports form a perfectly matched layer (PML), preventing waves from being reflected back into the reltron. Microwave power is calculated from the Poynting vector through the surface area of the ports that face inwards.

The EM fields are computed using the Maxwell Biased algorithm. This solver is an iterative time-biased implicit solution of Maxwell's equations that damps high-frequency noise arising from relativistic particles, poor particle statistics, or numerical instabilities. At each time step the solver iterates between the electric and magnetic fields. The electric fields have relaxation coefficients applied to them and these coefficients are relaxed at each iteration until Maxwell's equations are satisfied. This algorithm is computationally more expensive but is able to handle relativistic particles very well. The minimum grid size used in the simulation is dz=0.05 inch, dr=0.1 inch and dθ= 5°.

The space charge in the A-K gap is governed by the Child-Langmuir space charge current limit [37]

$$J_{child} = \frac{4\varepsilon_0}{9}\left(\frac{2q_e}{m_e}\right)^{1/2}\frac{V_b^{\ 3/2}}{d_{AK}^{\ 2}}. \tag{6.2}$$

In the relativistic limit, the Child Langmuir current limit becomes [37]

$$J_{rel\_child} = \frac{\varepsilon_0 m_e c^3}{2q_e d_{AK}^{\ 2}}\left[\int_1^{\gamma(d_{AK})}\frac{d\gamma}{\left(\gamma^2-1\right)^{1/4}}\right]^2. \tag{6.3}$$

The beam current propagating through the extraction cavity drift tube has been derived independently by Bogdankevich and Rukhadze [38], and Nation and Read [39]

$$I_{BR} = I_0\frac{\left(\gamma^{2/3}-1\right)^{3/2}}{1+2\ln(r_{wg}/r_b)}. \tag{6.4}$$

The current limits are for a cold beam and do not account for energy spread. Figure 6.6 plots the three current limits for a beam radius of 1.0 inch and A-K gap of 0.6 inch as a function of beam voltage.

6.1 UNM LOW POWER RELTRON WITH 0.6 INCH A-K GAP

We set the Marx voltage at 70 kV which gets divided across the A-K gap and post-acceleration gap in the ratio 2:1. The A-K gap is driven by a 46.6 kV step voltage with a 1 ns rise time, as shown in Figure 6.7. The post-acceleration gap is driven by a 23.3 kV step voltage with 1 ns rise time, as shown in Figure 6.8.

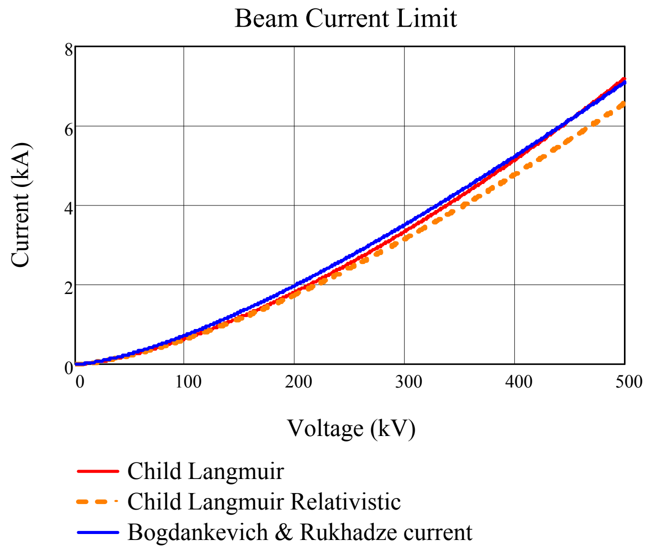

Figure 6.6: Space-charge-limited current as a function of beam voltage.

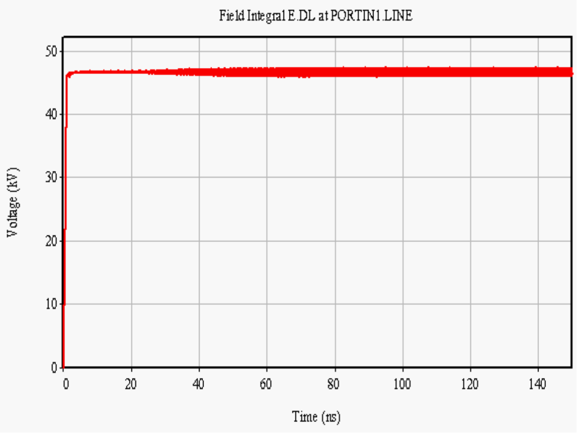

Figure 6.7: Beam voltage as a function of time in MAGIC simulations.

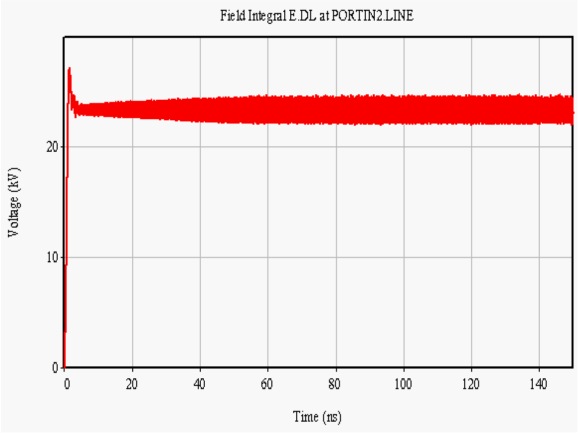

Figure 6.8: Post-acceleration voltage as a function of time in MAGIC simulations.

The beam power and post-acceleration power are plotted in Figure 6.9 and Figure 6.10, respectively. When the reltron saturates, it draws an average beam power of 16.5 MW.

MAGIC considers the power delivered to the post-acceleration gap to be reactive power because the anode and cathode of the input port from the post-acceleration gap do not emit any electrons. The beam propagating though the post-acceleration gap originates from the A-K gap. Power, calculated by integrating the Poynting flux from the input port, oscillates about a positive offset from the time axis.

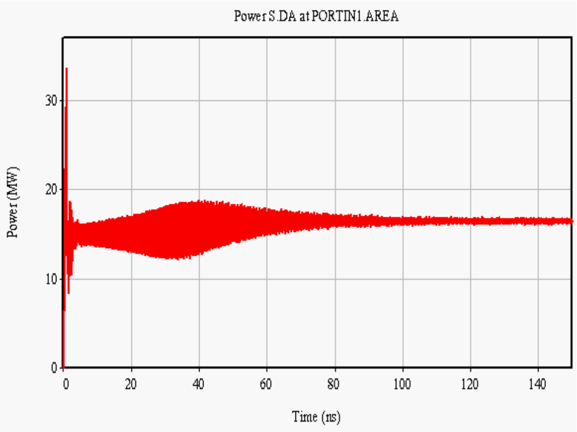

Figure 6.9: Beam power from MAGIC simulations.

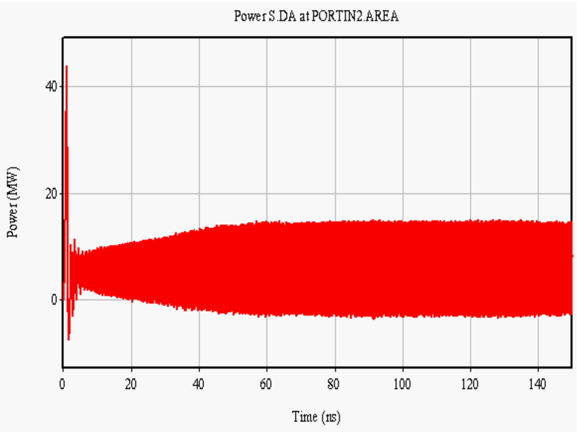

Figure 6.10: Post acceleration power from MAGIC simulations.

In the A-K gap, the Child-Langmuir current limit for a 46.6 kV beam is 205 A. In the extraction gap, the Bogdankevich and Rukhadze current limit for a 70 kV beam is 433 A. We measure the beam current emitted from the cathode surface Figure 6.11 and the average beam current entering the cavity $I_0 = 355$ A.

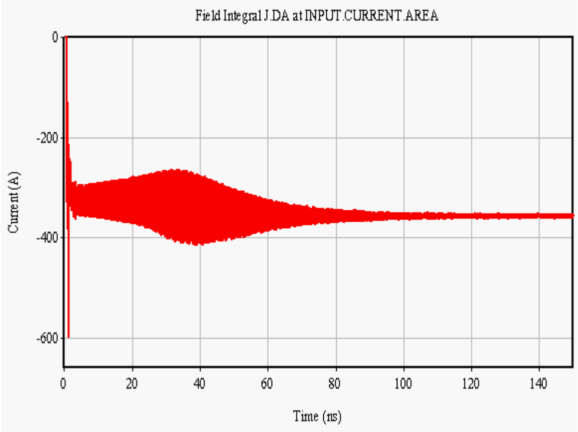

Figure 6.11: Beam Current as a function of time in MAGIC simulations.

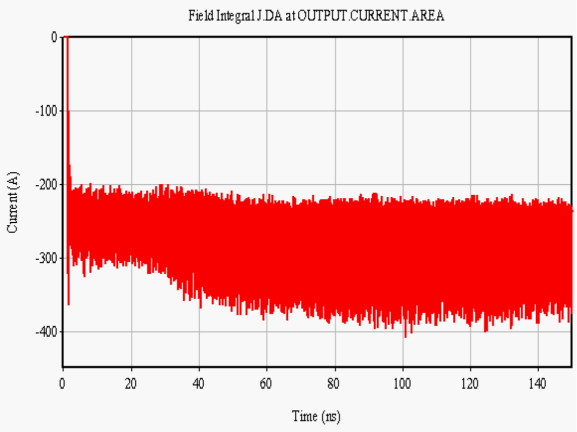

Figure 6.12: Modulating Current as a function of time in MAGIC simulations.

We also measure the modulating current just as the beam exits the modulating cavity (Figure 6.12). The peak modulating current $I_{RF} = 393$ A. We obtain the modulation coefficient by dividing the modulation current with the beam current

$$MC = \frac{I_{RF}}{I_0} = \frac{393}{355} = 1.1. \tag{6.5}$$

Figure 6.13 shows the electrons' position 120 ns into the MAGIC simulation (r-z view is presented). We see an electron bunch in the extraction cavity and another forming as it enters the drift tube. Some electrons do get intercepted by the metal hollow cone that forms the drift tube.

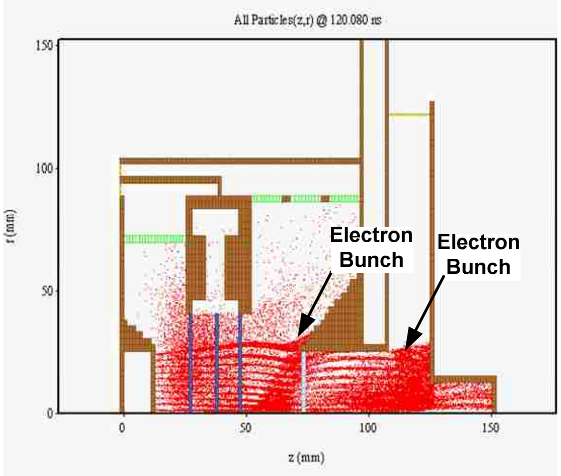

Figure 6.13: Electrons' position at 120 ns into the simulation. The simulation uses a grid thickness of 76.2 μm with 89.5% transparency.

At 120 ns, we plot the electrons' momentum (Figure 6.14) and K.E. (Figure 6.15). The modulating cavity is located between z = 28 mm z = 48 mm. The extraction cavity drift tube starts at z = 71 mm and its rectangular waveguide starts at z = 108 mm. The red lines in the phase space plots are formed by individual macro particle that have similar momentum / K.E.

In the A-K gap, the electrons undergo rapid acceleration to 43.3 keV as shown by the steep line gradient. Line thickness represents energy spread within the beam. The beam enters the modulating cavity with a narrow energy spread so the beam is cold. The line thickens in the modulating cavity, indicating a larger energy spread due to collisions, scattering by the grids, and velocity modulation.

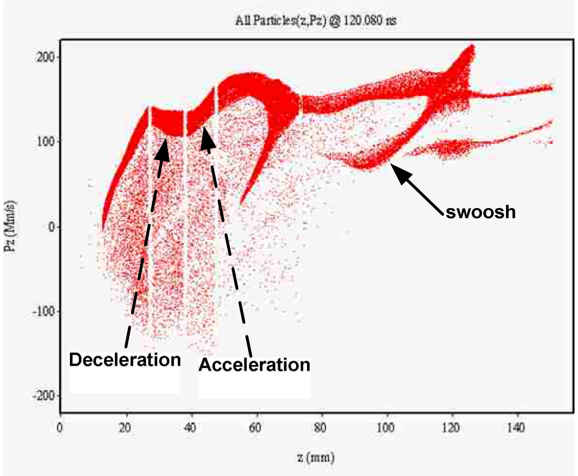

Figure 6.14: Plot of electrons' phase space.

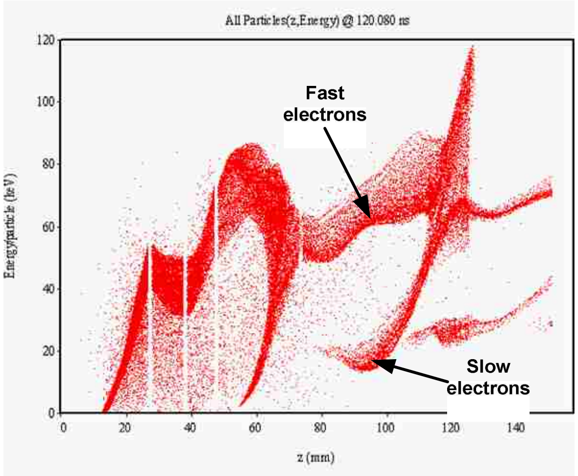

Figure 6.15: Plot of electron's K.E..

In the modulating cavity the electrons experience deceleration in the first gap and acceleration in the second gap. This gives the electrons a V-shaped momentum / K.E. distribution. Electrons experience a larger momentum change in the second gap and leave the cavity with peak energy of 90 keV. In the next half cycle, the electrons experience a reversal in the Lorenz force and get accelerated in the first gap and decelerated in the second gap. Electrons that are accelerated in the second gap leave the modulating cavity with velocity greater than that corresponding to the initial beam energy. Similarly, electrons that are decelerated leave the cavity with velocity less than that corresponding to the initial beam energy. This velocity modulation gives the electrons an energy spread of 0 – 80 keV but the beam has an energy spread ~20 keV (estimated from the line thickness). Some electrons have negative velocity because of backscattering from the grids and velocity modulation by the EM fields. These electrons can be reflected back to the cathode.

In the post-acceleration gap electrons continue to accelerate / decelerate. Once the electrons enter the extraction cavity, they attain a two population momentum / K.E. distribution. The top population is formed by fast electrons that experienced acceleration as they leave the modulating cavity. The lower population is formed by electrons that experienced deceleration as they leave the modulating cavity. The fast electrons in front of the population overtake the slow electrons in the back of the population as the slow electrons require a longer transit time to the traverse the drift distance. The two populations are joined by electrons that have an energy spread that spans the two populations. The electrons with an intermediate velocity are electrons that experience deceleration in the second gap, but not forceful enough to decelerate the electrons to the slow population. Together, the fast, slow, and intermediate velocity electrons take the shape of a swoosh in the momentum / K.E. graph. The gradient of the swoosh decreases over time as the electrons decelerate to give up their energy to produce microwaves.

The E_z fields in the modulating cavity and extraction cavity are shown in Figure 6.16 and Figure 6.17, respectively. The E_z fields in both cavities grow consistently and saturate after 60 ns.

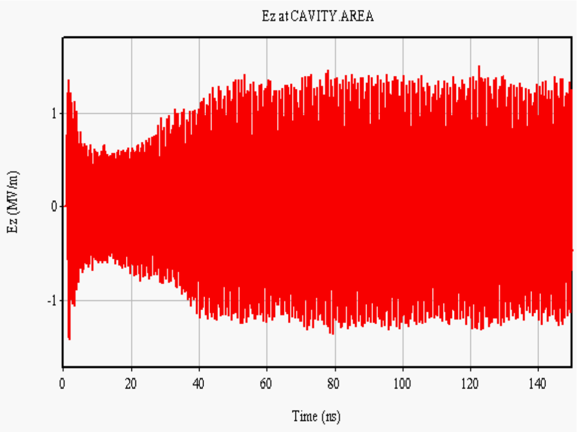

Figure 6.16: E_z field of modulating cavity from MAGIC simulations.

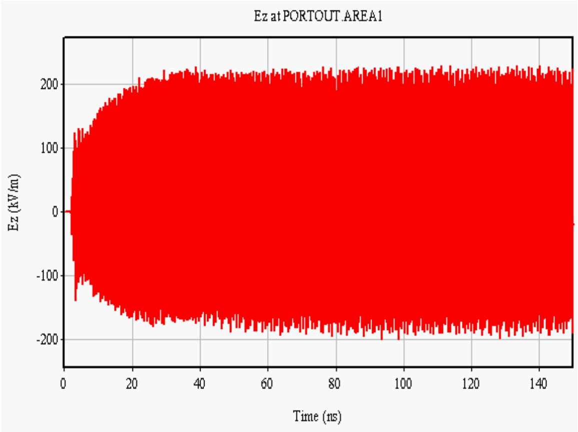

Figure 6.17: E_z field of extraction cavity from MAGIC simulations.

The frequency spectrum of the E_z field in the main cavity is plotted in Figure 6.18. We only observe the dominant TM_{010} mode oscillating at 2.748 GHz and the TM_{020} mode at 6.669 GHz. The frequency spectrum of the E_z field in the extraction cavity is plotted in Figure 6.19. The highest magnitude is the TM_{010} mode at 2.748 GHz and the next highest is the 2^{nd} harmonic TM_{010} mode at 5.499 GHz. We also see the TM_{110} mode 3.920 GHz appearing as the third highest component.

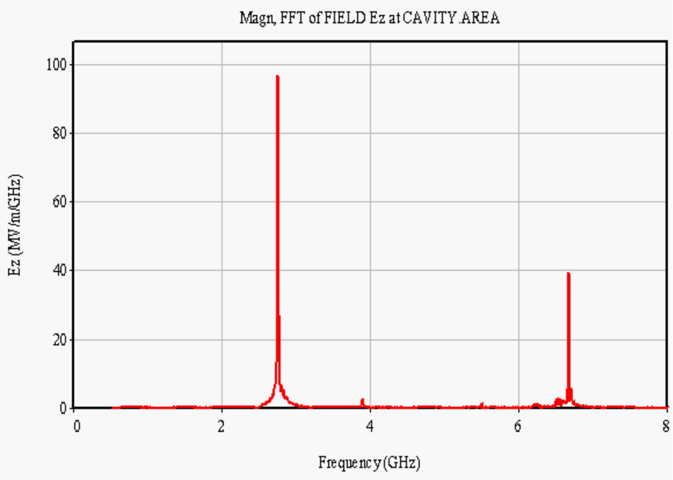

Figure 6.18: Frequency spectrum of the E_z field in the main cavity from MAGIC simulations.

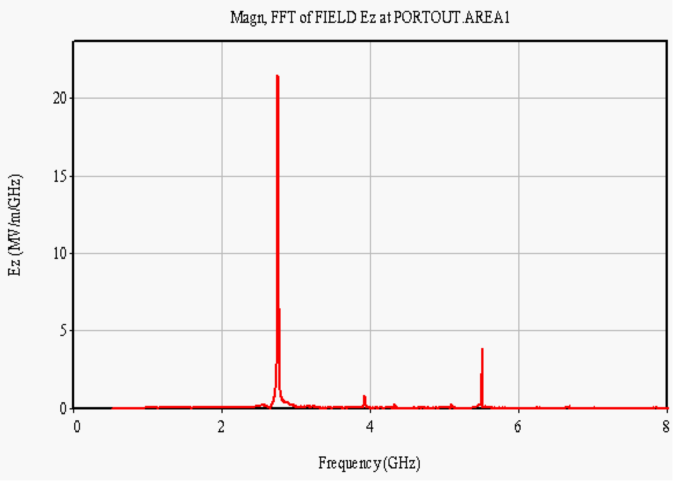

Figure 6.19: Frequency spectrum E_z field from portout1 from MAGIC simulations.

We perform a time frequency analysis of the E_z field in the modulating cavity (Figure 6.20) and extraction cavity (Figure 6.21).

In the modulating cavity, the TM_{010} mode is the dominant mode throughout the simulation. The TM_{020} mode appears after 42 ns into the simulation. In the extraction cavity we see only the TM_{010} mode throughout the simulation as the higher order modes are too small in magnitude compared to the TM_{010} mode. The higher order modes become negligible in magnitude after MAGIC processes the E_z field using its internal time frequency algorithm.

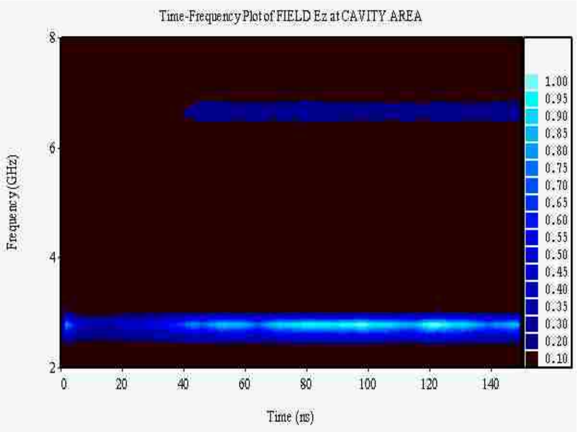

Figure 6.20: Time frequency plot of the E_z field in modulating cavity from MAGIC simulations.

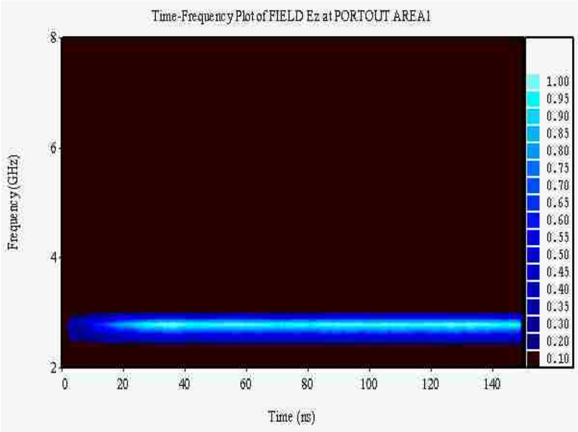

Figure 6.21: Time frequency plot of the E_z field in extraction cavity from MAGIC simulations.

The microwave power is calculated by integrating the Poynting flux over the cross sectional area of the output port. This gives the total power transmitted through the waveguide. The output power through portout1 is shown in Figure 6.22. Peak power is 227 kW, giving a total power of 454 kW from the two ports.

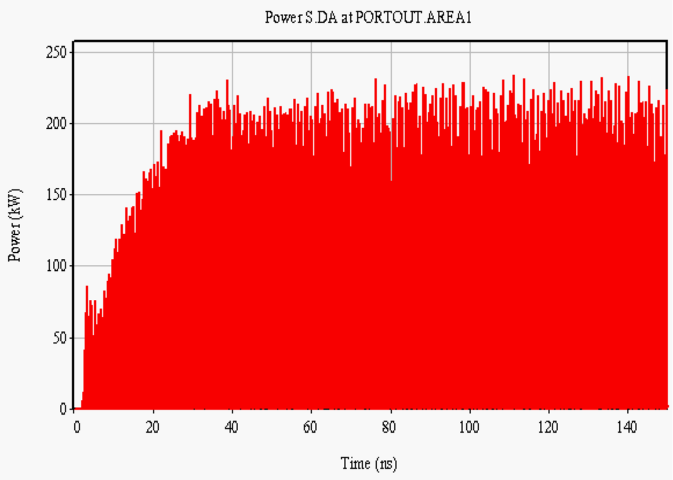

Figure 6.22: Output power from portout1 from MAGIC simulations.

We repeat our MAGIC simulations for the 0.6 inch A-K gap with Marx voltage varying from 60 kV to 100 kV. Figure 6.23 plots the microwave power generated by the reltron in the simulations. For the reltron to generate MW levels of microwave power, the Marx generator has to be charged to a minimum of 82.5 kV.

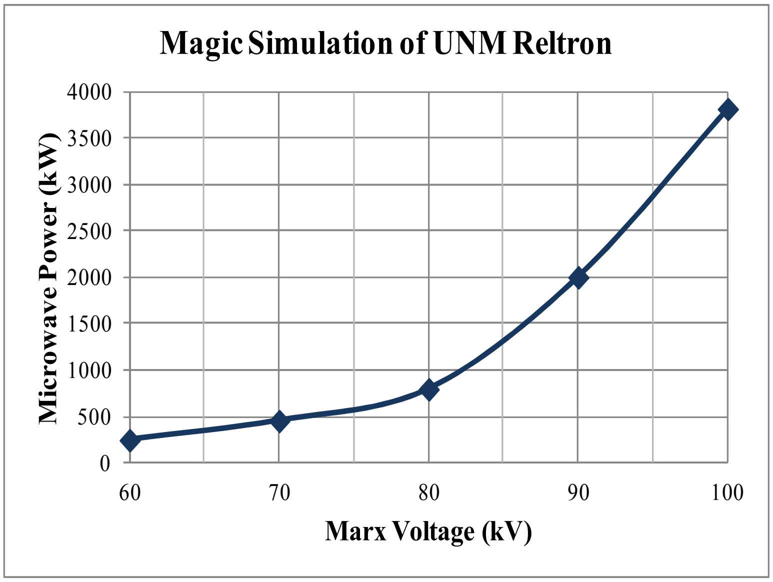

Figure 6.23: Microwave power as a function of Marx voltage.

6.2 UNM LOW POWER RELTRON WITH 0.525 INCH A-K GAP

We set the Marx voltage to 80 kV with a 1 ns rise time. This gives an A-K gap voltage of 53.3 kV (Figure 6.24) and post acceleration gap voltage of 26.6 kV (Figure 6.25).

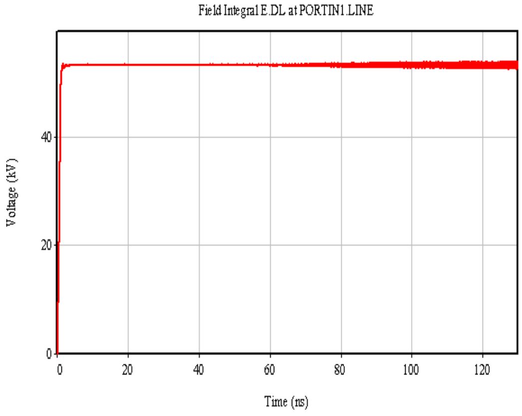

Figure 6.24: Beam voltage as a function of time in the MAGIC simulations.

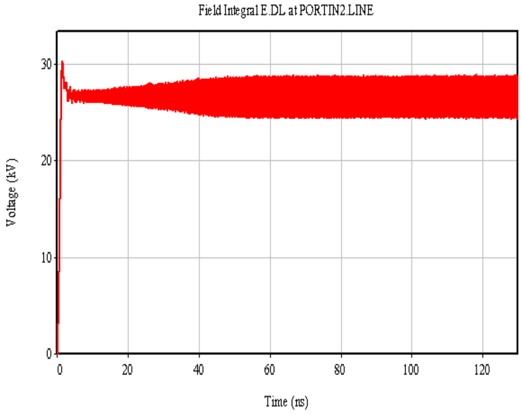

Figure 6.25: Post-acceleration voltage as a function of time in the MAGIC simulations.

The saturated beam power (Figure 6.26) is 28 MW and the post-acceleration power is reactive (Figure 6.27).

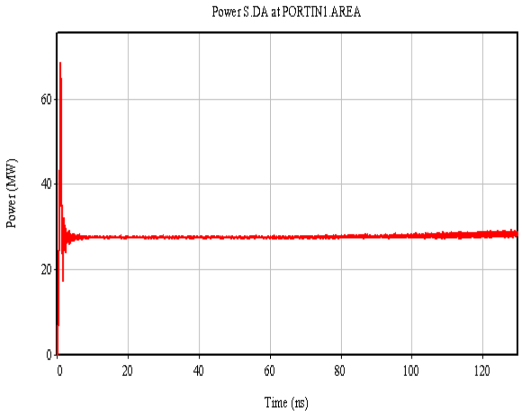

Figure 6.26: Beam power from MAGIC simulations.

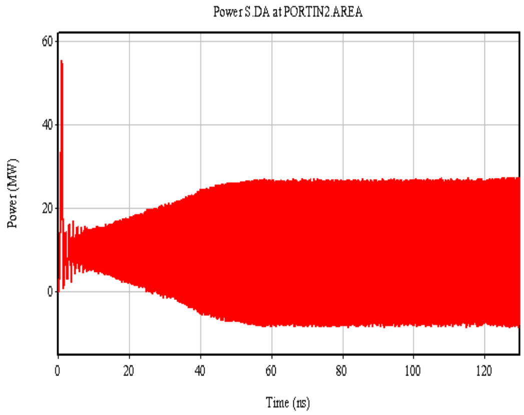

Figure 6.27: Post-acceleration power from MAGIC simulations.

In the A-K gap, the Child Langmuir current limit for a 53.3 kV beam is 250 A. In the extraction gap, the Bogdankevich and Rukhadze current limit for a 80 kV beam is 527 A. The average beam current entering the cavity is I_0 = 541 A (Figure 6.28) and the peak modulating current is I_{RF} = 643 A (Figure 6.29).

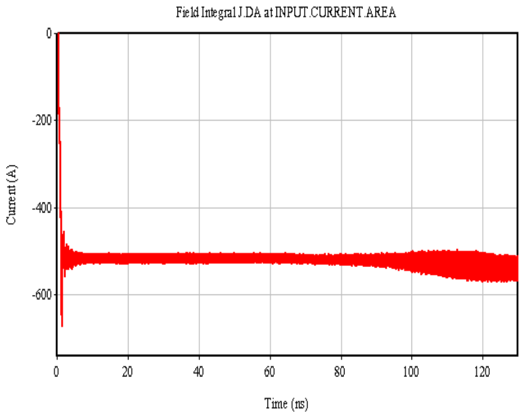

Figure 6.28: Beam current as a function of time

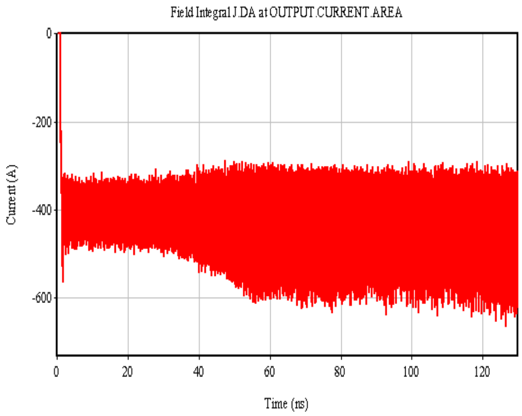

Figure 6.29: Modulating current as a function of time

The modulation coefficient is

$$MC = \frac{I_{RF}}{I_0} = \frac{643}{541} = 1.18. \tag{6.6}$$

Figure 6.30 shows the electrons position 126 ns into the MAGIC simulation (r-z view is presented). We see an electron bunch entering the drift tube of the extraction cavity and another inside the extraction cavity waveguide.

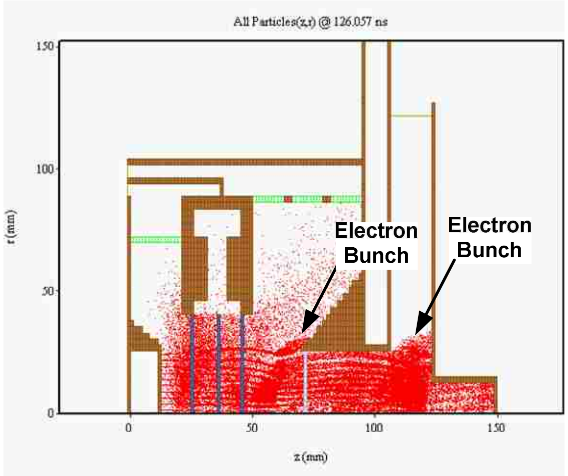

Figure 6.30: Electrons' position at 126 ns into the simulation. The simulation uses a grid thickness of 76.2 μm with 89.5% transparency.

At 126 ns, we plot the electrons' momentum (Figure 6.31) and K.E. (Figure 6.32). The modulating cavity is located between z = 26 mm z = 46 mm. The extraction cavity drift tube starts at z = 69 mm and its rectangular waveguide starts at z = 106 mm.

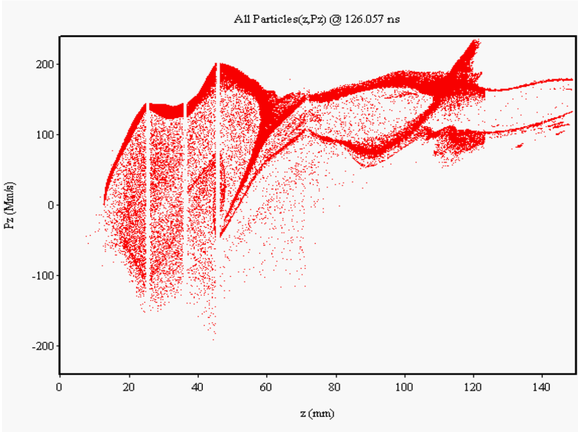

Figure 6.31: Plot of electron's phase space.

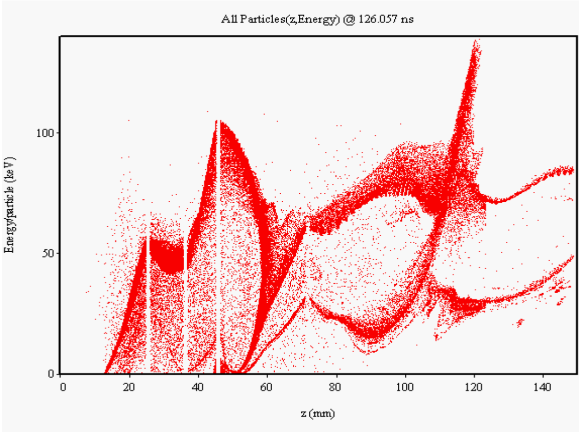

Figure 6.32: Plot of electrons' K.E..

We shall compare our results with the 70 keV beam (0.6 inch A-K gap). In the modulating cavity electrons in the second gap experience a larger momentum change as seen from the steeper line gradient. Electrons leave the modulating cavity with higher peak energy of 110 keV and larger energy spread of 0 – 110 keV. However, the bulk of the electrons now have a narrower energy spread ~ 10 keV (thinner lines). There is now a distinct stream of electrons with negative velocity reflecting back from the third grid.

In the extraction cavity, the electrons attain a two population momentum / K.E. distribution comprising of fast and slow electrons. Downstream, we see the intermediate velocity electrons spanning the two populations creating a swoosh momentum / K.E. distribution. The decrease in momentum is more prominent as the line exhibits a larger decrease in gradient over time.

The E_z fields in the modulating cavity and extraction cavity are shown in Figure 6.33 and Figure 6.34, respectively. The E_z fields in both cavities saturates after 60 ns.

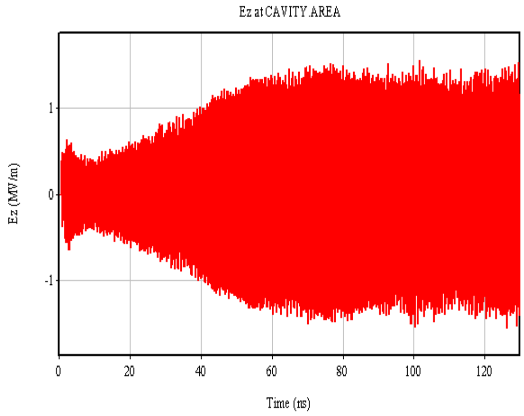

Figure 6.33: E_z field of modulating cavity from MAGIC simulations.

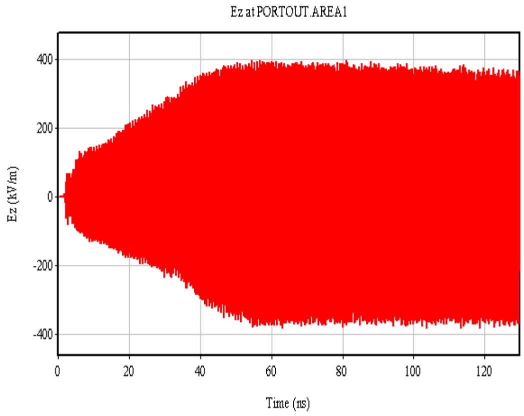

Figure 6.34: E_z field of extraction cavity from MAGIC simulations.

The frequency spectrum of the E_z field in the main cavity is plotted in Figure 6.35. The TM_{010} mode is very dominant at 2.745 GHz, while the magnitude of the TM_{020} mode is very small at 6.522 GHz.

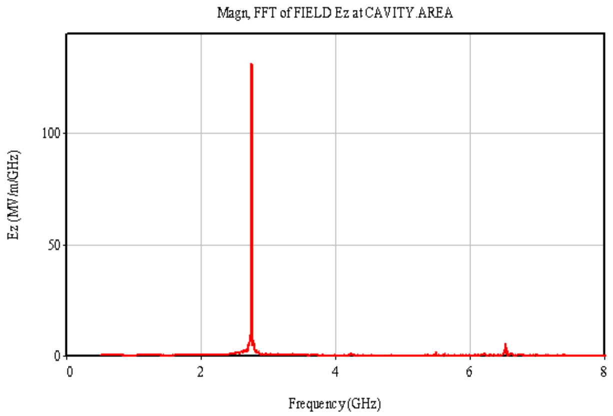

Figure 6.35: Frequency spectrum of the E_z field in the main cavity from MAGIC simulations.

The frequency spectrum of the E_z field in the extraction cavity is plotted in Figure 6.36. The dominant TM_{010} mode is at 2.746 GHz and the 2nd harmonic TM_{010} mode is 5.490 GHz.

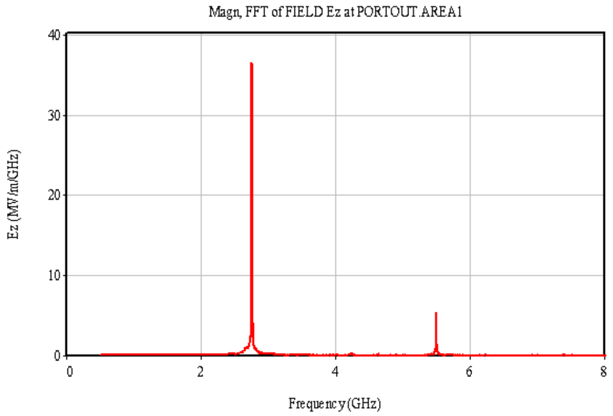

Figure 6.36: Frequency spectrum of the E_z field from portout1 from MAGIC simulations.

We perform a time frequency analysis of the E_z field in the modulating cavity (Figure 6.**37**) and extraction cavity (Figure 6.38). For both cavities, the TM_{010} mode is the dominant mode throughout the simulation. The TM_{010} mode saturates after 51.2 ns and remains light blue until the end of the simulation.

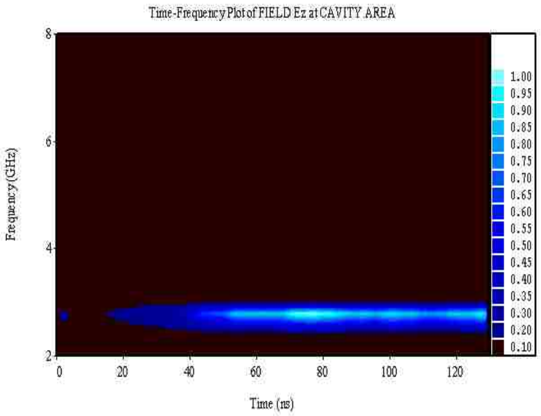

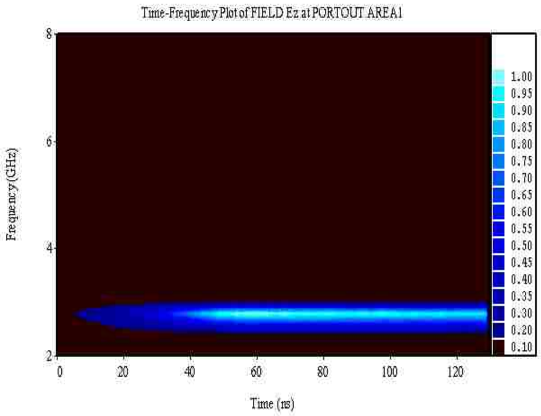

Figure 6.37: Time frequency plot of E_z field in the modulating cavity from MAGIC simulations.

Figure 6.38: Time frequency plot of E_z field in the extraction cavity from MAGIC simulations.

Peak power through portout1 is 640 kW (Figure 6.39), giving a total power of 1.28 MW from the two ports.

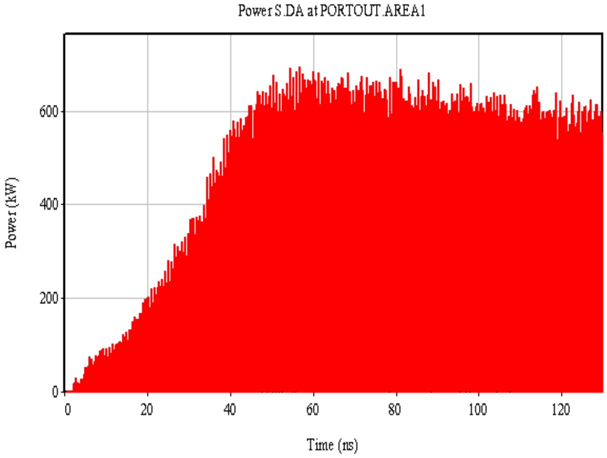

Figure 6.39: Output power from portout1 from MAGIC simulations.

6.3 UNM LOW POWER RELTRON WITH VARIABLE A-K GAP

We perform a parametric study with A-K gaps of 0.45 inch, 0.525 inch, and 0.6 inch. For each A-K gap, we vary the Marx voltage from 60-90 kV. We plot the total microwave power generated for increasing A-K gaps and Marx voltages (Figure 6.40). In all simulations we use the same modulating cavity and extraction cavity dimensions.

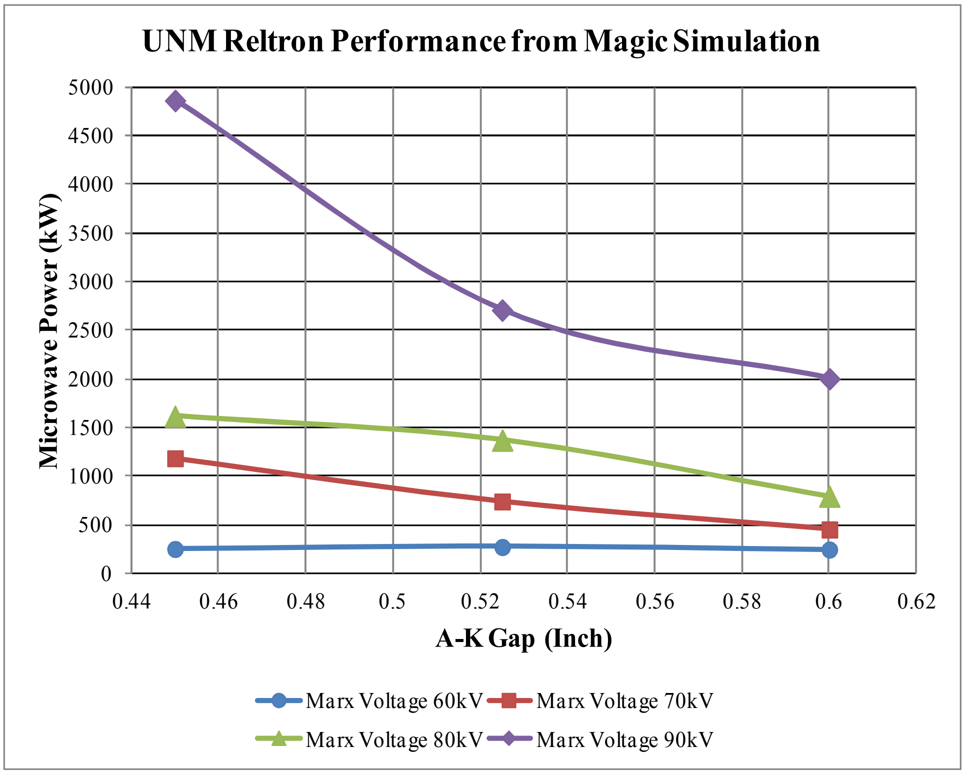

Figure 6.40: UNM low power reltron performance chart from MAGIC simulations.

For a Marx voltage of 60 kV, microwave power is almost independent of the A-K gap. Microwave power for the 0.525 inch A-K gap is 274 MW and is 10% higher than for the 0.6 inch A-K gap and 7.8% higher than for the 0.45 inch A-K gap. Above 70 kV, microwave power decreases piecewise linearly for increasing A-K gaps. We conclude that a minimum Marx voltage of 70 kV is required for optimum microwave generation. The UNM reltron is able to generate microwave power in the megawatt range for Marx voltages 80 kV or higher and A-K gaps of 0.525 inch and smaller.

CHAPTER 7: EXPERIMENTS ON THE UNM RELTRON

Figure 7.1 shows a photograph of the reltron experimental setup. The reltron is placed above the Marx generator which is housed inside the 2.5’ x 2.5’ x 3’ tank filled with transformer oil. The vacuum system is connected on top of the reltron using a KF50 vacuum T joint. The reltron radiates into a vacuum waveguide load through the directional coupler. The controls and diagnostics are placed behind the reltron inside metal enclosures.

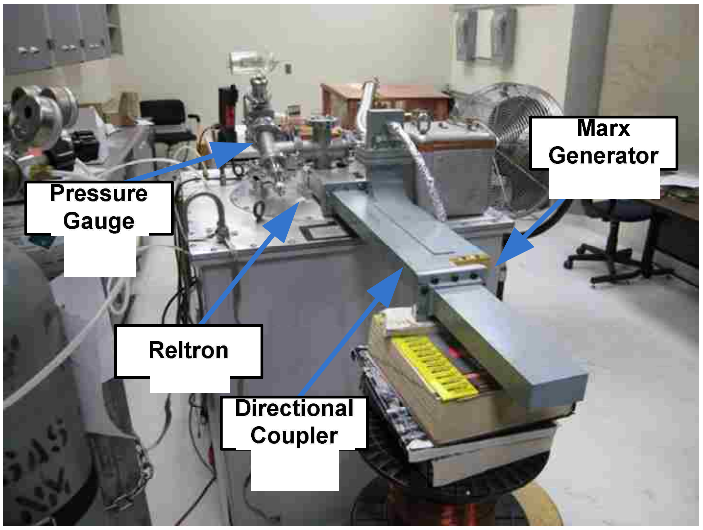

Figure 7.1: Photograph of the reltron experimental setup.

Figure 7.2 shows a block diagram of the power modulator system that powers the reltron [11].

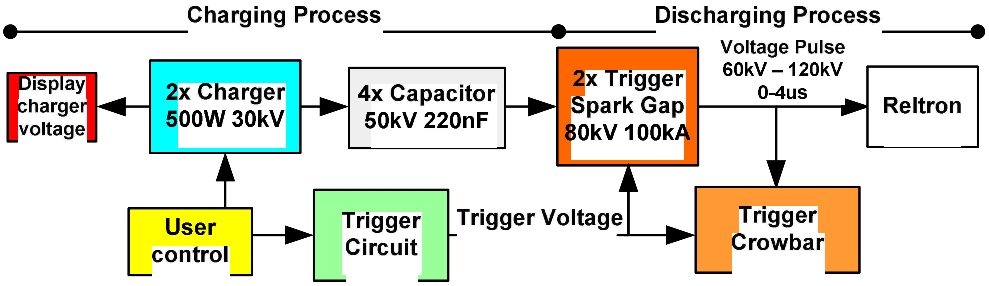

Figure 7.2: Block diagram of reltron power modulator system.

The user presets the pulse duration and PRR before charging up the capacitors to the desired voltage. The chargers are switched off before the user toggles the trigger circuit to close the spark gaps, which in turn erect the Marx generator. A microprocessor triggers the crowbar after a preset delay, shunting power away from the reltron. Manual control of the charging voltage eliminates the chances of pre-fire.

7.1 IMPROVEMENTS TO THE LOW POWER RELTRON

7.1.1 Modulating Cavity Base Plate

We redesigned a base plate for the modulating cavity to improve the voltage hold off capability of the A-K gap, as indicated in Figure 7.3.

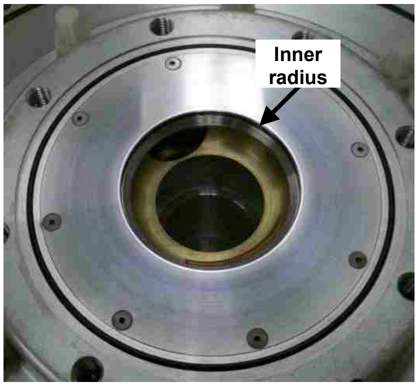

Figure 7.3: Redesigned modulating cavity base plate in the reltron.

The previous plate inclined from the outer to the inner radius. From our electrostatic analysis we showed that a flat plane best distributes the normal electric field in the gap. The inner radius of the plate covers the countersunk screws that hold the grids in place. Previously, breakdown occurred between the cathode and the screws because of field enhancement on the screw heads. The inner radius of the redesigned plate is also rounded to 0.0365 inch to minimize the peak electric field on the rounded corner.

Our electrostatic analysis also shows the normal electric fields on the cathode base plate exceed 150 kV/cm. We apply Glyptal® on the entire base plate and the cathode holders to increase the breakdown threshold above 150 kV/cm (see the photograph in Figure 7.4).

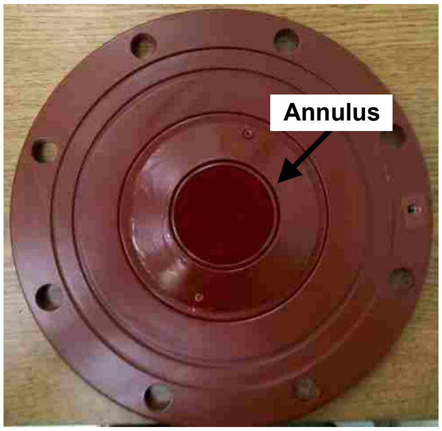

Figure 7.4: Glyptal®-coated cathode base plate with the red velvet cathode material in the center.

We also installed an annulus around the cathode to reduce field enhancement and to improve the electric field's distribution within the gap. The slope of the annulus reduces the electric field's magnitude and decreases the electric field gradient from the cathode to the base plate.

7.1.2 The A-K Gap and Post-Acceleration Gap Insulators

Using the results form our electrostatic analysis in Chapter 5, we machined A-K gap insulators with thicknesses ranging from 0.7 inch to 1.025 inch using Rexolite®, which is a cross linked polystyrene. Figure 7.6 shows the dimension of our 0.839 inch thick A-K gap insulator.

From our experiments, we deduced that Rexolite® has a breakdown threshold over 40 kV/cm. When breakdown occurs, we see arcing tracks on the Rexolite®. We can recover the hold off voltage by machining and polishing the surface that was scarred by electron streams.

The insulators in the post-acceleration gap are made from Polymethyl methacrylate (trademark Lucite® or Plexiglass®). On occasion we do experience breakdown in the gap. We varied the thicknesses of the insulators in the gap to improve the voltage hold off. Figure 7.6 shows the dimension of the thickest post acceleration insulator used. We can only vary the thickness from 0.475 inch to 0.625 inch so the increase in voltage hold off is minimal.

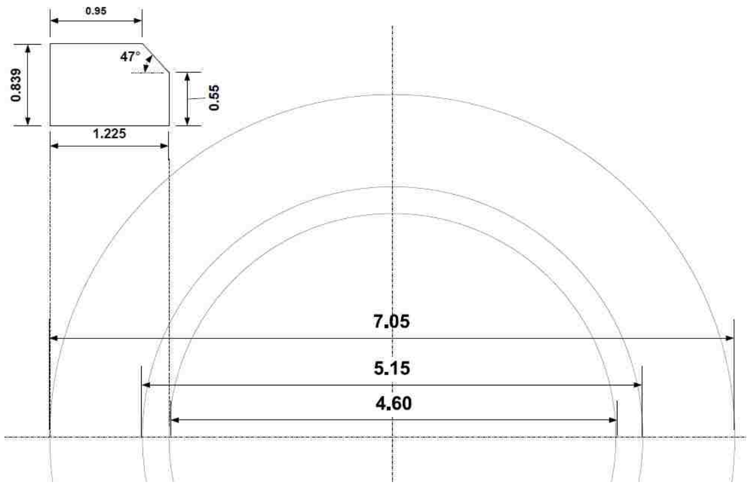

Figure 7.5: Top and side view of the cathode insulator. Dimensions are in inches.

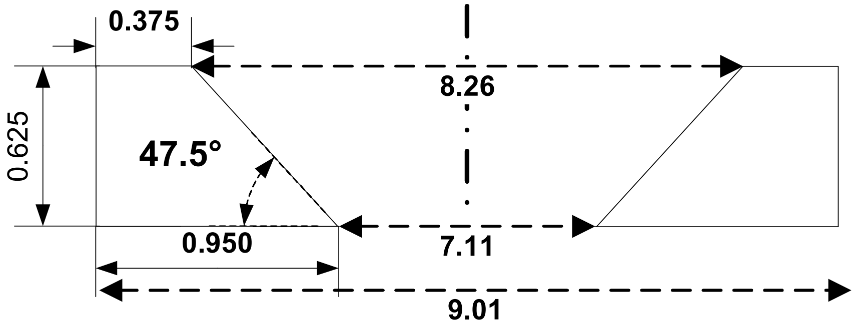

Figure 7.6: Dimension of the post acceleration insulator ring. Dimensions are in inches.

Once we implemented the improvements to the reltron, we were able to achieve relatively flat-top Marx voltages (Figure 7.7), post acceleration voltages (Figure 7.8), and current pulses (Figure 7.9).

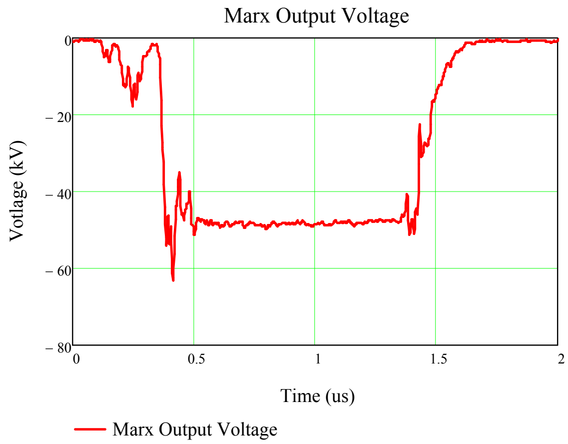

Figure 7.7: Marx voltage waveform in reltron experiments.

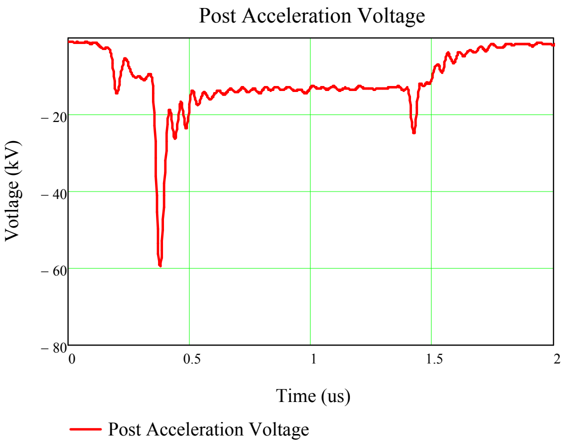

Figure 7.8: Post acceleration gap voltage waveform in reltron experiments.

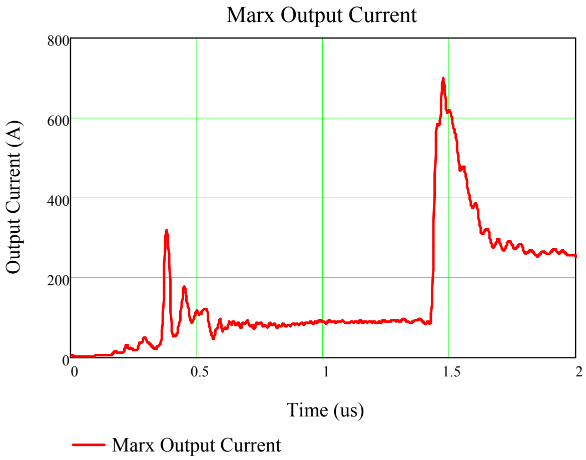

Figure 7.9: Marx current waveform in reltron experiments.

7.1.3 New Grids in the Modulating Cavity

The grids covering the reltron cavity became worn from usage. The original grids were made from micron-thin stainless steel with >95% transparency. Electron etching is used to cut out a grid pattern on the foil. The center portion of the grid is less transparent compared to its outer radius. However, these stainless steel grids are not durable and have to be changed after some 1,000's of shots. A small tear can be seen on the grid closest to the cathode near the outer radius in Figure 7.10.

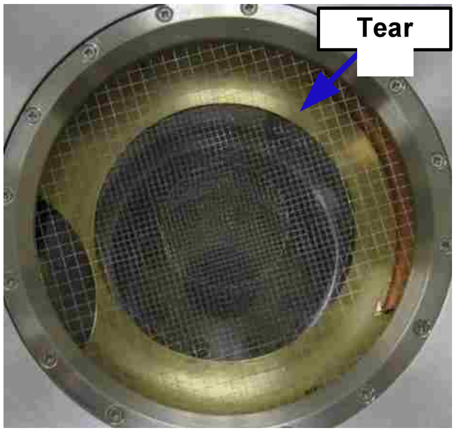

Figure 7.10: Old grids in the reltron modulating cavity.

Figure 7.11: New grids in the reltron modulating cavity.

We replaced the grids with tungsten wire cloth from Unique Wire Weaving Company. These grids have withstood 10,000's of shots to-date without damage. The tungsten cloth has a uniform weave pattern with mesh size of 18 x 18 (wires/inch). The wire diameter is 0.003 inch and the tungsten cloth has a transparency of 89.5%. The reduction in transparency factor can clearly be seen with the new grids in Figure 7.11.

7.2 EXPERIMENTAL DIAGNOSTICS

The power modulator system generates high frequency noise from transient signals such as the Marx trigger voltage or plasma in the gas switches. We reduce this noise by using a 1 GHz oscilloscope to measure signals from the power modulator system. Microwave signals are measured using a 4 GHz oscilloscope with a 10 Gs/s sampling rate (Figure 7.12). All oscilloscopes are commonly grounded to remove ground loops.

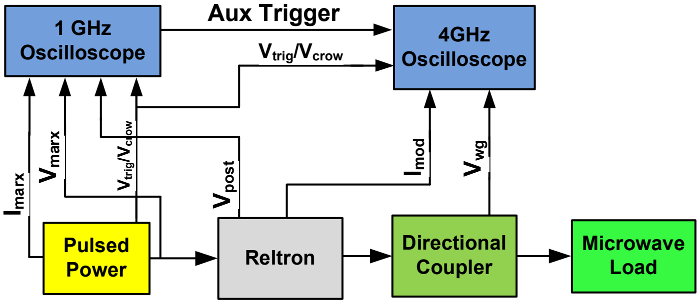

Figure 7.12: Schematic of the experimental diagnostic set-up.

The total current generated by the Marx generator I_{Marx} is measured using a self-integrating Rogowski coil. The Marx voltage V_{Marx} and post-acceleration voltage V_{post} are measured using resistive dividers made of a chain of carbon resistors soldered to a BNC connector. Both the Marx trigger and the crowbar trigger generate a sample pulse when the main pulse is fired. We made a B-dot probe that is inserted into the tank housing of the Marx generator to measure the azimuthal magnetic flux density induced by the modulating beam current. The changing flux induces an electromotive force that is measured across a 50 Ω load on the oscilloscope as I_{mod}. Microwaves are sampled using a WR284 waveguide directional coupler and a waveguide-to-coaxial adapter. Microwaves induce a current source in the adapter that generates a voltage across the internal 50 Ω impedance of the oscilloscope as V_{wg}.

Figure 7.13 shows a block diagram of the vacuum system. A thermocouple (TC) gauge is used to measure pressure in low vacuum (10^{-2} -10^{-4} Torr) and the ion gauge is used to measure pressure in high vacuum (10^{-5} - 10^{-8} Torr).

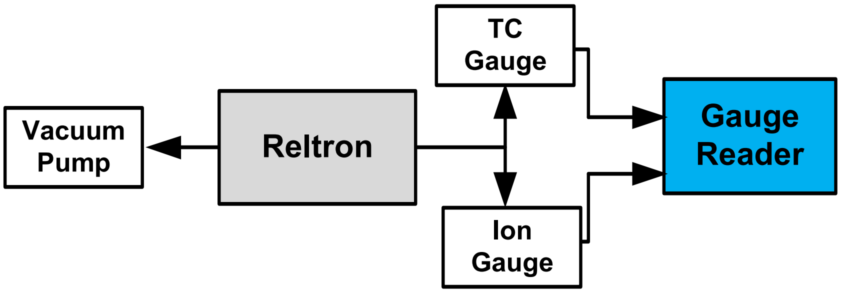

Figure 7.13: Block diagram of the vacuum measurement system.

We are able to pump the reltron down from atmospheric pressure to pressures ~$2.7\text{x}10^{-6}$ Torr. Pulsing the reltron repetitively 10 times at ~0.5 Hz causes the pressure to rise to ~$3.2\text{x}10^{-6}$ Torr.

7.3 EXPERIMENTAL RESULTS

The cold modulating cavity resonates in the π/2 mode at 2.78 GHz when we set the horseshoe dial to 2400 and the idler dial to 3409. The cold extraction cavity resonates at 2.8 GHz with an iris window width of 1.922 inch and cavity length of 3.5 inch. In all our experiments we tune the hot extraction cavity to match the resonant frequency of the hot modulating cavity to maximize microwave power.

7.3.1 Experiments with a 0.4 inch A-K Gap

We use the smallest A-K gap of 0.4 inch to increase the E_z fields on the cathode surface that turns on the velvet cathode. The Marx generator can generate a maximum of 80 kV so the E_z field increases with a narrower gap. The 0.4 inch A-K gap is 1.06 times wider than the 0.375 inch gap of the modulating cavity.

From our circuit model, resistive losses, such as the presence of an electron beam, will lower the resonant frequency of the modulating cavity. We increase the horseshoe dial to 2500, which moves the horseshoe deeper into the cavity and the idler dial to 3445, which brings the idlers closer together. In the extraction cavity we move the back plunger to set the cavity length at 3.1 inch. We set the iris window to 1.73 inch.

Figure 7.14 and Figure 7.15 show the measured Marx voltage and the post-acceleration voltage, respectively. The minimum Marx voltage is -52 kV and the minimum post acceleration voltage is -36 kV.

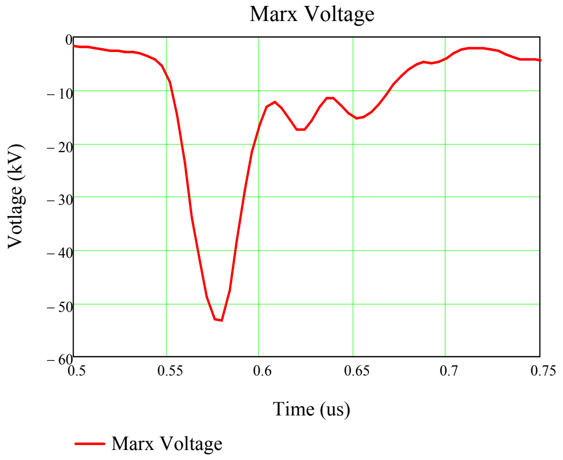

Figure 7.14: Marx voltage waveform obtained in reltron experiments.

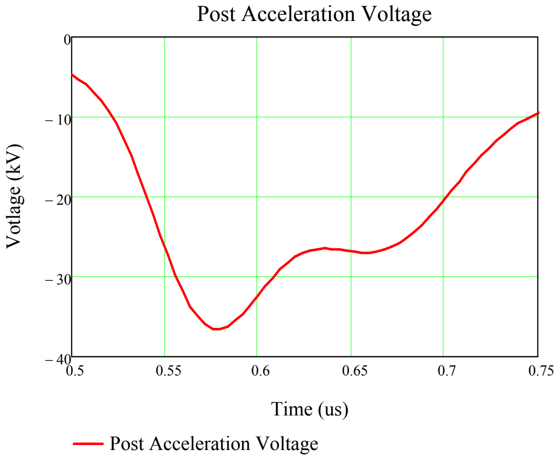

Figure 7.15: Post acceleration gap voltage waveform obtained in reltron experiments.

We infer the A-K gap voltage by taking the difference between the Marx voltage and the post-acceleration gap voltage, as shown in Figure 7.16. Dividing the A-K gap voltage by the A-K gap spacing, we obtain the average electric field inside the gap, which is shown in Figure 7.17.

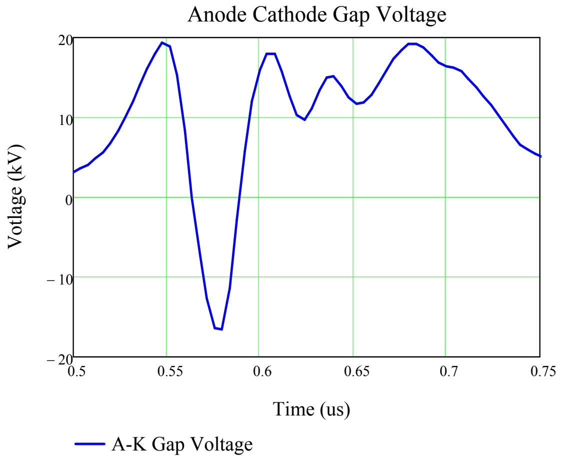

Figure 7.16: A-K gap voltage waveform inferred in reltron experiments.

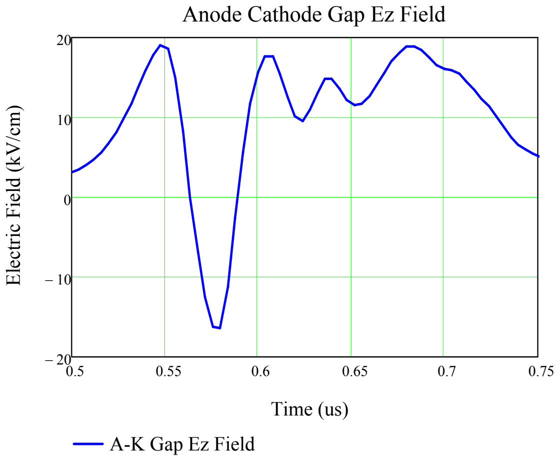

Figure 7.17: Average E_z field in the A-K gap waveform inferred in reltron experiments.

We reach a minimum potential of -16.4 kV with a minimum E_z field of -16.2 kV/cm across the A-K gap.

The total current generated by the Marx generator is shown in Figure 7.18. From the total current, we subtract the current through the water resistor to obtain the beam current, shown in Figure 7.19. Maximum Marx current is 273 A and the maximum beam current is 217 A.

We plot the beam power as a function of time in Figure 7.20. The beam power is calculated by multiplying the A-K gap voltage with the beam current at each instance in time

$$P_{beam}(t) = V_{AK}(t) \times I_{beam}(t)\,. \tag{7.1}$$

The beam power rises sharply to 2.8 MW and falls quickly to negative values because of the voltage reversal in the A-K gap.

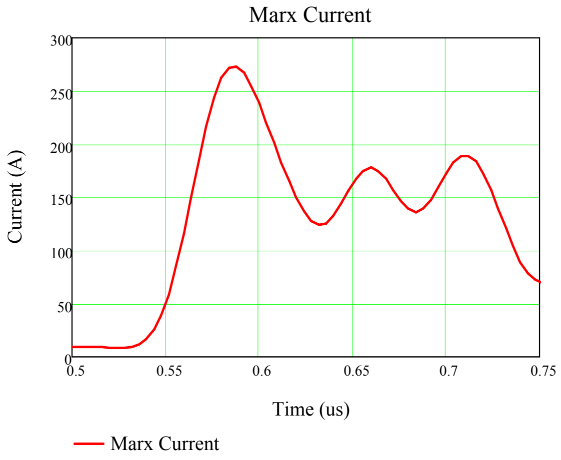

Figure 7.18: Marx current waveform obtained in reltron experiments.

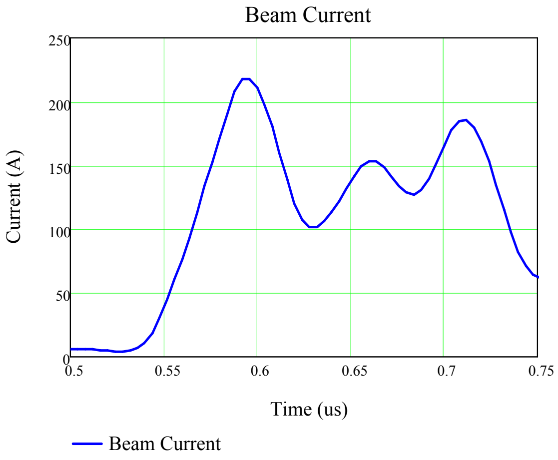

Figure 7.19: Beam current waveform calculated in reltron experiments.

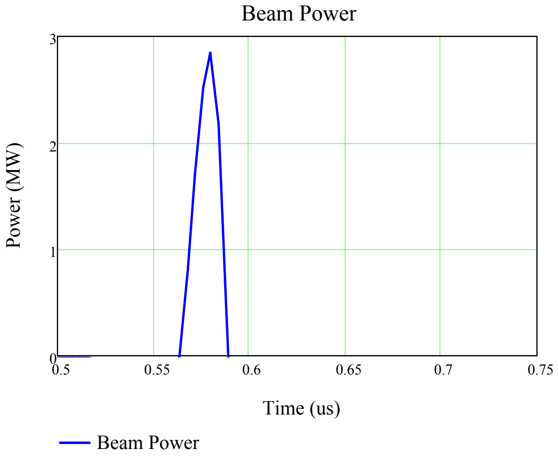

Figure 7.20: Net beam power, as calculated in reltron experiments.

We measure the total voltage generated by the waveguide port of the reltron using a directional coupler, which is shown in Figure 7.21. The beam modulation signal is measured using the B-dot probe and the result is shown in Figure 7.22.

The reltron generates microwaves from 0.55 μs to 0.65 μs for a duration of 100 ns. The microwave power generated by the reltron is plotted in Figure 7.23. Microwave power is calculated by dividing the square of the microwave voltage with the 50 Ω impedance of the oscilloscope

$$P_{wg}(t) = \left[V_{wg}(t)\right]^2 / 50. \tag{7.2}$$

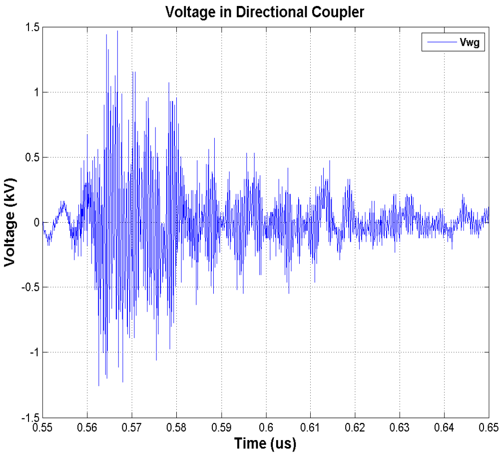

Figure 7.21: Microwave voltage waveform measured in reltron experiments.

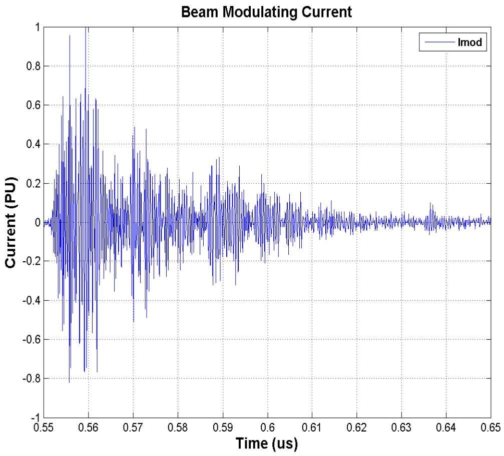

Figure 7.22: Modulating current waveform measured in reltron experiments.

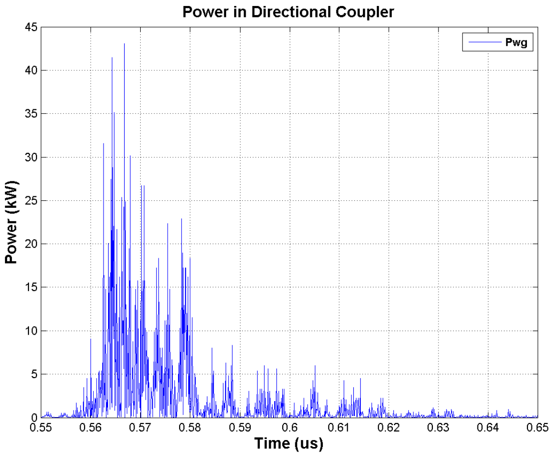

Figure 7.23: Microwave power generated in reltron experiments.

The peak microwave power is 43.09 MW with a FWHM of 18 ns. The FWHM of the microwave power is much shorter than the duration of the microwave voltage because we use the square of the voltage to calculate microwave power.

The frequency spectrum of the microwaves is obtained using the Fast Fourier Transform function in MATLAB 2010a. Figure 7.24 shows the frequency spectrum of the microwave voltage in units of per unit (PU)/GHz and Figure 7.25 show the frequency spectrum of beam modulating current, respectively.

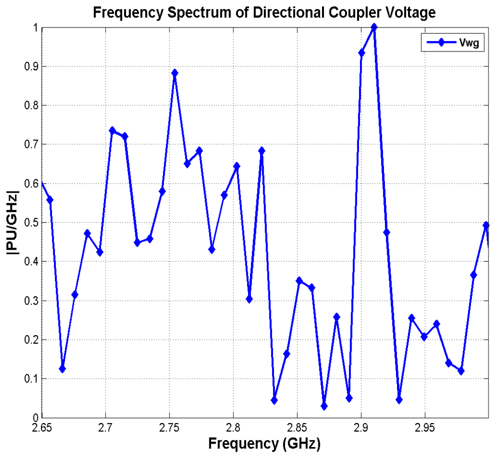

Figure 7.24: Frequency spectrum of microwaves generated in reltron experiments.

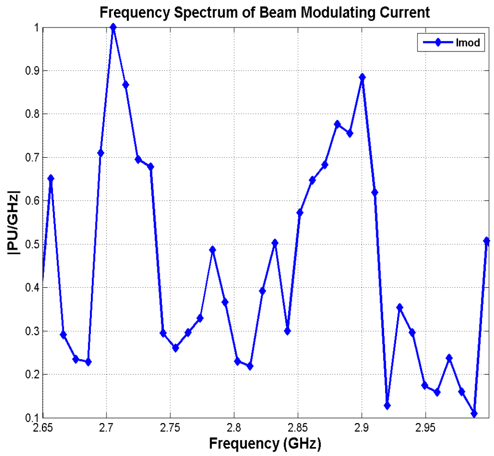

Figure 7.25: Frequency spectrum of modulation current in reltron experiments.

The dominant frequency in the microwave spectrum is 2.91 GHz with the second largest component at 2.754 GHz. The dominant frequency for the current spectrum is 2.705 GHz with the second largest component at 2.9 GHz.

In order to match the resonant frequency of the extraction cavity with the modulating cavity, we widen the iris window to 1.94 inch and shorten the cavity length to 2.878 inch. We move the horseshoe away from the cavity axis by turning the horseshoe dial down to 2400 and move the idlers closer by turning the idler dial up to 3546. Figure 7.26 and Figure 7.27 show the frequency spectrum of the microwave voltage and beam modulating current, respectively.

With a wider window, we down shift the dominant microwave frequency from 2.91 GHz to 2.754 GHz and the second component to 2.705 GHz. The dominant frequency of the modulating current is still 2.705 GHz. Maximum microwave power is 42 kW which is similar to the maximum microwave power generated using the previous modulating cavity and extraction cavity settings.

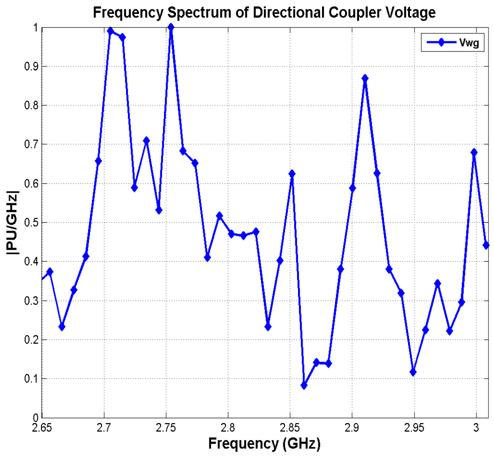

Figure 7.26: Frequency spectrum of microwaves in reltron experiments.

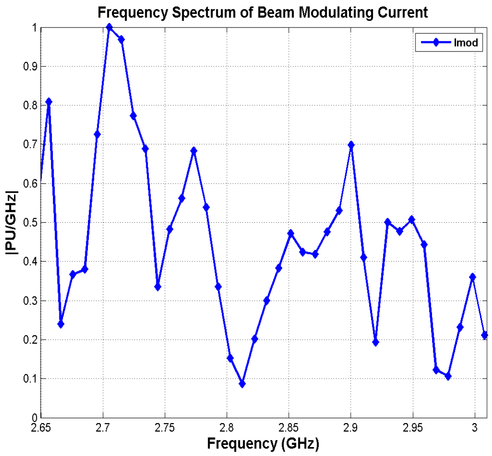

Figure 7.27: Frequency spectrum of modulation current in reltron experiments.

7.3.2 Experiments with a 0.539 inch A-K Gap

We increase the A-K gap to 0.539 inch to increase the voltage hold off. With a higher breakdown threshold we can pulse the reltron at higher voltages. We again set the horseshoe dial back to 2500 and the idler dial to 3445. We set the iris window to 2.01 inch and the cavity length to 2.878 inch. Figure 7.28 and Figure 7.29 show the measured Marx voltage and the post acceleration voltage waveforms, respectively. Minimum Marx voltage is -70.3 kV and the minimum post-acceleration voltage is -41.8 kV.

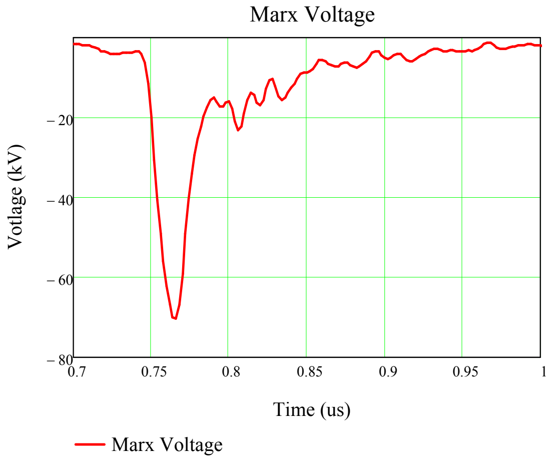

Figure 7.28: Marx voltage waveform obtained in reltron experiments.

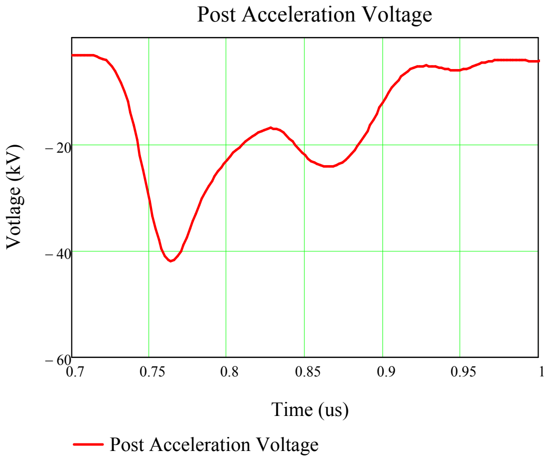

Figure 7.29: Post-acceleration gap voltage waveform obtained in reltron experiments.

The A-K gap voltage reaches -28.7 kV (Figure 7.30) with an average electric field -19.8 kV/cm (Figure 7.31).

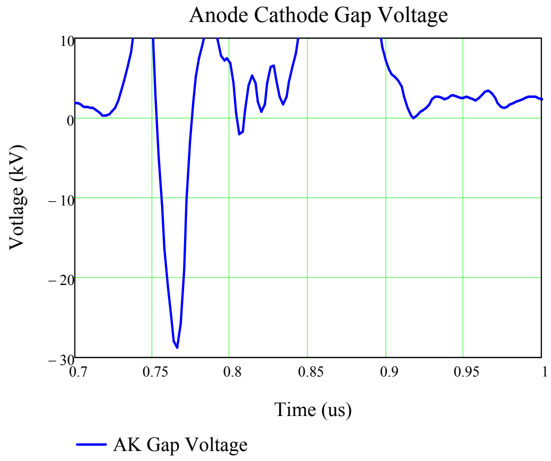

Figure 7.30: A-K gap voltage waveform calculated in reltron experiments.

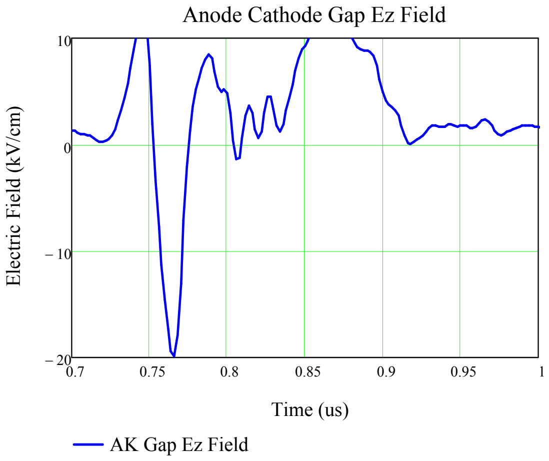

Figure 7.31: Average E_z field in the A-K gap, waveform calculated in reltron experiments.

The total current generated by the Marx generator is shown in Figure 7.32 and the beam current in Figure 7.33. Maximum Marx current is 319 A and maximum beam current is 263 A.

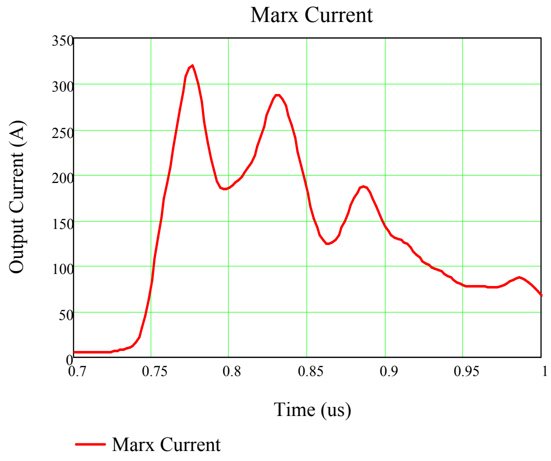

Figure 7.32: Marx current waveform obtained in reltron experiments.

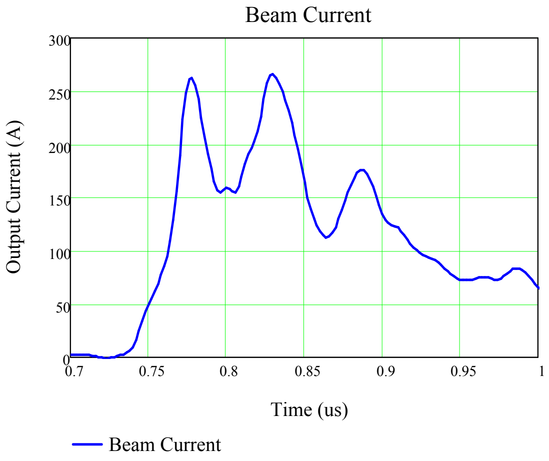

Figure 7.33: Beam current waveform calculated in reltron experiments.

Multiplying the A-K gap voltage with the beam current, we plot the beam power in Figure 7.34. The beam power peaks at 4.03 MW.

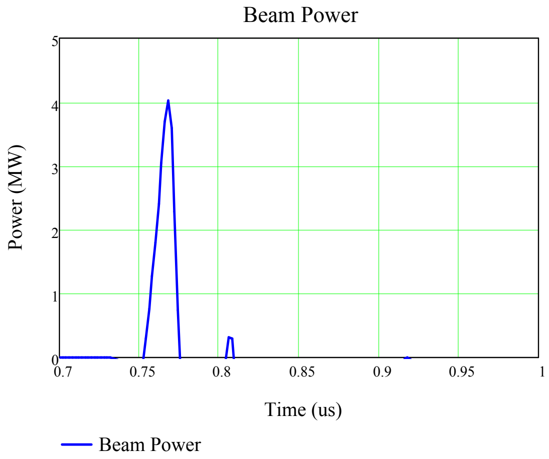

Figure 7.34: Net beam power, as calculated in reltron experiments.

The microwave voltage and the modulating current are plotted in Figure 7.35 and Figure 7.36, respectively.

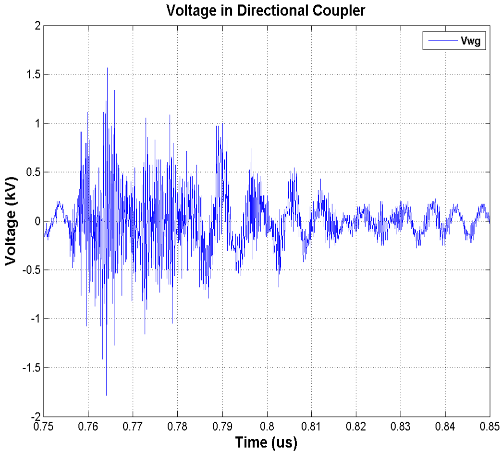

Figure 7.35: Microwave voltage waveform measured in reltron experiments.

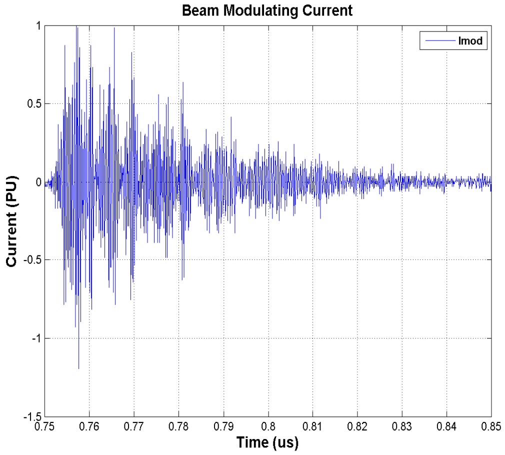

Figure 7.36: Modulating current waveform measured in reltron experiments.

From the microwave voltage, we calculate the microwave power and plot the microwave power waveform in Figure 7.37. Maximum power generated is 63.6 MW.

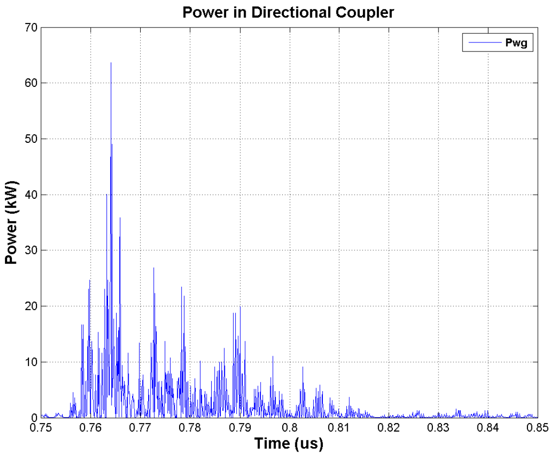

Figure 7.37: Microwave power generated in reltron experiments.

Figure 7.38 and Figure 7.39 show the frequency spectrum of the microwave voltage and beam modulating current, respectively. The dominant microwave frequency is 2.656 GHz with the second largest component at 2.754 GHz. The dominant current frequency is 2.725 GHz with the second largest component at 2.773 GHz.

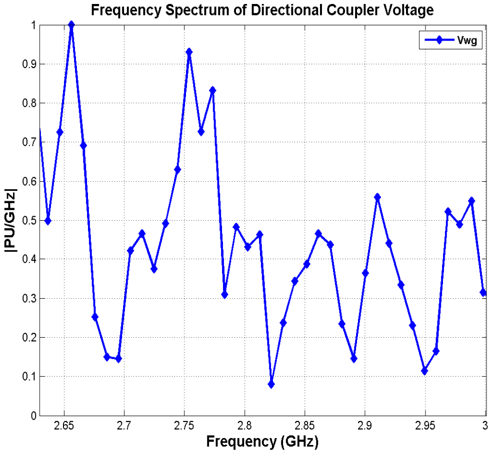

Figure 7.38: Frequency spectrum of generated microwaves in reltron experiments.

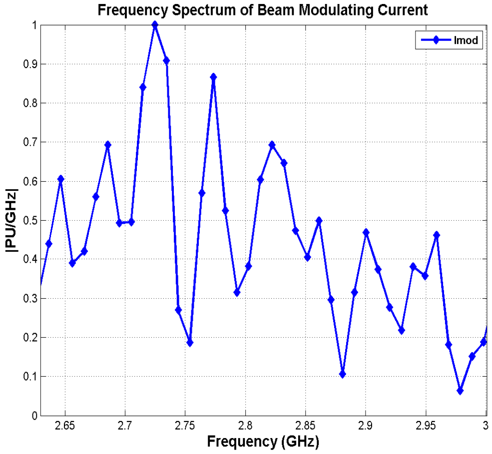

Figure 7.39: Frequency spectrum of modulation current in reltron experiments.

We retune the resonant frequency of the extraction cavity by reducing the cavity window to 1.865 inch and increasing the length to 3.28 inch. The modulating cavity dial settings are kept the same as before. For this shot, we have shifted the dominant microwave frequency upwards to 2.754 GHz (Figure 7.40) while keeping dominant current frequency at 2.734 GHz (Figure 7.41). Maximum beam power decreases to 32.8 MW.

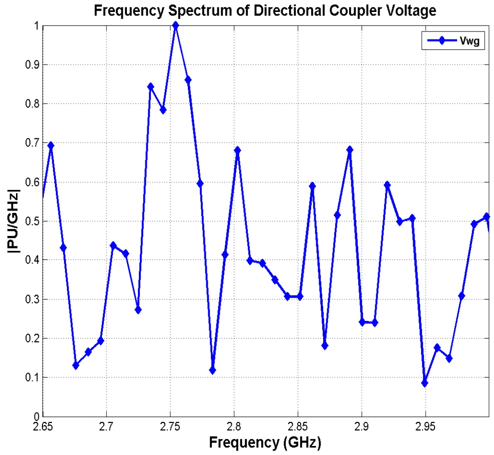

Figure 7.40: Frequency spectrum of generated microwaves in reltron experiments.

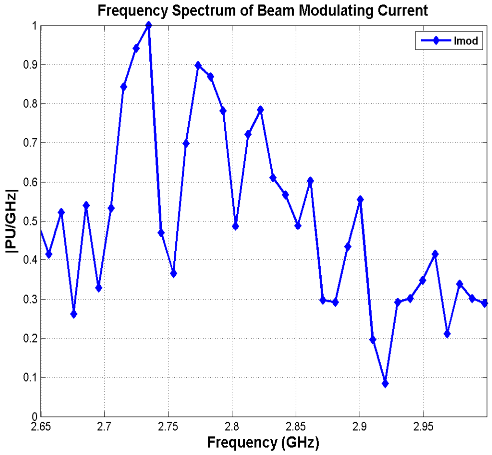

Figure 7.41: Frequency spectrum of modulation current in reltron experiments.

7.3.3 Experiments with a 0.625 inch A-K Gap

In this series we increase the A-K gap to 0.625 inch. We set the horseshoe dial to 2500 and the idler dial to 3545. The extraction cavity length is 2.873 inch and the iris window is 1.84 inch. Figure 7.42 and Figure 7.43 show the measured Marx voltage and the post-acceleration voltage waveforms, respectively.

The Marx voltage reaches its first minimum of -57.8 kV at 0.568 µs, ascends to -18 kV and descends to its second minimum of -28.5 kV at 0.608 µs. After this it decays exponentially. The post-acceleration voltage also shows two dips with less pronounced gradients. These two minima are reflected in the A-K gap voltage (Figure 7.44) and the average electric field (Figure 7.45) waveforms. The A-K gap voltage reaches a minimum of -16.7 kV with an average electric field -10.5 kV/cm at its first minimum and -7.5 kV, -4.7 kV/cm at its second minimum.

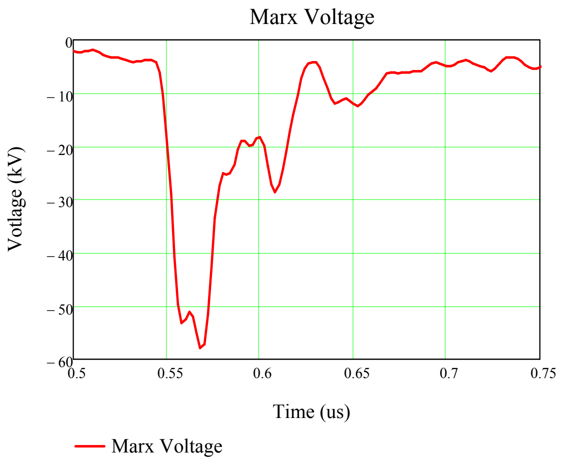

Figure 7.42: Marx voltage waveform.

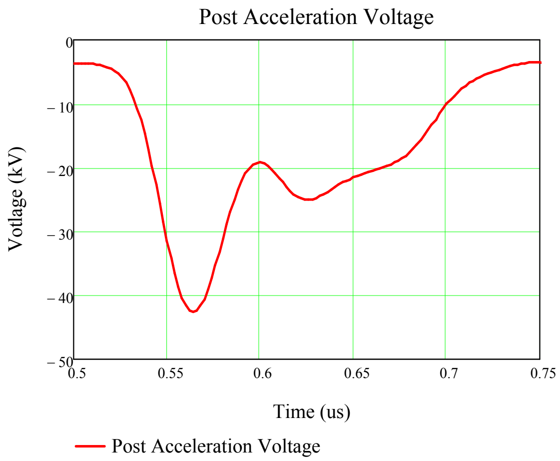

Figure 7.43: Post-acceleration gap voltage waveform.

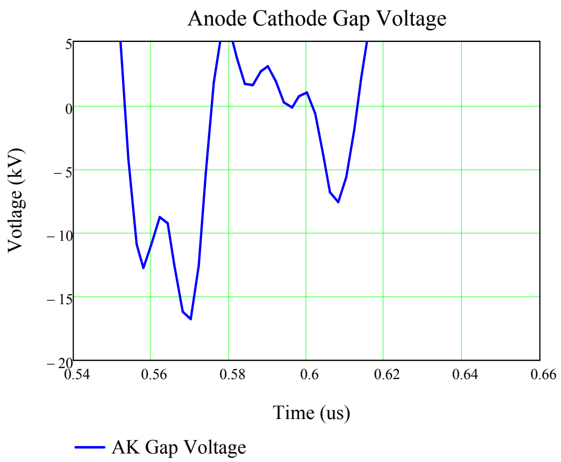

Figure 7.44: Calculated A-K gap voltage waveform.

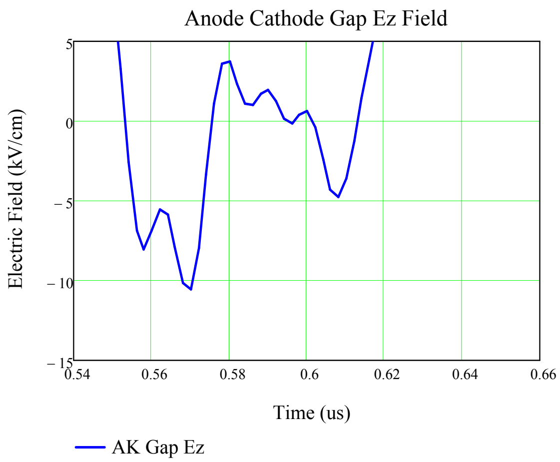

Figure 7.45: Calculated average E_z field in the A-K gap.

The Marx current at its first maximum is 283 A (Figure 7.46) with a beam current of 233 A (Figure 7.47). The Marx current at its second maximum is 277 A with a beam current of 267 A.

The beam power reaches its first peak of 2.67 MW (Figure 7.48), which coincides with the time the A-K gap voltage reaches its first minimum. The beam power reaches its second peak of 1 MW, which coincides with the time the A-K gap voltage reaches its second minimum.

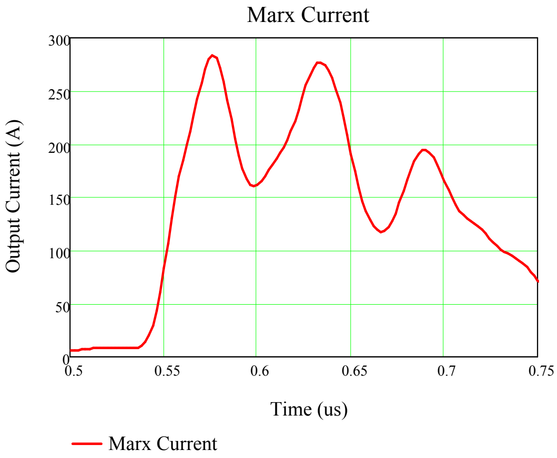

Figure 7.46: Marx current waveform obtained in reltron experiments.

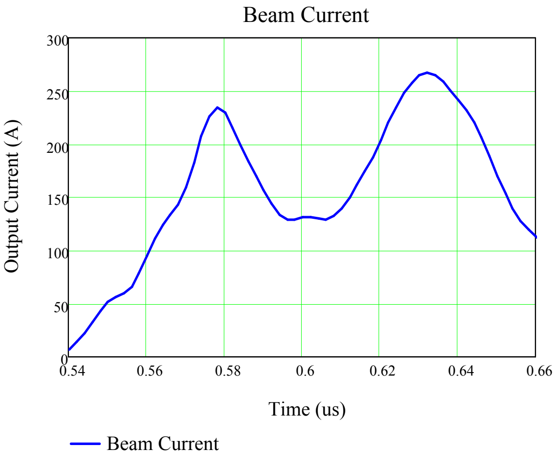

Figure 7.47: Beam current waveform calculated in reltron experiments.

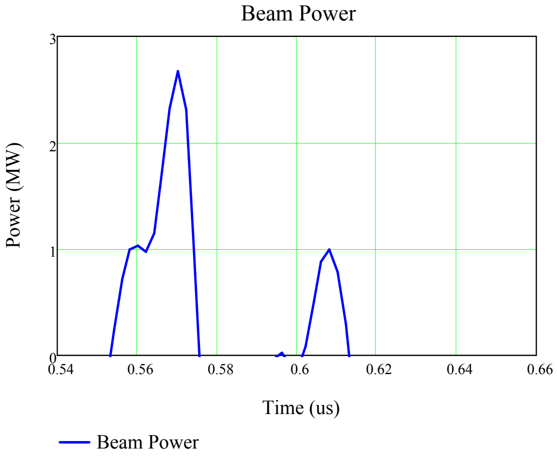

Figure 7.48: Net beam power, as calculated in reltron experiments.

The microwave voltage and the modulating current are plotted in Figure 7.49 and Figure 7.50, respectively. We see a few cycles of low frequency oscillations that start after the beam power becomes negative. Even though the beam power peaks a second time, we do not see a second surge in microwave power.

Microwave power reaches its maximum of 116 MW at 0.563 μs (Figure 7.51) just as the beam power reaches its first peak.

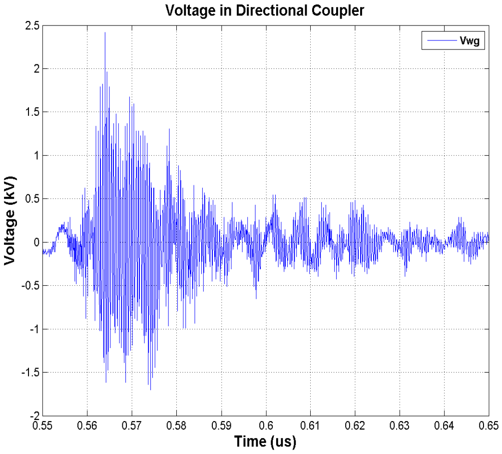

Figure 7.49: Microwave voltage waveform measured using the directional coupler.

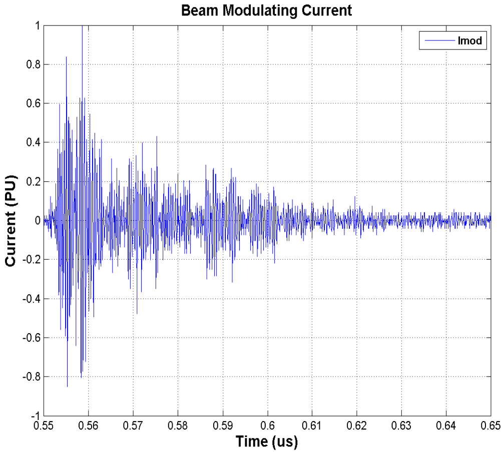

Figure 7.50: Modulating current waveform.

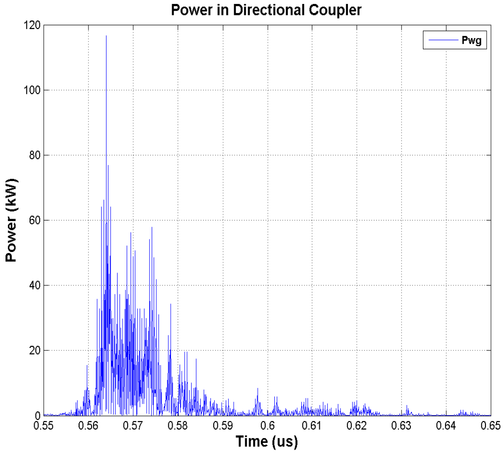

Figure 7.51: Microwave power waveform.

Figure 7.52 and Figure 7.53 show the frequency spectrum of the microwave voltage and beam modulating current, respectively.

The microwave spectrum reveals two dominant frequencies at 2.91 GHz and 2.754 GHz. The dominant frequency in the modulating current is 2.656 GHz. We perform a time frequency analysis of the microwave voltage using the spectrogram function in MATLAB 2010. Spectrogram computes the short time Fourier transform of the signal within a specified Hamming window. Figure 7.54 is a time frequency plot of the microwave signal. The time axis is the time after the start of microwave generation at

0.55 μs. Both the 2.91 GHz and 2.754 GHz frequency components are found at the start of microwave generation. The 2.91 GHz component lasts for 65 ns while the 2.754 GHz chirps upwards in frequency after 35 ns.

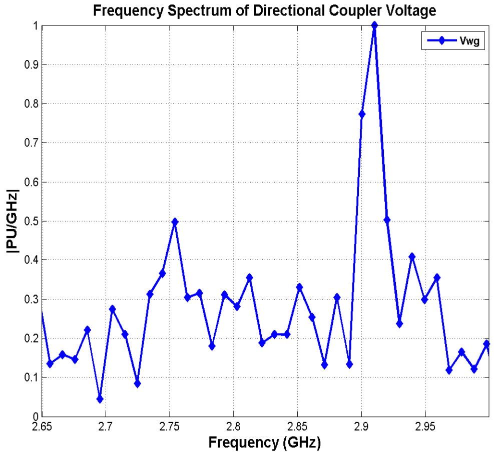

Figure 7.52: Spectrum of microwave frequency

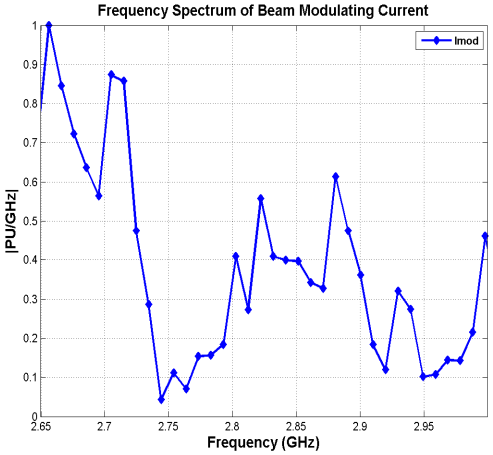

Figure 7.53: Spectrum of modulating current

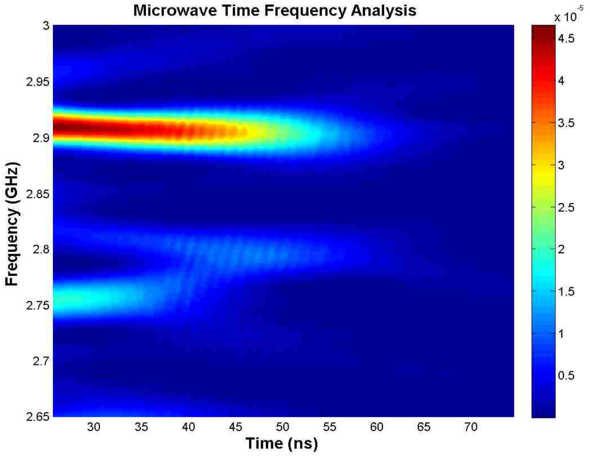

Figure 7.54: Contour plot of microwave time frequency analysis.

We retain the settings on the extraction cavity and turn down the horseshoe dial to 2351 and we turn down the coupling dial to 3443. The Marx voltage again shows (Figure 7.55) two major dips of -76.5 kV at 0.278 μs and of -35.4 kV at 0.316 μs. The post-acceleration voltage shows similar dips with less pronounced gradients (Figure 7.56). Both the Marx and post acceleration voltage decay exponentially after the second dip.

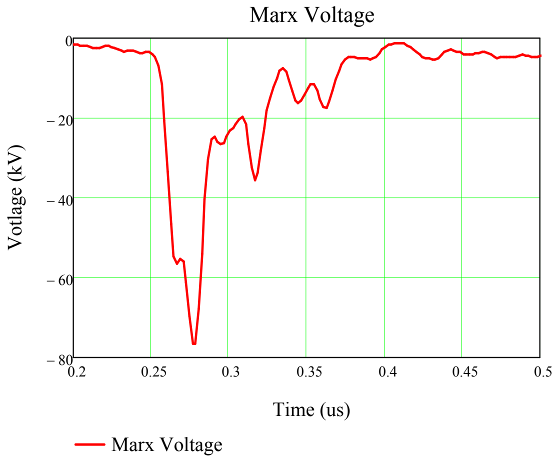

Figure 7.55: Marx voltage waveform obtained in reltron experiments.

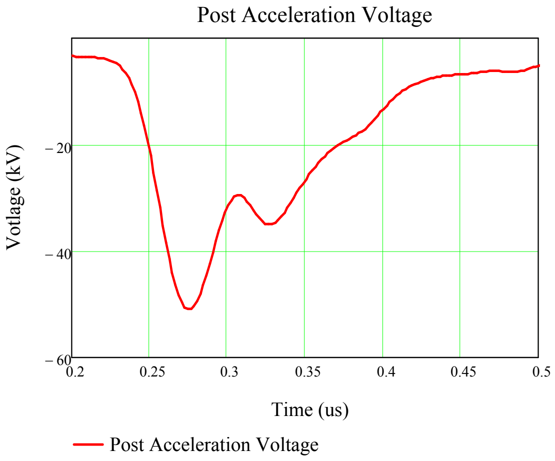

Figure 7.56: Post-acceleration gap voltage waveform obtained in reltron experiments.

The A-K gap potential (Figure 7.57) drops to -26 kV and -3.2 kV with average E_z field (Figure 7.58) declining to -16.4 kV/cm and -2 kV/cm, respectively.

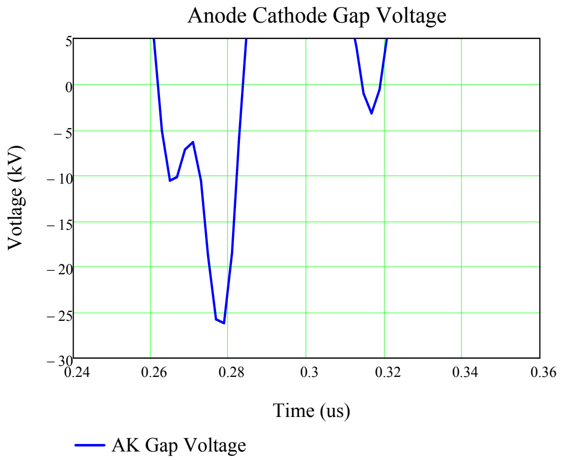

Figure 7.57: A-K gap voltage waveform calculated in reltron experiments.

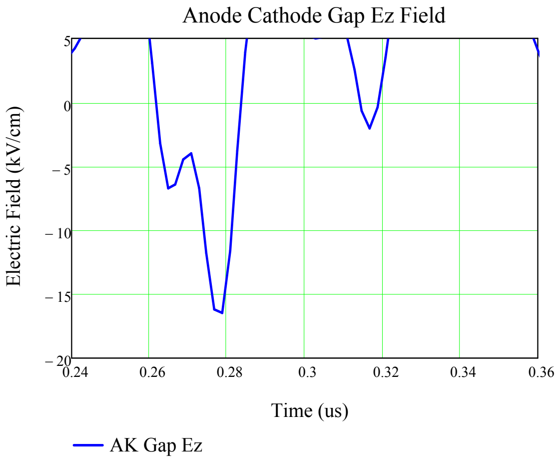

Figure 7.58: Average E_z field in the A-K gap, calculated in reltron experiments.

Just after the Marx voltage reaches its first minimum, the Marx current rises to 264 A (Figure 7.59) and the beam current to 213 A (Figure 7.60). After the Marx reaches its second minimum, the Marx current rises to 242 A and the beam current to 242 A.

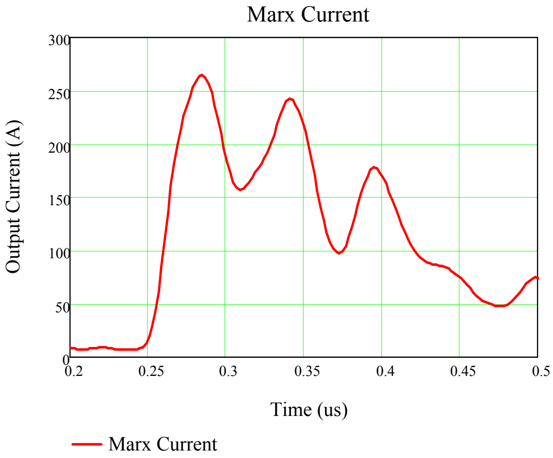

Figure 7.59: Marx current waveform obtained in reltron experiments.

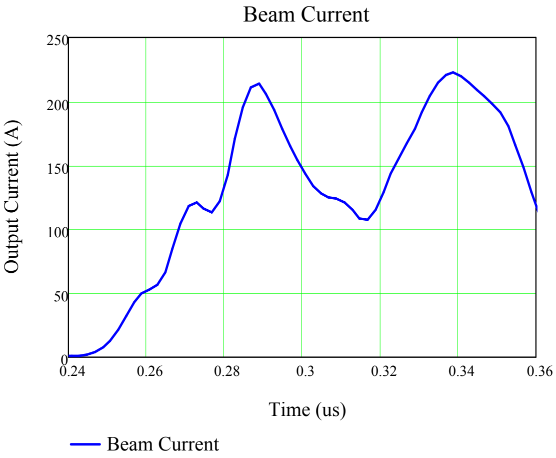

Figure 7.60: Beam current waveform calculated in reltron experiments.

The beam power reaches a maximum of 3.18 MW (Figure 7.61) when the Marx voltage reaches its first minimum before declining rapidly to negative values. It reaches a low peak of 0.348 MW at the second minimum and declines rapidly to negative values.

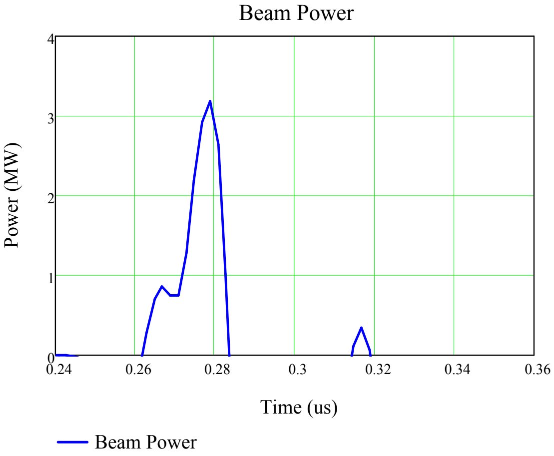

Figure 7.61: Net beam power, as calculated in reltron experiments.

During the first minimum of the Marx voltage, microwave power reaches its maximum of 60.5 MW at 0.263 μs (Figure 7.62).

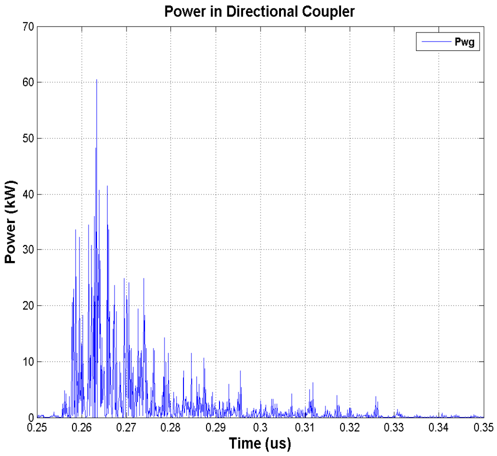

Figure 7.62: Microwave power generated in reltron experiments.

Figure 7.63 and Figure 7.64 show the frequency spectrum of the microwave voltage and beam modulating current, respectively.

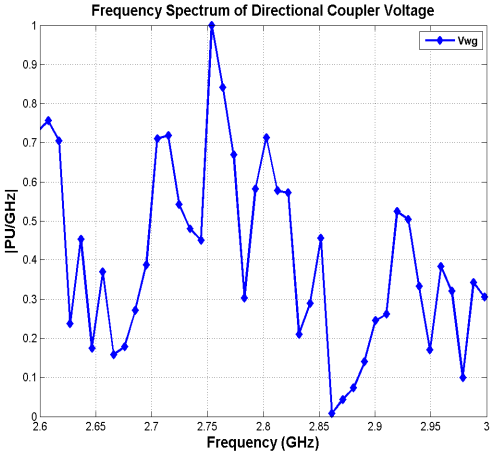

Figure 7.63: Frequency spectrum of generated microwaves in reltron experiments.

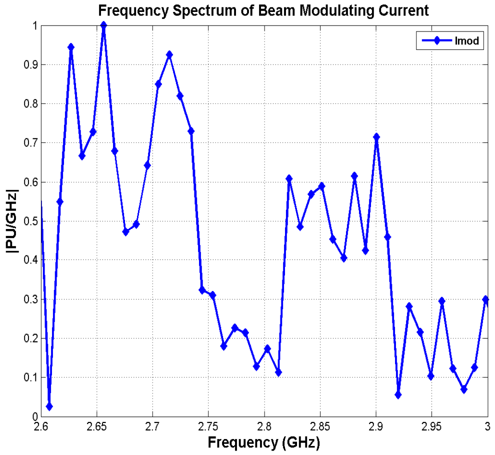

Figure 7.64: Frequency spectrum of modulation current in reltron experiments.

The dominant frequency in the microwave spectrum is 2.754 GHz and the dominant frequency in the current spectrum is 2.65 GHz. Figure 7.65 is a time frequency plot of the microwave signal. The time axis is the time after the start of microwave generation at 0.25 μs. All three frequency components, 2.754 GHz, 2.715 GHz, and 2.808 GHz are excited at the start of microwave generation. The dominant component, 2.754 GHz, persists for the longest duration and ceases after 40 ns.

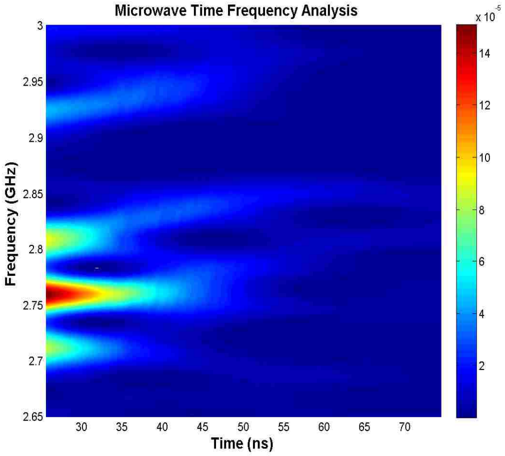

Figure 7.65: Contour plot of microwave time frequency analysis.

7.4 SUMMARY OF EXPERIMENTAL RESULTS AND CONCLUSIONS FROM EXPERIMENTS

We tabulate the peak microwave power and frequency for A-K gaps of 0.4 inch – 0.75 inch in Figure 7.66. The data points are sampled from numerous single shot experiments conducted on the reltron.

Maximum microwave power generated by the reltron is 116 MW at 2.9 GHz. Even though we can tune the modulating cavity to resonate with the extraction cavity, the cavities do saturate because beam propagation is disrupted. As the cavities do not saturate, the reltron does not generate microwaves with power level in the single digit megawatt range.

In all experiments we always see a reversal in the polarity of the A-K gap potential and the polarity of the E_z field prior to the exponential decay of microwave power. We postulate that the reversal is due to arcing across the A-K gap. Arcing disrupts the continuous beam before it enters the modulating cavity, reducing the quality of the beam that enters the modulating cavity. For narrow gaps of 0.4 inch and 0.539 inch, arcing results in the Marx voltage decaying exponentially. For the wider 0.625 inch gap, the Marx voltage does recover to a smaller magnitude, as seen in the second minimum, before decaying exponentially. The reversal in polarity results in the beam power declining rapidly from its peak to negative values. Without sufficient beam power to sustain the EM fields in the modulating cavity, the reltron stops generating microwaves.

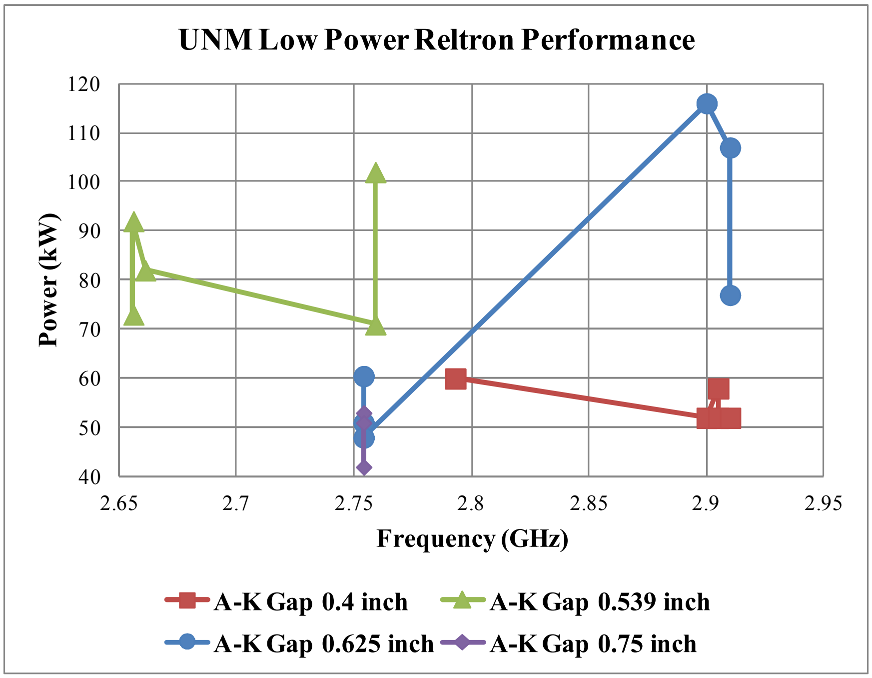

Figure 7.66: Microwave power and frequency of the UNM reltron.

The velvet cathode emits electrons via explosive emission [28]. Surface flashover generates a cold dense plasma along the lengths of the velvet tufts and the electrons are extracted from the plasma by electric fields. Our A-K gap voltage and E_z field are too low to effectively sustain the plasma and allow electrons to be continuously drawn from the plasma. Our data show the average E_z field does not exceed -20 kV/cm for all A-K gaps. Also, the slow rise time of the Marx generator results in the flashover burning the fibers rather than causing the fibers to uniformly generate plasma.

Figure 7.67 shows the Marx voltage and post-acceleration voltage, and Figure 7.68 shows the Marx current into the resistive divider without the reltron. The Marx generator erects from 0 to -50 kV with a rise time of 132 ns.

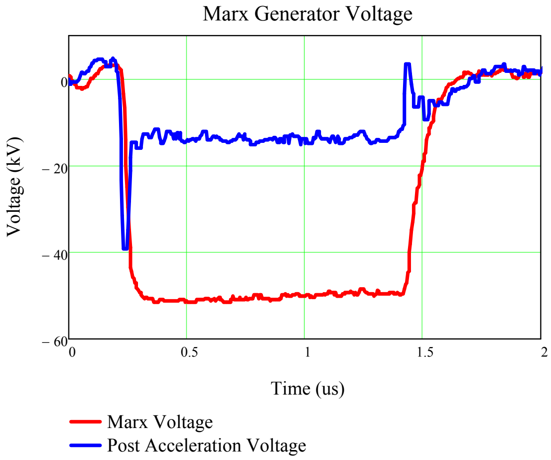

Figure 7.67: Marx generator voltage and post acceleration voltage.

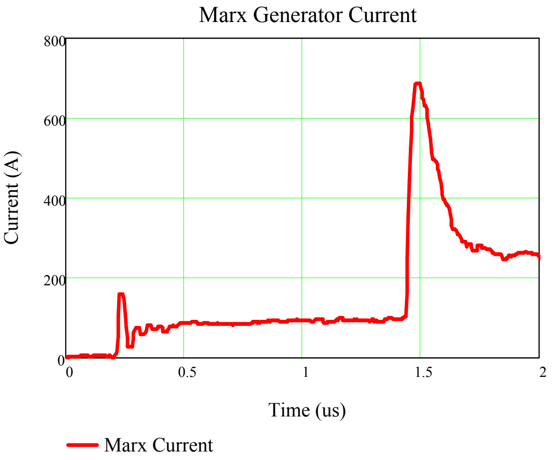

Figure 7.68: Marx generator current.

If we neglect the reltron impedance, the Marx generator will give an A-K gap potential of -35 kV in 132 ns. We can reach average E_z fields of -30 kV/cm or greater for our 0.4 inch A-K gap. For larger A-K gaps, we need only to charge the capacitors to higher voltages. We believe arcing prevents the A-K gap from reaching -30 kV/cm, thus preventing the velvet cathode from turning on effectively. The cathode generates an electron beam for a short duration of ~100 ns until arcing prevents the beam from propagating through the modulating cavity.

CHAPTER 8: CONCLUSIONS AND RECOMMENDATIONS FOR FUTURE WORK

8.1 CONCLUSIONS

From our single particle analysis, we calculate the minimum beam potential for the modulating cavity to self excite is 13.1 kV. In experiments, we see the start of significant beam modulation when the cathode potential rises to ~20 kV. Placing a short drift tube between the gaps (4 grids SCO) causes the electrons to lose a larger portion of their K.E. to the modulating cavity.

MAGIC simulations and cold cavity measurements confirm the π/2 mode to be at 2.78 GHz. Using the resonant mode, we calculate the resonant frequency of the main cavity and coupling cavity using a circuit model. A transmission line model of the single and dual extraction cavity is used to give the initial physical parameters of the extraction cavity. We simulate the extraction cavity in HFSS to obtain the actual resonant frequency.

The calculated electric fields in the A-K gap are greater than the fields simulated by CST. However, the fields are within the same order of magnitude. In the post-acceleration gap, the calculated electric fields are an order of magnitude greater than the simulated fields. The higher fields are due to the stair stepping approximation used in the model to account for the slope of the metal electrodes. In order to keep the maximum electric field on the metal electrodes to 150 kV/cm, we need an A-K gap distance of 0.78 inch. With the A-K potential at 40 kV, this gives an average E_z field of 20 kV/cm on the velvet surface.

MAGIC simulations show the UNM reltron is able to generate microwave power in the single digit megawatt range for Marx voltages of 80 kV or higher. Microwave frequency is 2.74 GHz - 2.75 GHz and saturates after 60 ns for a voltage pulse with 1 ns rise time. Only one dominant mode is observed throughout the 125 ns simulation and microwave power remains constant after saturation. Phase space plots show some electrons do get reflected back from the modulating cavity and impact the cathode.

8.2 RECOMMENDATIONS FOR FUTURE WORK

The UNM low power reltron suffers from arcing across the A-K gap. We propose using cesium iodide (CsI) coated carbon fiber cathodes [40] instead of velvet cathodes to mitigate the problem of arcing. CsI carbon fiber cathodes turn at a much lower electric field threshold, thus limiting the effects of explosive emission and plasma formation in the A-K gap. In addition they produce little outgassing, thus maintaining the integrity of the vacuum in the gap region. The limited plasma generation and little outgassing will reduce the probability of arcing. In addition, we can insert a peaking switch between the Marx generator and the reltron to sharpen the rise time of the voltage pulse. A fast rise time will assist the turn on process of the cathode material.

The maximum voltage that the Marx generator can produce is ~80 kV. This voltage limit is due to self-breakdown of the crowbar switch. We can replace the crowbar switch with one that has a higher self-breakdown threshold to increase the maximum voltage of the Marx generator.

For the high power reltron tubes, we designed a self-excited dual cavity reltron [41]. We added a second cavity to increase beam modulation, allowing tighter beam bunches to be formed. We designed the dual cavity reltron using relativistic single particle analysis and MAGIC PIC simulations. From MAGIC PIC simulations we show that the microwave power generated by the dual cavity reltron is greater than the beam power of the A-K gap.

We also have a design for a high power reltron capable of generating dual modes concurrently [42]. We designed a modulating cavity with a beam that can excite both TM_{010} and TM_{110} modes and tune the extraction cavity to match both modes. By extracting two modes, we are able to generate microwave power greater than the power generated by individual modes.

REFERENCES

[1] R. B. Miller, W. F. McCullough, K. T. Lancaster, and C. A. Muehlenweg, “Super-reltron theory and experiments,” IEEE Trans. Plasma Sci., vol. 20, pp. 332-343 (1992).

[2] R. B. Miller, W. F. McCullough, K. W. Habiger, and J. R. Clifford, “Super-reltron progress”, IEEE Trans. Plasma Sci, vol. 22, pp.701-705 (1994).

[3] R. B. Miller, “Repetitive pulse operation of reltron tubes,” *Proceedings SPIE*, vol. 3158, Intense Microwave Pulses V (1997).

[4] R. B. Miller, K. W. Habiger, W. R. Beggs, Jr., and J. R. Clifford, “Advances in super-reltron source development,” *Proceedings SPIE*, vol. 2557, Intense Microwave Pulses III (1995).

[5] R. B. Miller, “Pulse shortening in high peak power reltron tubes,” *Proceedings SPIE*, vol. 2843, Intense Microwave Pulses IV (1996).

[6] P. K. Tien, and L. M. Field, “Space-charge waves in an accelerated electron stream for amplification of microwave signals,” Proc. I.R.E. vol. 40, pp. 688-695 (1952).

[7] F. B. Llewellyn, and L. C. Peterson, “Vacuum-tube networks,” Proc. I.R.E. vol. 32, pp. 144-166 (1944).

[8] J. Gardelle, “The arletron: a new buncher for high-repetition-rate HPM operation,” IEEE Trans. Plasma Sci, vol. 37, issue 7, pp. 1225-1232 (2009).

[9] B. Goplen, L. Ludeking, D. Smith, and G. Warren, “User-configurable MAGIC for electromagnetic pic calculations,” Comp. Phys. Comm., vol. 87, 54-86 (1995).

[10] E. B. Abubakirov and A. V. Savelyev, “Relativistic microwave devices with post acceleration of an electron beam in the interaction space,” Tech. Phys., vol. 45, pp. 883-886 (2000).

[11] S. Soh, E. Schamiloglu, J. Gaudet, and R.L. Terry, “Analytic model and experimental study of the UNM educational reltron's pulsed power system,” *Proc. 2009 IEEE Int’l Pulsed Power Conf.* (Washington, DC, June 2009), pp. 768-773.

[12] S. Soh, E. Schamiloglu, and R. B. Miller, “Circuit model of UNM educational reltron cavity,” *Proceedings 2010 Power Modulator Conf.* (Atlanta, GA, May 2010), pp. 233-237.

[13] J. Marcum, “Interchange of energy between an electron beam and an oscillating electric field,” J. Appl. Phys., vol. 17, pp. 4-11 (1946).

[14] R. Courant, K. Friedrichs, H. Lewy, “On the partial difference equations of mathematical physics,” Mathematische Annalen, vol. 100, pp. 32–74 (1928).

[15] R.B. Miller, “Pulse shortening in high-peak-power reltron tubes,” IEEE. Trans. Plasma Sci., vol. 26, pp. 340-347 (1998).

[16] B. M. Marder, M.C. Clark, L.D. Bacon, J.M. Hoffman, R.W. Lemke, and P.D. Coleman, “The split-cavity oscillator: a high-power e-beam modulator and microwave source,” Trans. Plasma Sci., vol. 20, pp. 312–331 (1992).

[17] E. Schamiloglu, and S. Soh, “Reltron evolution from the split-cavity oscillator (SCO),” Internal Report, Department of Electrical and Computer Engineering, University of New Mexico, 2010.

[18] E. A. Knapp, B. C. Knapp and J. M. Potter, “Standing wave high energy linear accelerator structures,” Rev. Sci. Instrum., vol. 39, pp. 979–991 (1968).

[19] L. Ludeking, D. Smithe, M. Bettenhausen, and S. Hayes, *MAGIC user’s manual,* (Mission Research Corp., Newington, VA, MRC/WDC-R-445, 1999).

[20] D.E. Nagle, E.A. Knapp, and B.C. Knapp, “Coupled resonator model for standing wave accelerator tanks,” Rev. Sci. Instrum., vol. 38, pp. 1583-1587 (1967).

[21] R. B. Miller, *Electronic Irradiation of Foods: An Introduction to the Technology*, (Springer, New York, NY, 2005).

[22] D.L. Webster, “Cathode-ray bunching,” J. Appl. Phys. vol. 10, pp. 501-508 (1939).

[23] W. T. Roybal, *Investigation Of The Effects Of Returning Electrons On Klystron Performance* (Ph.D. Dissertation, University of New Mexico, Albuquerque, NM, 2005).

[24] D. M. Pozar, *Microwave Engineering 3rd Ed.* (Wiley, Hoboken, NJ, 2004).

[25] H. A. Atwater, *Introduction To Microwave Theory* (McGraw-Hill, New York, NY, 1981).

[26] B. N. Breizman (Brejzman) and D. D. Ryutov, “Powerful relativistic electron beams in a. plasma and in a vacuum (theory),” Nucl. Fusion, vol. 14, pp. 873-907 (1974).

[27] C. A. Balanis, *Advanced Engineering Electromagnetics*, (John Wiley & Sons, New York, NY, 1989).

[28] R. B. Miller, “Mechanism of explosive electron emission for dielectric fiber (velvet) cathodes,” J. Appl. Phys., vol. 84, pp. 3880-3889 (1998).

[29] J. D. Cockcroft, “The effect of curved boundaries on the distribution of electrical stress round conductors,” J. IEE, vol. 66, pp. 385-409 (1928).

[30] J. W. Boag, “The design of the electric field in a Van de Graaff generator,” Proceedings IEE, vol. 100, pp. 63-82 (1953).

[31] C. K. Allen, S. K. Guharay, and M. Reiser, “Solution of Laplace’s equation by the method of moments with Applications to Charged Particle Transport,” *Computational Accelerator Physics*, AIP Conference Proceedings, vol. 297 (1993).

[32] R. V. Latham (Series Editor), *High Voltage Vacuum Insulation: Basic Concepts and Technological Practice* (Academic Press, New York, NY, 1995).

[33] K. Yee, “Numerical solution of initial boundary value problems involving Maxwell's equation in isotropic media,” IEEE Trans. Antennas and Propagat., vol. 14, pp. 302-307 (1966).

[34] J. P. Boris, “Relativistic plasma simulation-optimization of a hybrid code,” *Proc. Fourth Conf. on Numerical Simulation of Plasmas* (Naval Research Laboratory, Washington. DC. 1970), pp. 3-67.

[35] J. A. Halbleib and R.P. Kensek, “ITS: The integrated TIGER series of electron/photon transport codes - Version 3.0”, IEEE Trans. Nuclear Sci. vol. 39, pp. 1025-1030 (1992).

[36] B. C. Franke, R.P. Kensek, and T. W. Laub, “ITS Version 5.0: The Integrated TIGER Series of Coupled Electron/Photon Monte Carlo Transport Codes with CAD Geometry,” Sandia National Laboratories Report, SAND2004-5172 (2005).

[37] S. Humphries, *Charged Particle Beams*, (John Wiley and Sons, New York, NY, 1990).

[38] L. S. Bogdankevich and A. A. Rukhadze, “Stability of relativistic electron beams in a plasma and the problem of critical currents,” Sov. Phys. Uspekhi, vol. 14, pp. 163–179 (1971).

[39] J. A. Nation and M. Read, “Limiting currents in unneutralized relativistic electron beams,” Appl. Phys. Lett., vol 23, pp. 426-428 (1973).

[40] D. A. Shiffler, M. J. LaCour, M. D. Sena, M. D. Mitchell, M. D. Haworth, K. J. Hendricks, and T. A. Spencer, “Comparison of carbon fiber and cesium iodide-coated carbon fiber cathodes,” IEEE Trans. Plasma Sci, vol. 28, pp. 445-451 (2000).

[41] S. Soh, R. B. Miller, and E. Schamiloglu, “Dual cavity reltron,” *Proc. 2011 IEEE Int’l Pulsed Power Conf.* (Chicago, IL, June 2011) in press.

[42] S. Soh, R. B. Miller, and E. Schamiloglu, “Dual mode reltron,” (in preparation for publication).

[43] L. Tonks and I. Langmuir, “Oscillations in ionized gases,” Phys. Rev., vol. 33, pp. 195 – 210 (1929).

[44] W. C. Hahn, “Small signal theory of velocity modulated electron beams,” General Electric Review, vol. 42, pp. 258-270 (1939).

[45] W. C. Hahn, “Wave energy and transconductance of velocity-modulated electron beams,” General Electric Review, vol. 42, pp. 497-502 (1939).

[46] S. Ramo, “Space charge and field waves in an electron beam,” Phys. Rev., vol. 56, pp. 276-283 (1939).

[47] S. Ramo, “The electronic wave theory of velocity modulated tubes,” I.R.E., vol. 27, pp. 757-763 (1939).

[48] J. D. Lawson, *The Physics of Charged-particle Beams* (Oxford University Press, New York, NY, 1977).

APPENDIX A: DISPERSION RELATION OF SPACE CHARGE WAVES

Throughout this Appendix, the variables are assumed to have small sinusoidal perturbation from the steady state. For example, electron velocity in the z direction will have a steady and perturbed component $v_z(z,t) = v_0(z) + v_1(z)e^{i(\omega t - kz)}$.

A.1 DISPERSION RELATION OF UNBOUNDED SPACE CHARGE WAVES IN A RELATIVISTIC ELECTRON BEAM

Tonks and Langmuir [43] have shown that electrons with zero drift velocity will oscillate with frequency proportional to the square root of their density. This is termed the plasma frequency and its relativistic form is given by

$$\omega_p^2 = \frac{q^2 n_0}{\gamma_0 \varepsilon_0 m_e} \tag{A.1}$$

where γ_0 is the relativistic correction factor given by

$$\gamma_0 = \frac{1}{\sqrt{1-\left(\frac{v_0}{c_0}\right)^2}} = \frac{1}{\sqrt{1-\beta_0{}^2}} \quad . \tag{A.2}$$

When electrons flow with drift velocity v_0, space charge disturbances propagate along the column of electrons. The space charge forces modulate the electron velocity causing the electrons to oscillate in phase. An EM wave is excited because of the beam and this wave is termed a space charge wave.

Hahn [44] is the first to publish on the theory of space charge waves inside a beam. In his paper, he derived the dispersion relation for an axisymmetric beam of uniform density inside a waveguide. The cyclotron resonance ω_H due to the external magnetic field is included in the dispersion relation. He simplified the mathematically complicated dispersion relation by taking the limits $\omega_H \rightarrow \infty$ and $\omega_H \rightarrow 0$. He then obtained dispersion relations in the two limits. In his next paper, Hahn [45] analyzed the energy flow in the waves and the resulting current modulation of the beam as it traversed a gap.

Building upon Hahn's analysis, Ramo [46] published a general dispersion relation in the non-axisymmetric case. He considered the case where electrons only have an axial velocity (high magnetic field) and the case where electrons have velocity components in all direction (no magnetic field). Ramo [47] also demonstrated the use of space charge wave theory in designing electron tubes.

We will now derive the dispersion relation of the space charge wave for a beam of particles with charge q_e drifting in the z direction. The three sets of equations needed are Poisson's equation, the continuity equation and the equation of motion

Poisson Equation

$$\frac{\partial E_1}{\partial z} = \frac{q_e n_1}{\varepsilon_0},$$

$$\tilde{E}_1 = \frac{i q_e \tilde{n}_1}{k \varepsilon_0}. \tag{A.3}$$

Continuity Equation

$$\frac{\partial n_1}{\partial t} + \frac{\partial}{\partial z}\left[(n_0 + n_1)(v_0 + v_1)\right] = 0,$$
$$\frac{\partial n_1}{\partial t} + n_0 \frac{\partial v_1}{\partial z} + v_0 \frac{\partial n_1}{\partial z} = 0,$$
$$i\omega \tilde{n}_1 - ik n_0 \tilde{v}_1 - ik v_0 \tilde{n}_1 = 0,$$

$$\tilde{n}_1 = \frac{k n_0 \tilde{v}_1}{(\omega - k v_0)}. \tag{A.4}$$

Equation of Motion

$$q_e E_1 = m_e \left[\gamma_0 \frac{\partial v_1}{\partial t} + v_0 \frac{\partial \gamma_1}{\partial t} + v_0{}^2 \frac{\partial \gamma_1}{\partial z} + v_0 \gamma_0 \frac{\partial v_1}{\partial z} \right],$$
$$q_e \tilde{E}_1 = m_e i \left[\omega \gamma_0 \tilde{v}_1 + \omega v_0 \tilde{\gamma}_1 - k v_0{}^2 \tilde{\gamma}_1 - k v_0 \gamma_0 \tilde{v}_1 \right]$$ Rearranging gives

$$q_e \tilde{E}_1 = c_0 \gamma_0 m_e i \left[\omega - k v_0 \right] \left(\tilde{\beta}_1 + \beta_0 \frac{\tilde{\gamma}_1}{\gamma_0} \right).$$

Assuming $\frac{\beta_1}{\beta_0} << 1$, we simplify the above by **

$$q_e\widetilde{E}_1 = v_0\gamma_0 m_e i[\omega - kv_0]\left(\frac{\widetilde{\beta}_1}{\beta_0}+\frac{\widetilde{\gamma}_1}{\gamma_0}\right),$$

$$q_e\widetilde{E}_1 \approx v_0\gamma_0 m_e i[\omega - kv_0]\frac{\beta_1}{\beta_0}\gamma_0^{\,2},$$

$$q_e\widetilde{E}_1 = c_0\gamma_0^{\,3} m_e i[\omega - kv_0]\beta_1,$$

$$q_e E_1 = \gamma_0^{\,3} m_e i[\omega - kv_0]v_1. \tag{A.5}$$

$$**\gamma_0+\gamma_1 = \left[1-(\beta_0+\beta_1)^2\right]^{-1/2}$$

$$\gamma_0(1+\gamma_1/\gamma_0) = \left[1-\beta_0^{\,2}(1+\beta_1/\beta_0)^2\right]^{-1/2}$$

Let $f(x) = \left[1-\beta_0^{\,2}(1+x)^2\right]^{-1/2}$, then $f'(x) = \beta_0^{\,2}\left[1-\beta_0^{\,2}(1+x)^2\right]^{-3/2}(1+x)$

$$\gamma_0\left(1+\frac{\gamma_1}{\gamma_0}\right) = \left[1-\beta_0^{\,2}\right]^{-1/2} + \beta_0^{\,2}\left[1-\beta_0^{\,2}\right]^{-3/2}\left(\frac{\beta_1}{\beta_0}\right) + HOT$$

$$\gamma_0\left(1+\frac{\gamma_1}{\gamma_0}\right) = \gamma_0 + \beta_0^{\,2}\gamma_0^{\,3}\frac{\beta_1}{\beta_0} + HOT$$

$$\frac{\gamma_1}{\gamma_0} = \beta_0^{\,2}\gamma_0^{\,2}\frac{\beta_1}{\beta_0} + HOT$$

$$\frac{\beta_1}{\beta_0}+\frac{\gamma_1}{\gamma_0} = \frac{\beta_1}{\beta_0}\left(1+\beta_0^{\,2}\gamma_0^{\,2}\right) + HOT$$

$$= \frac{\beta_1}{\beta_0}\gamma_0^{\,2} + HOT.$$

Substitute n

Substitute n_1 (A.4) into E_1 (A.3) and using the new $\widetilde{E}_1$ in (A.5)

$$q_e\frac{iq_e}{k\varepsilon_0}\frac{kn_0\widetilde{v}_1}{(\omega-kv_0)} = \gamma_0^{\,3} m_e i(\omega-kv_0)\widetilde{v}_1,$$

$$(\omega-kv_0)^2 = \omega_p^2/\gamma_0^2.$$

Clearly

$$\omega = kv_0 \pm \omega_p/\gamma_0 \tag{A.6}$$

where $\omega = kv_0+\omega_p/\gamma_0$ is the dispersion for the fast space charge waves while $\omega = kv_0-\omega_p/\gamma_0$ is the dispersion for slow space charge waves [48]. The dispersion relations for both waves are plotted in Figure A.1.

Both waves have the same group velocity equal to the electron drift velocity v_0. Fast space charge waves are positive energy waves which give energy to electrons. A beam encountering fast waves will be accelerated by the waves. Slow space charge waves are negative energy waves which take energy from the electrons. Slow waves gain energy from moving electrons, causing electrons to slow down, thereby reducing their overall K.E.. Fast and slow waves are sustained through the exchange of energy between the beam and the two waves.

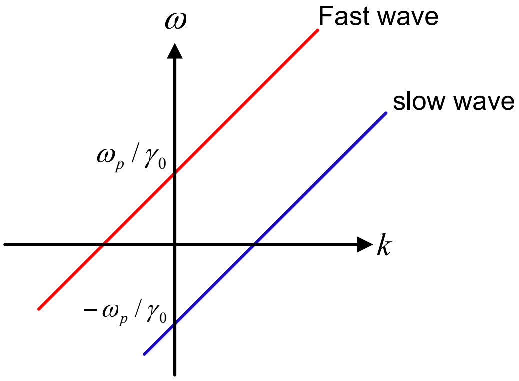

Figure A.1: Unbounded fast and slow space charge wave.

A.2 DISPERSION RELATION OF BOUNDED SPACE CHARGE WAVE IN RELATIVISTIC ELECTRON BEAM

The dispersion relation $\omega = kv_0 \pm \omega_p$ derived in the previous section describes unbounded free streaming electrons. For an electron beam propagating in a waveguide (Figure A.2), boundary conditions have to be accounted for and Poisson's equation must be replaced by Maxwell's equation.

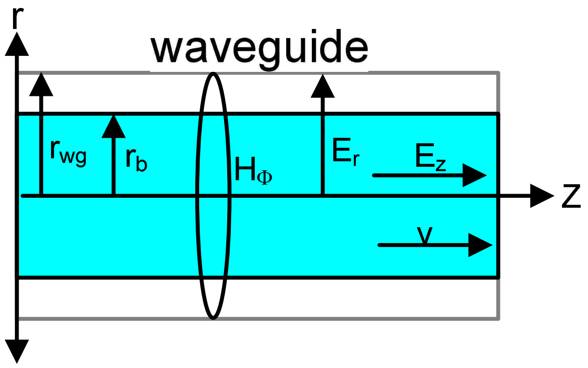

Figure A.2: Electron beam in a cylindrical waveguide

As we are now interested in the oscillating EM fields, we neglect the static fields in this derivation. All the electric and magnetic field components have only the perturbed states so the subscript 1 is dropped from the variables in Maxwell's equations. The electron beam has a current density given by

$$\tilde{J}_z = q_e n_0 \tilde{v}_1 + q_e v_0 \tilde{n}_1 . \tag{A.7}$$

Substituting $\tilde{n}_1 = \dfrac{k n_0 \tilde{v}_1}{(\omega - k_z v_0)}$ from (A.4) and $\tilde{v}_1 = \dfrac{q_e \tilde{E}_z}{\gamma_0{}^3 m_e i[\omega - k_z v_0]}$ from (A.5)

$$\tilde{J}_z = \left(q_e n_0 + q_e v_0 \frac{k n_0}{(\omega - k_z v_0)} \right) \frac{q_e \tilde{E}_z}{\gamma_0{}^3 m_e i[\omega - k_z v_0]},$$

$$= \frac{-i q_e{}^2 \tilde{E}_z \omega n_0}{\gamma_0{}^3 m_e (\omega - k_z v_0)^2}. \tag{A.8}$$

We neglect the TE modes which do not have an E_z field component. For the TM mode, we only have to account for the E_r, E_z and H_Φ components as the beam in the waveguide is axisymmetric.

Starting with Ampere's law with displacement current

$$\nabla x \vec{H} = \vec{J} + \varepsilon_0 \frac{\partial \vec{E}}{\partial t} . \tag{A.9}$$

We obtain the $\tilde{E}_r$ component from Ampere's law with displacement current

$$i k_z \tilde{H}_\phi = i \omega \varepsilon_0 \tilde{E}_r ,$$

$$\tilde{E}_r = \frac{k_z \tilde{H}_\phi}{\omega \varepsilon_0}. \tag{A.10}$$

We obtain the $\tilde{E}_z$ component from Ampere's law with displacement current

$$\frac{1}{r} \frac{\partial}{\partial r} (r \tilde{H}_\phi) = \tilde{J}_z + i \omega \varepsilon_0 \tilde{E}_z . \tag{A.11}$$

Starting with Faraday's Law

$$\nabla x \vec{E} = -\mu_0 \frac{\partial \vec{H}}{\partial t} , \tag{A.12}$$

we obtain the $\tilde{H}_\phi$ component as

$$-ik_z\tilde{E}_r - \frac{\partial \tilde{E}_z}{\partial r} = -i\omega\mu_0\tilde{H}_\phi. \tag{A.13}$$

Substitute $\tilde{E}_r = \dfrac{k_z\tilde{H}_\phi}{\omega\varepsilon_0}$ into (A.13) yields

$$ik_z\frac{k_z\tilde{H}_\phi}{\omega\varepsilon_0} + \frac{\partial \tilde{E}_z}{\partial r} = i\omega\mu_0\tilde{H}_\phi,$$

$$i\tilde{H}_\phi\left(k_z\frac{k_z}{\omega\varepsilon_0} - \omega\mu_0\right) = -\frac{\partial \tilde{E}_z}{\partial r},$$

$$\tilde{H}_\phi = \left(\frac{i\omega\varepsilon_0}{k_z{}^2 - \omega^2/c_0{}^2}\right)\frac{\partial \tilde{E}_z}{\partial r}. \tag{A.14}$$

Substituting $\tilde{H}_\phi$ (A.14) and $\tilde{J}_z$ (A.8) to (A.11) yields

$$\frac{1}{r}\frac{\partial}{\partial r}\left[r\left(\frac{i\omega\varepsilon_0}{k_z{}^2 - \omega^2/c_0{}^2}\right)\frac{\partial \tilde{E}_z}{\partial r}\right] = \tilde{J}_z + i\omega\varepsilon_0\tilde{E}_z,$$

$$\frac{1}{r}\frac{\partial}{\partial r}\left(r\frac{\partial \tilde{E}_z}{\partial r}\right) = \left(\frac{\tilde{J}_z}{i\omega\varepsilon_0} + \tilde{E}_z\right)k_\perp{}^2,$$

$$\frac{1}{r}\frac{\partial}{\partial r}\left(r\frac{\partial \tilde{E}_z}{\partial r}\right) + \left(\frac{q_e{}^2\tilde{E}_z n_0}{\varepsilon_0\gamma_0{}^3 m_e(\omega - k_z v_0)^2} - \tilde{E}_z\right)k_\perp{}^2 = 0,$$

$$\frac{1}{r}\frac{\partial}{\partial r}\left(r\frac{\partial \tilde{E}_z}{\partial r}\right) + k_\perp{}^2 m^2\tilde{E}_z = 0,$$

where $k_\perp{}^2(k_z,\omega) = k_z{}^2 - \omega^2/c_0{}^2$ and $m^2(k_z,\omega) = \dfrac{\omega_p{}^2}{\gamma_0^2(\omega - k_z v_0)^2} - 1.$

The above equation is a 2nd order Bessel Equation for E_z. In the region within the beam radius $r<r_b$

$$\tilde{E}_z = [AJ_0(rk_\perp m)]e^{-ik_z z}\ . \tag{A.15}$$

In the region between the beam radius and waveguide radius $r_b<r<r_{wg}$, $\omega_p=0$

$$\tilde{E}_z = [BI_0(rk_\perp) + CK_0(rk_\perp)]e^{-ik_z z}. \tag{A.16}$$

A, B, and C are constants to be determined by the following boundary conditions.

Boundary Conditions

First boundary condition: $\tilde{E}_z$ is zero at the surface of the waveguide thus

$$\tilde{E}_z(r_{wg}k_\perp) = 0$$

$$BI_0(r_{wg}k_\perp) + CK_0(r_{wg}k_\perp) = 0,$$

$$C = -B\frac{I_0(r_{wg}k_\perp)}{K_0(r_{wg}k_\perp)}. \tag{A.17}$$

Second boundary condition: continuity of $\tilde{E}_z$ field at r=r$_b$

$$\left.\tilde{E}_z\right|_{rb-} = \left.\tilde{E}_z\right|_{rb+}$$

$$AJ_0(r_b k_\perp m) = BI_0(r_b k_\perp) + CK_0(r_b k_\perp),$$

$$AJ_0(r_b k_\perp m) = B\left(I_0(r_b k_\perp) - \frac{I_0(r_{wg}k_\perp)}{K_0(r_{wg}k_\perp)}K_0(r_b k_\perp)\right). \tag{A.18}$$

Third boundary condition: continuity of H$_\Phi$ field at r=r$_b$

$$\left.\tilde{H}_\phi\right|_{rb-} = \left.\tilde{H}_\phi\right|_{rb+}$$

$$\left(\frac{i\omega\varepsilon_0}{k_z{}^2 - \omega^2/c_0{}^2}\right)\left.\frac{\partial\tilde{E}_z}{\partial r}\right|_{rb-} = \left(\frac{i\omega\varepsilon_0}{k_z{}^2 - \omega^2/c_0{}^2}\right)\left.\frac{\partial\tilde{E}_z}{\partial r}\right|_{rb+}$$

$$-AmJ_1(r_b k_\perp m) = BI_1(r_b k_\perp) - CK_1(r_b k_\perp)$$

$$-AmJ_1(r_b k_\perp m) = B\left(I_1(r_b k_\perp) + \frac{I_0(r_{wg}k_\perp)}{K_0(r_{wg}k_\perp)}Y_1(r_b k_\perp)\right). \tag{A.19}$$

Using the three boundary conditions we obtain the dispersion relation for the beam

$$\frac{I_1(r_b k_\perp)K_0(r_{wg}k_\perp) + I_0(r_{wg}k_\perp)K_1(r_b k_\perp)}{I_0(r_b k_\perp)K_0(r_{wg}k_\perp) - I_0(r_{wg}k_\perp)K_0(r_b k_\perp)} = \frac{-mJ_1(r_b k_\perp m)}{J_0(r_b k_\perp m)}. \tag{A.20}$$

The above dispersion relation is solved numerically using the root finding function in Mathcad v14.

Breizman and Ryutov [26] obtained a quadratic form of the dispersion relation in Appendix I of their paper. In their derivation they assumed a thin electron beam and applied the Leontovich boundary condition instead of the continuity of H$_\Phi$. Using the continuity of E$_Z$ field and H$_\Phi$ field on the beam radii as the other two boundary conditions, they solved for the lowest mode. By setting conductivity σ→∞, they obtain a closed form solution for the dispersion relation given by

$$\left(\mathrm{k}_z - \frac{\omega}{\mathrm{v}_0}\right)^2 = \left(\mathrm{k}_z{}^2 - \frac{\omega^2}{\mathrm{c}_0{}^2}\right)\xi \ln\frac{\mathrm{r}_{wg}}{\mathrm{r}_b}, \tag{A.21}$$

where $\xi = 2qI_b / mv_0{}^3\gamma_0{}^3$ and I_b is the unperturbed beam current.

The above equation is solved using Mathcad v14 by finding the roots of the quadratic equation. We solve for a 50 keV, 500 A beam with beam radius 1.0 inch and waveguide radius of 1.6 inch. Figure A.3 shows a plot of the dispersion relation for our space charge waves dispersion (A.20) compared with that derived by Breizman and Ryutov, and Lawson.

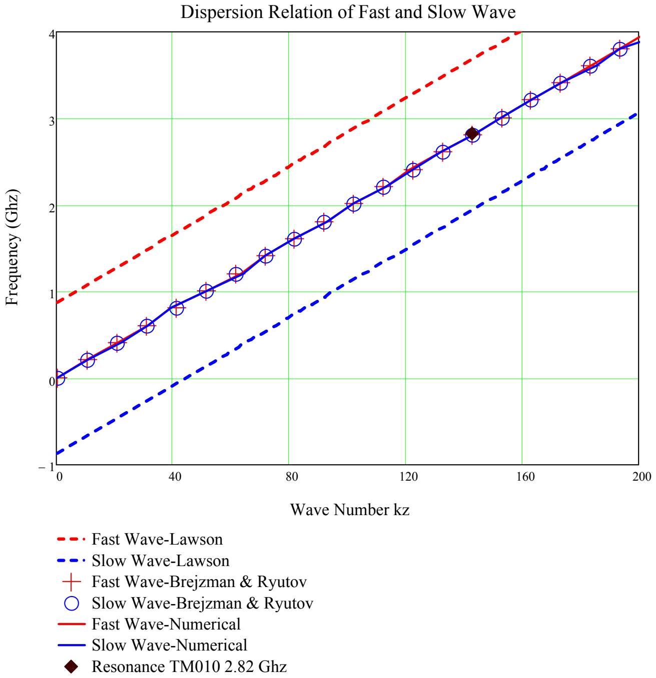

Figure A.3: Dispersion relation for fast and slow space charge waves.

Any wave inside the reltron cavity can only resonate at certain frequencies depending on the eigenmode of the wave. As such, the cavity dispersion relation is not continuous but varies as discrete points in the frequency. This implies that the space charge wave will resonate at discrete frequencies inside the cavity. The cavity is cylindrical with radius 1.6 inch and height 0.75 inch. The lowest resonant frequency for the TM_{010} mode in the cavity is calculated to be 2.82 GHz. The space charge wave inside the waveguide will thus oscillate at 2.82 GHz and, in turn, cause the electrons to oscillate at the same frequency and have a wave number of 142 rad/m.